UNIVERSITEIT VAN PRETORIA
UNIVERSITY OF PRETORIA
YUNIBESITHI YA PRETORIA

CHARACTERISATION OF THE IONOSPHERE OVER THE SOUTH ATLANTIC ANOMALY BY USING A SHIP-BASED DUAL-FREQUENCY GPS RECEIVER

by

Stefanus Jansen van der Merwe

Submitted in partial fulfillment of the requirements for the degree

Master of Engineering (Electronic)

in the

Faculty of Engineering, Built Environment and Information Technology
Department of Electrical, Electronic and Computer Engineering

UNIVERSITY OF PRETORIA

February 2011

UNIVERSITEIT VAN PRETORIA
UNIVERSITY OF PRETORIA
YUNIBESITHI YA PRETORIA

DECLARATION OF AUTHORSHIP

I, S.J. van der Merwe, declare that this dissertation titled, 'Characterisation of the ionosphere over the South Atlantic Anomaly by using a ship-based dual-frequency GPS receiver' and the work presented in it are my own. I confirm that:

- This work was done wholly or mainly while in candidature for a research degree at the University of Pretoria.
- Where any part of this dissertation has previously been submitted for a degree or any other qualification at this University or any other institution, this is clearly stated.
- Where I have consulted the published work of others, this is always clearly attributed.
- Where I have quoted from the work of others, the source is always given. With the exception of such quotations, this dissertation is entirely my own work.
- I have acknowledged all main sources of help.
- Where the thesis is based on work done by me in collaboration with others, I clearly state exactly what was done by others and what my contribution was.

Signed: _____

Date: _____

"Only when you drink from the river of silence shall you indeed sing.
And when you have reached the mountain top, then you shall begin to climb.
And when the earth shall claim your limbs, then shall you truly dance."

Kahlil Gibran

UNIVERSITEIT VAN PRETORIA
UNIVERSITY OF PRETORIA
YUNIBESITHI YA PRETORIA

SUMMARY

CHARACTERISATION OF THE IONOSPHERE OVER THE SOUTH ATLANTIC ANOMALY BY USING A SHIP-BASED DUAL-FREQUENCY GPS RECEIVER

by

Stefanus Jansen van der Merwe

Supervisors: Dr. Pierre Cilliers (Hermanus Magnetic Observatory, South Africa)
Dr. Pieter de Villiers (University of Pretoria, South Africa)
Department: Department of Electrical, Electronic and Computer Engineering
University: University of Pretoria
Degree: Master of Engineering (Electronic)

Keywords: Ionosphere, tomography, total electron content, high frequency communications, South Atlantic Anomaly, mobile dual-frequency GPS, electron density.

The ionosphere is a layer of ionised gas in the upper layers of the atmosphere around the Earth that plays a critical role in satellite communication, military communication and space science. The influence that the ionosphere has on communication systems can be quantified if the distribution of the electron density within the ionosphere is known. Several methods and instruments to determine the distribution of electron density are currently being used: satellites, ionosondes, incoherent scatter radars and computerised ionospheric tomography based on dual-frequency GPS signals. The present study investigates a novel way of using GPS receivers on mobile platforms to achieve near real-time ionospheric characterisation over locations beyond the reach of land-based ionospheric characterisation methods. GPS observations were collected, preprocessed and inverted by means of tomography to generate three-dimensional electron density maps. These electron density maps were analysed and verified. The viability of using observations from a mobile GPS receiver for ionospheric tomography was investigated.

The algorithms were verified by means of a model ionosphere and a simulated GPS

receiver. Furthermore, electron density maps generated from GPS observables from a mobile receiver were verified against ionosonde-derived electron density profiles, static land-based GPS receivers and known high-frequency propagation paths using propagation path prediction. The results were evaluated and the conclusion was that, although some aspects still have to be addressed, a dual-frequency GPS receiver on a ship can provide useful ionospheric characterisation in areas which are otherwise poorly or not covered by land-based receivers.

UNIVERSITEIT VAN PRETORIA
UNIVERSITY OF PRETORIA
YUNIBESITHI YA PRETORIA

OPSOMMING

KARAKTERISERING VAN DIE IONOSFEER OOR DIE SUID-ATLANTIESE ANOMALIE DEUR GEBRUIK TE MAAK VAN 'N MOBIELE DUBBELFREKWENSIE GPS-ONTVANGER OP 'N SKIP

deur

Stefanus Jansen van der Merwe

Studieleiers: Dr. Pierre Cilliers (Hermanus Magnetiese Observatorium, Suid Afrika)
Dr. Pieter de Villiers (Universiteit van Pretoria, Suid Afrika)
Departement: Departement van Elektriese, Elektroniese en Rekenaaringenieurswese
Universiteit: Universiteit van Pretoria
Graad: Meester van Ingenieurswese (Elektronies)

Sleutelwoorde: Ionosfeer, tomografie, totale elektron inhoud, hoë frekwensie kommunikasie, Suid-Atlantiese Anomalie, mobiele dubbelfrekwensie GPS, elektrondigtheid.

Die ionosfeer is 'n laag geïoniseerde gas wat voorkom rondom die Aarde in die boonste laag van die atmosfeer en speel 'n kritieke rol speel in satellietkommunikasie, militêre toepassings en ruimtefisika. Die aard en vlak van invloed wat die ionosfeer op kommunikasiestelsels het, kan bepaal word indien die elektrondigtheidsverspreiding van die ionosfeer bekend is. Verskeie metodes en instrumente om elektrondigtheid te bepaal word tans gebruik: satelliete, ionosondes, inkoherente verstrooiings radar en ionosferiese tomografie wat van dubbelfrekwensie GPS-ontvangers gebruik maak. Die huidige studie ondersoek die gebruik van mobiele GPS ontvangers om 'n naby-intydse karakterisering van die ionosfeer te lewer. GPS-observasies is versamel, voorafverwerk en elektrondigtheidsprofiele is deur middel van tomografiese omkering genereer. Die elektrondigtheidsprofiele is ontleed en geverifieer. Die bruikbaarheid van 'n mobiele dubbelfrekwensie GPS-ontvanger vir ionosferiese tomografie is ondersoek.

Die algoritmes is geverifieer deur middel van 'n model-ionosfeer en 'n gesimuleerde GPS-ontvanger. Elektrondigtheidsprofiele wat verkry is vanaf observasies van 'n mobiele GPS-ontvanger, is geverifieer teen ionosonde-gebaseerde profiele, teen statiese

landgebaseerde GPS-ontvangers en teen bekende hoëfrekwensie seinpaaie deur van algoritmes vir propagasiepadvoorspelling gebruik te maak. Die resultate is geëvalueer en die gevolgtrekking is dat, alhoewel sekere aspekte van die tomografie proses nog ondersoek benodig, dubbelfrekwensie GPS-ontvangers bruikbare elektrondigtheidprofiele kan lewer vir gebiede wat buite die bereik val van landgebaseerde metodes.

ACKNOWLEDGEMENTS

The author would like to extend his appreciation to the following people and institutions:

- Dr. Pierre Cilliers, for all his support and the amazing unforgettable opportunities he gave me. I have come to know him not only as a supervisor, but as an inspired, extremely energetic, wonderful person who gives glory to God in everything he does.
- Dr. Pieter de Villiers, for all his support, guidance and inspiration throughout the past three years. I have come to know him not only as a supervisor, but as a friend and colleague.
- Telkom Centre of Excellence (CoE) for granting me a bursary. Without their financial support this research would not have been possible.
- Centre for Teletraffic Engineering in an Information Society (CeTEIS) for their financial assistance for conference attendance.
- Everyone who supported me throughout my postgraduate studies, and especially during the writing of this dissertation.

LIST OF ABBREVIATIONS

BPSK	**B**inary **P**hase **S**hift **K**eying
CIT	**C**omputerised **I**onospheric **T**omography
ELF	**E**xtremely **L**ow **F**requency
EOF	**E**mpirical **O**rthogonal **F**unction
GPS	**G**lobal **P**ositioning **S**ystem
HF	**H**igh **F**requency
HMO	**H**ermanus **M**agnetic **O**bservatory
IOC	**I**ntergovernmental **O**ceanographic **C**ommission of UNESCO
IODE	**I**nternational **O**ceanographic **D**ata and Information **E**xchange
IRI	**I**nternational **R**eference **I**onosphere
LTEC	**L**-observable **T**otal **E**lectron **C**ontent
MIDAS	**M**ulti-**I**nstrument **D**ata **A**nalysis **S**ystem
ODINAFRICA	**O**cean **D**ata and **I**nformation **N**etwork for **Africa**
PRN	**P**seudo **R**andom **N**umber
PTEC	**P**-observable **T**otal **E**lectron **C**ontent
RMS	**R**oot **M**ean **S**quare
SAA	**S**outh **A**tlantic **A**nomaly
STEC	**S**lant **T**otal **E**lectron **C**ontent
TEC	**T**otal **E**lectron **C**ontent
VTEC	**V**ertical **T**otal **E**lectron **C**ontent
VLF	**V**ery **L**ow **F**requency

TERMINOLOGY

AGHL GPS receiver	The GPS receiver on the SA Agulhas vessel
CTWN GPS receiver	The GPS receiver in Cape Town, South Africa
Electron density map	3-D voxel map representation of electron density
Electron density distribution	2-D longitudinal or latitudinal slice from the 3-D voxel map shown with altitude (height) along the y-axis
Electron density profile	1-D electron density curve of a specific longitude and latitude with altitude (height) on the y-axis
Epoch	GPS instance of time associated with a single observation of slant TEC from transmitter to receiver
GOGH GPS receiver	The GPS receiver on Gough Island
GPS observables	GPS variables needed to perform ionospheric tomography - $L1$, $L2$, $P1$ and $P2$
High latitude	Latitudes close to the poles
Low latitude	Latitudes close to the equator
Voxel	One element of an electron density map characterised by a unique latitude, longitude and altitude
Total electron content map	Map of the vertical total electron content as seen from above the ionosphere
Valid satellite	A satellite with a complete set of GPS observables needed to perform ionospheric tomography

SYMBOLS AND UNITS

$TECU$	Total Electron Content Units	$10 \times^{16} \frac{electrons}{m^2}$
N	electron density	$10 \times^{12} \frac{electrons}{m^3}$
ω	angular frequency	$\frac{rad}{s}$
f	frequency	Hz
e	mathematical constant	≈ 2.71828
e	abbreviation for electrons	

TABLE OF CONTENTS

This dissertation is firstly dedicated to my Heavenly Father, who by His grace gave me all the tools necessary to write it. Secondly, I dedicate this to my grandfather, Toon van der Merwe, who has joined my Heavenly Father. Without Oupa's inspiration, playful spirit and imagination I would not be where I am today. I hope to see Oupa again soon!

CHAPTER 1

INTRODUCTION

The ionosphere is a layer of ionised gas in the upper layer of the atmosphere around the Earth that plays a critical role in satellite communications, military communications and space physics. Satellite signals penetrating the ionosphere are delayed and refracted to such a degree that this effect cannot simply be ignored. The delay and refraction of transionospheric signals are proportional to the amount of ionised gas or equivalently, the number of free electrons or total electron content (TEC), in the ionosphere along a ray path from the satellite to the receiver. The unit of TEC is the number of electrons in a column with a perpendicular surface of one square meter. Total electron content is measured in TEC units (TECU) - one TECU is equal to 1×10^{16} $\frac{\text{electrons}}{\text{m}^2}$. The delay and refraction are to first order inversely proportional to the square of the frequency of the signal. The Global Positioning System (GPS), launched by the US Department of Defence in the 1970's, originally used an array of 24 satellites orbiting at an altitude of 20 200 km to transmit signals to receivers on the surface of the Earth. The receivers are able to determine their location through triangulation, using the distances to each of the visible GPS satellites as derived from the duration of travel of the signal from GPS satellite to receiver. In order to compensate for the delay introduced in the GPS signal by the ionosphere, the GPS signals are transmitted at two phase-coherent frequencies. Since the delay and refraction are inversely proportional to frequency, the difference in the duration of travel of the signal at the two frequencies can be used to determine the total electron content along the ray path in the ionosphere. If a sufficient number of observations of TEC along different ray paths can be made at a single location, the spatial distribution of the electrons in the ionosphere can be obtained through an inversion process similar to X-ray tomography. This is known as Computerised Ionospheric

Tomography (CIT). The result is a three-dimensional (3D) electron density map of the ionosphere.

The advantages of using GPS signals for ionospheric characterisation over other ionospheric characterisation methods such as ionosondes and incoherent scatter radars are that GPS is globally available and much less expensive to the user. The ionosondes can only give an accurate presentation of the ionosphere directly above the device and within a limited radius. GPS signals are also available twenty-four hours a day, seven days a week and have a high temporal resolution and instantaneous global coverage. GPS observations can easily be taken on ships and other mobile vehicles, enabling scientists to investigate ionospheric effects in locations far from land, where the shielding effect of the Earth's magnetic field against high energy particles from the solar wind is reduced, such as over the South Atlantic Anomaly (SAA).

The South Atlantic Anomaly is a region located in the southern hemisphere over the Atlantic Ocean where the Earth's magnetic field is at its weakest and decreasing at an unprecedented rate. This is where the Van Allen radiation belts are the closest to the Earth's surface. This region is also prone to increased ionospheric ionisation by high energy particles originating from the Van Allen radiation belts. The reduced shielding in the SAA has a major influence on communication and electronic systems passing through this area. The abnormal behaviour of the ionosphere makes inter-continental high frequency (HF) propagation difficult to predict over this region. The advent of CIT via GPS makes the characterisation of the ionosphere possible. The result of this characterisation will advance technology in communication, military and navigational applications.

In this dissertation the application of CIT to the ionosphere over the South Atlantic Anomaly by use of a mobile dual-frequency GPS receiver on the South African polar research vessel, the SA Agulhas, is investigated. Data was gathered on the SA Agulhas voyage to Antarctica in 2009, and on several subsequent trips to Marion Island and Gough Island. Software was developed for the preprocessing of the GPS data. Tomography was performed on the data (using the MIDAS software package developed at the University of Bath) and the resulting electron density maps were analysed and verified. The viability of using a mobile GPS receiver for ionospheric tomography is investigated and results are presented.

1.1 MOTIVATION

The ionosphere has always been a subject of great interest in radio communication, and for all practical purposes, its study has always been challenging. In situ measurement of the electron density of the ionosphere is done with rockets and low Earth orbit satellites, but such observations are intermittent and very expensive. As a result, multiple methods exist to measure the electron density of the ionosphere indirectly from Earth. These methods include ionosondes and high-powered incoherent scatter radars - all of which have certain limitations. A satellite operating specifically to monitor the ionosphere from above is expensive and there are only a few such satellites (the CHAMP and COSMIC satellites). The satellites also have a very limited resolution - for one satellite to orbit the Earth takes a while and since the ionosphere is a dynamic ever-changing medium, this limits the time resolution of the measurements. Ionosondes are devices which sound the ionosphere from the surface of the Earth. Ionosondes are limited to characterising the ionosphere directly above the antenna. Large antennas are needed to operate the ionosondes, limiting their mobility. Incoherent scatter radars are extremely expensive to operate, because of their high power requirements, and because they require a large parabolic dish antenna.

Dual-frequency GPS receivers allow for inexpensive, mobile, high-resolution charateri-sation of the ionosphere. However, thus far, these GPS devices have only been sed as static base stations, mostly as an adjunct to single-frequency surveying receivers and for geodetic observations. The use of mobile dual-frequency receivers for this purpose on ships has not been implemented until now.

Given the large number of ships travelling the Earth's oceans every day, if each of these ships could be equipped with a mobile dual-frequency GPS receiver, very high-resolution, near real-time electron density maps of the ionosphere could be provided to several technologies which require an estimate of the current state of the ionosphere. The need for analysis of and investigation into the viability of such a large research venture is clear. This is what the research presented in this dissertation hopes to achieve by investigating the viability of the charactisation of the ionosphere, using data from a dual-frequency GPS receiver on the SA Agulhas, the first ship thus far known to be equipped with such an instrument.

Possible applications of results obtained from such an investigation include, but are not limited to:

- HF propagation path prediction
- Near real-time GPS corrections for application in:
  - Autopilot in aircraft
  - Accurate military guidance systems
  - Military HF direction-finding
- Characterising the South Atlantic Anomaly

Clearly, an improved characterisation of the ionosphere would be of great value to space scientists, the military, physicists who use the ionosphere for space weather research and for frequency prediction for high frequency radio communication. A more accurate electron density map of the ionosphere over the SAA region would enable scientists to improve their understanding of the SAA and its effects on the Earth-space environment.

1.2 OBJECTIVES

The primary objective of this dissertation was to investigate the viability of using a mobile GPS receiver for ionospheric tomography. This was achieved by the verification of the electron density maps obtained by using observables from the mobile GPS receiver. Secondary objectives were to develop a system for processing data from a mobile dual-frequency GPS receiver and using this data to obtain electron density maps by means of a known inversion algorithm.

1.2.1 Data and algorithm verification

The results obtained from MIDAS were verified using the following methods.

1. Inversion electron density maps were compared with known values for a simulated mobile GPS receiver in a modelled ionosphere for different parameters.

2. A comparison was made between the electron density height profiles generated via inversion using observables from a mobile GPS receiver and the profiles from an ionosonde currently in operation at the Hermanus Magnetic Observatory (HMO), South Africa.

3. A comparison was made between electron density maps generated from observables from the GPS receiver on board the SA Agulhas and those generated from observables from static land-based GPS receivers for a period when the ship was near such land-based receivers.

4. A comparison was made between predicted HF propagation paths and propagation results from the HF Beacon experiment. The predictions were based on electron density maps generated from GPS observables from the SA Agulhas GPS receiver as well as electron density maps generated using the IRI2007 model.

1.2.2 System development and data preprocessing

The software for the system developed was implemented in MATLAB and performs the following functions:

1. Accepts raw data measured by the Ashtech Z-12 dual-frequency GPS receiver and logged by the GBSS software on board the SA Agulhas.

2. Converts data to standard RINEX format and isolates useful data.

3. Preprocesses the useful data as input for the MIDAS software package.

1.2.3 Data processing

The MIDAS software package was modified to allow for the use of data from a terrestrial mobile receiver as opposed to data from static receivers for which the algorithm was originally developed. The modified MIDAS software was used to calculate electron density maps and TEC distributions over the region of observation.

1.3 CONTRIBUTIONS

The following research outputs were produced during the course of this investigation:

- "Characterization of the Ionosphere over the South Atlantic Anomaly by using a ship based Dual Frequency GPS receiver" in the proceedings of the 55th Annual Conference of the South African Institute of Physics (SAIP), CSIR International Convention Centre, Pretoria, South Africa, 27 Sept. - 1 Oct., 2010.
- "Characterization of the Ionosphere over the South Atlantic Anomaly by using a ship based Dual Frequency GPS receiver as aid for HF propagation path prediction" in the Proceedings of South African Telecommunication, Networks and Applications Conference (SATNAC 2010), Stellenbosch, South Africa, 5-8 Sept., 2010.

1.4 STRUCTURE OF THIS DISSERTATION

This dissertation has been structured as follows: *Chapter 2* presents a brief overview of the theoretical aspects of space physics and of the algorithms which form the basis for this research - the ionosphere, the South Atlantic Anomaly (SAA) and GPS ionospheric tomography. In *Chapter 3* several characteristics of a mobile GPS receiver is simulated using a simulated mobile receiver and GPS observables from an IRI2007 generated ionosphere. In *Chapter 4* a number of experimental verification analyses are performed with GPS observables from the mobile dual-frequency GPS receiver installed on the SA Agulhas research vessel using ionosondes, static land-based GPS receivers and HF propagation path prediction. Chapter *Chapter 5* offers conclusions.

CHAPTER 2

BACKGROUND

2.1 THE IONOSPHERE

2.1.1 Properties of the ionosphere

The ionosphere is a partially ionised layer in the upper atmosphere ranging from 50 km to approximately 2000 km in altitude [1]. The main contributor to ionisation in the ionosphere is electromagnetic radiation in the form of extreme ultraviolet and X-rays from the sun, although other sources such as cosmic rays and energy transfer from charged particles of solar origin also play a role in this process. Ionisation loss processes such as molecular recombination of electrons and positive ions and the connection of electrons to neutral atoms counter-act ionisation [2].

The ionosphere has four defined layers: the D, E, F1 and F2 layers. These layers are shown in Fig. 2.1. These layers differ primarily in electron density and have different effects on signals penetrating the ionosphere [2]. In general, as the frequency of a signal increases, it penetrates deeper into the ionosphere. The D layer (50 km - 90 km) acts as the main contributor to signal loss because of its high neutral atomic and molecular density, causing a high electron collision frequency (2×10^6 per second at 75 km). The D layer also acts as a reflector in the Extremely Low Frequency (ELF - 3 Hz to 3 kHz) and Very Low Frequency (VLF - 3 kHz to 30 kHz) ranges. The E layer (90 km - 130 km) is an important layer for HF propagation in distances less than 2000 km. The F layer is divided into two layers, the F1 and F2 layers. However,

the differences between these two layers are only apparent during daytime - at night the F1 layer disappears. The F1 layer (130 km - 210 km) is usually penetrated by the same frequencies that penetrated the E-layer. These waves travel to the F2 layer (250 km - 400 km), which is the primary layer of interest in long-distance HF communication, because it is the layer with the highest electron density. The F layer is also the main contributor to GPS errors. The ionisation properties of the F layer are not significantly influenced by the solar zenith angle (angle of the sun in terms of the perpendicular reference to the Earth's surface) and can store received solar energy for many hours beyond sunset because of its low molecular collision rate [1].

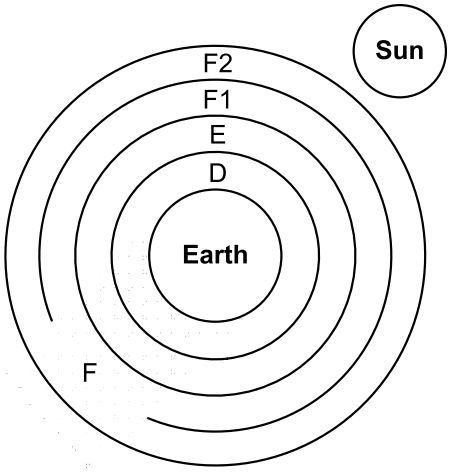

FIGURE 2.1: The ionosphere divided into layers.

2.1.2 Total electron content

Total electron content is the primary manner of defining the number of electrons in the ionosphere and is defined as the integrated value of electron concentration along a path of unit cross-section through the ionosphere. Total electron content is measured in TEC units (TECU) - one TECU is equal to 1×10^{16} $\frac{\text{electrons}}{\text{m}^2}$. For a satellite with a transmitter in orbit above the ionosphere and a receiver on the Earth's surface, the TEC is given by the following line integral [3]:

$$I = \int_r^s N(R, \Theta, \Lambda).dl \quad \text{in} \quad \frac{\text{electrons}}{\text{m}^2} \ , \tag{2.1}$$

where N is the electron density in electrons per cubic meter ($/\text{m}^3$), R is the radial distance from the centre of the earth (although N is only defined for heights above

the mean sea level of the earth), Θ is the geographical latitude, Λ is the geographical longitude and l is the path from the receiver r to the satellite s. The TEC does not provide any information about the distribution of the electrons along the ray path - it only gives total electron content along the line integral of (2.1). The TEC is a function of time, since the electron density N is also a function of time, with characteristic diurnal, seasonal and storm-enhanced time variations.

2.1.3 The South Atlantic Anomaly

The South Atlantic Anomaly, also known as the South Atlantic Magnetic Anomaly (SAMA), is a region in the southern hemisphere which is located over the Southern Atlantic Ocean and the western part of the Indian Ocean. The Earth's Van Allen radiation belts come closest to the Earth's surface over the SAA because the Earth's magnetic field is at its weakest in this region. Fig. 2.2 shows the location of the SAA in terms of the flux density of high energy protons from the Van Allen radiation belts over in this region.

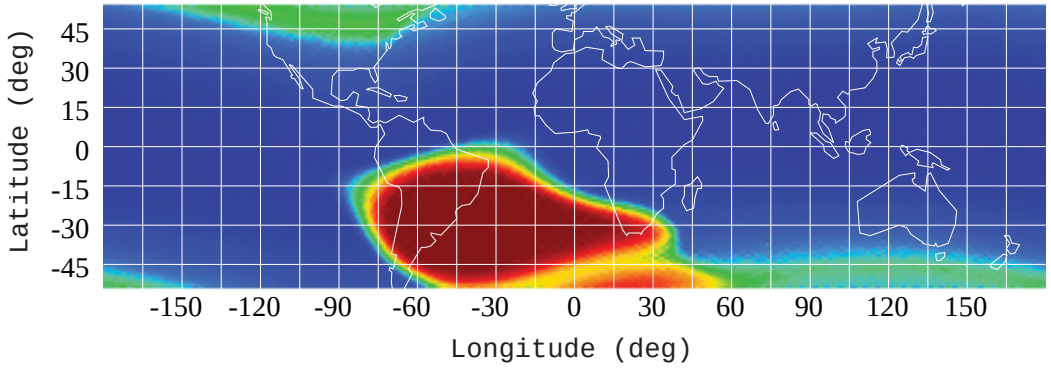

FIGURE 2.2: The South Atlantic Anomaly - contours show increased flux of high energy particles into the atmosphere as a result of the weaker magnetic field over this region. Taken from the NASA US ROSAT Science Data Center, with permission.

Thus an increased flux of high energy particles originating from the Sun is precipitated in this area and as a result, low Earth orbit satellites are exposed to higher levels of radiation and the impact of a higher frequency of high energy particles from the Van Allen radiation belts. Fig. 2.3 shows the contours of the total magnetic field intensity as well as the location of spacecraft anomalies that have occurred in the SAA.

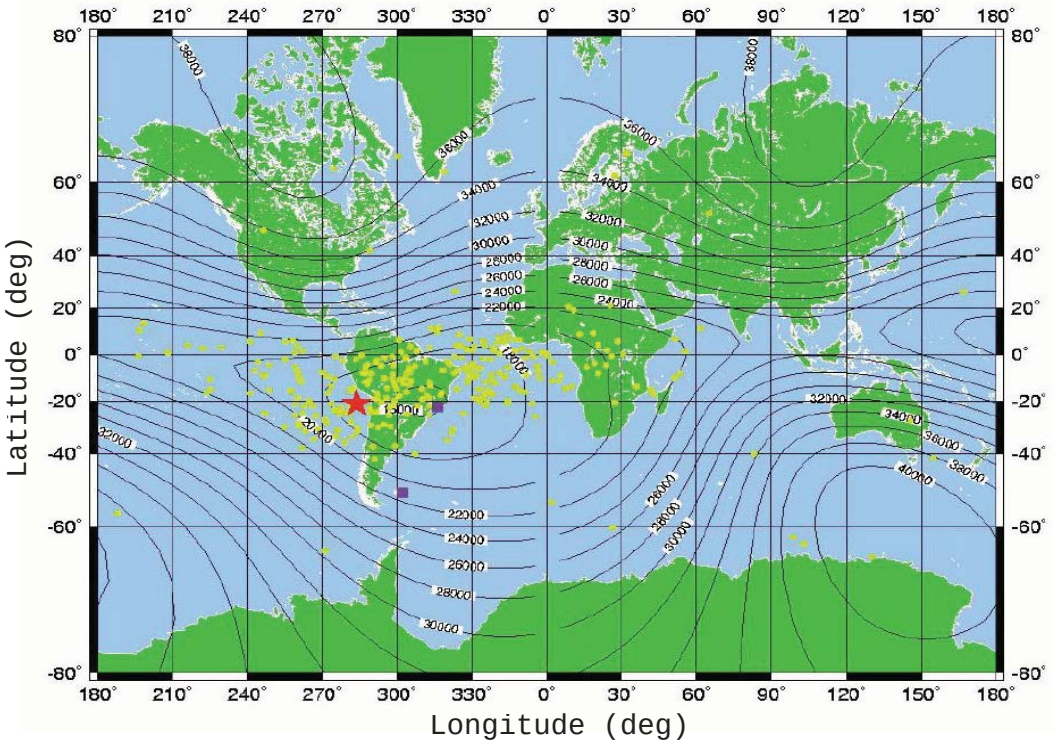

FIGURE 2.3: Contours of constant magnetic field intensity in nanotesla at 1 338 km altitude. Sites of spacecraft anomalies in the area of the SAA on TOPEX satellite (dots) and MODIS satellite (star) are indicated. Taken from [4], with permission.

The strength of the Earth's magnetic field is decreasing at a higher rate in this area than any other place on the surface of the Earth and a recent report suggested that a reverse dynamo is developing in the Earth's core below this area which may lead to a magnetic pole reversal [5]. All these factors cause increased and unusual ionisation levels and patterns in this region of the ionosphere, making it an interesting area for ionospheric scientists to characterise. Characterising this area may lead to a better understanding of the Earth-space environment. Better models of the ionosphere over this region may hold several potential advantages for military and commercial communication applications.

2.2 COMPUTERISED IONOSPHERIC TOMOGRAPHY (CIT)

X-ray tomography is the process used in medicine to reconstruct a three-dimensional view of the tissue density distribution in a patient's body by scanning the body with

X-rays and recording the total absorption along the ray paths through the body. This process can also be applied to the ionosphere in radio signal tomography, if the delays on signals penetrating the ionosphere along various ray paths can be recorded and then inverted to obtain the electron density maps. To accomplish this, ionospheric delays of signals from the GPS system are used.

2.2.1 The Global Positioning System (GPS)

The transmitter component of the GPS system was originally a constellation of 24 satellites (currently there are 31 operational satellites) in six orbit paths around the Earth at an altitude of approximately 20 200 km with an inclination of 55° to the equatorial plane [6]. The satellites continuously transmit two phase-coherent signals in the L band at 1575.42 MHz and 1227.60 MHz, known as L1 and L2 frequencies respectively and each satellite is identified by its unique pseudo-random number (PRN) code. Dual-frequency receivers are used to receive both these frequencies on the same antenna. The ionospheric TEC can be determined from the difference in the delays of the L1 and L2 signals due to the dispersion of the radio signals in the ionosphere.

The timing on the GPS signals are derived from a 10.23 MHz oscillator on the satellite with a stability of one in 10^{13} [6]. The messages used for navigation are modulated onto L1 and L2 at a rate of 50 Hz using binary phase shift keying (BPSK), and are then spread, using pseudo-random sequences, and transmitted towards the Earth. The largest contributor to GPS errors on the user side is due to ionospheric delays, caused predominantly by the layer with the highest electron density, i.e. the F layer. This delay can be estimated by dual-frequency receivers since they simultaneously detect the L1 and L2 signals. Thus, for TEC determination, dual-frequency GPS receivers are required as opposed to the single frequency receivers in common use for navigation. However, TEC is of great value for correcting the position error for single frequency GPS users. A system currently used in the USA, the Wide Area Augmentation System (WAAS), calculates the approximate delay using the TEC - since TEC is proportional to delay - and transmits this information to single frequency GPS users and aircraft navigation systems [7]. Therefore, a more accurate representation of the spatial electron density distribution of the ionosphere can be used to increase accuracy in commercial single frequency GPS receivers.

2.2.2 Ionospheric tomography

Ionospheric effects are the main contributor to the errors in GPS position determination. Computerised ionospheric tomography offers a readily available method to characterise the ionosphere in near real-time, thus enabling compensation for these errors in single frequency GPS receivers and other autonomous processes relying on GPS accuracy, such as automatic aircraft landing [8].

Before the advent of CIT, the primary method used for ionospheric prediction was by means of models derived using various observations by ionosondes, rockets and incoherent scatter radars over a number of years. One of the best known theoretical models is the Chapman layer model [9] in which the ionosphere is characterised by using the balance between ionisation and recombination of the gasses in the upper atmosphere. The Chapman model will be discussed in more detail in Section 2.2.4.1. Another widely used empirical model is the International Reference Ionosphere (IRI) which is the standard model of the ionosphere adopted by the International Telegraphic Union (ITU). The IRI model provides the monthly averages of several ionospheric parameters and is updated regularly through international collaboration of scientists. When space weather is quiet, the models give an adequate representation of the ionosphere at mid-latitudes. However, at high latitudes the ionosphere is highly variable and the models lack accuracy. The most widely known technique for localizing the point at which the ray path from the GPS satellites traverses the ionosphere is the "thin shell" method, where the ionosphere is modelled as a thin layer at a fixed height. By means of the "thin shell" model, the TEC measurements are mapped onto a two-dimensional (2-D) surface to obtain a distribution of vertical TEC. Several new methods have been developed to allow the derivation of three-dimensional (3-D) - latitude, longitude and height - and four-dimensional (4-D) - latitude, longitude, height and time - distributions of electron density, such as the Multi-Instrument Data Analysis System (MIDAS) [10] and the Electron Density Assimilative Model (EDAM) [11]. These methods incorporate GPS data and different basis functions of the electron density distribution to generate electron density maps from TEC observations.

Ionospheric tomography and the GPS data processing will now be discussed.

2.2.2.1 From GPS observations to total electron content

A signal propagates at the speed of light, c, in a vacuum. In a dispersive medium the velocity of the signal is modified by the refractive index, defined as

$$n = \frac{c}{v} \ , \tag{2.2}$$

where v is the velocity of the wave while it passes through the refractive medium. The refractive index of the ionosphere is defined by the Apple-Hartree equation [12]:

$$n^2 = 1 - \frac{X}{1 - jZ - [\frac{Y_T^2}{2(2-X-jZ)}] \pm [\frac{Y_T^4}{4(1-X-jZ)^2} + Y_L^4]^{\frac{1}{2}}} \ , \tag{2.3}$$

where the variables are defined as

$$X = \frac{\omega_p^2}{\omega^2} \ ,$$

$$Y = \frac{\omega_B}{\omega} \ ,$$

$$Y_L = \frac{\omega_L}{\omega} cos(\theta) \ ,$$

$$Y_T = \frac{\omega_T}{\omega} sin(\theta) \ ,$$

$$Z = \frac{v}{\omega} \ .$$

The carrier frequency is represented by ω, ω_p is the plasma frequency, ω_B is the electron gyrofrequency, ω_T and ω_L are the longitudinal and transverse components of ω_B respectively, θ is the angle between the propagation direction and the direction of the geomagnetic field and v is the electron neutral collision frequency. All these frequencies are angular frequencies and are measured in radians per second. Several assumptions can be made to simplify the equation: at high altitudes the neutral gas density is low (high ionisation rate) and the electron-neutral collision frequency can be assumed to be negligible. The effects of the magnetic field can also be assumed to be negligible [12]. Thus (2.3) simplifies to μ, which represents only a real refractive index given by

$$\mu^2 = 1 - X = 1 - \frac{\omega_p^2}{\omega^2}. \tag{2.4}$$

If expanded, the higher order terms can be ignored since they only comprise less than 1% of the first-order term [12]. Therefore, μ^2 can be approximated as:

$$\mu \approx 1 - \frac{1}{2}X = 1 - \frac{1}{2}\frac{\omega_p^2}{\omega^2}. \tag{2.5}$$

The plasma frequency, f, expressed in Hz is given by

$$f_p^2 = \frac{e^2}{4\pi^2\epsilon_0 m_e}N \approx 9\sqrt{N}\ , \tag{2.6}$$

where e is the charge of an electron (1.602×10^{-19} C), ϵ is the permittivity of free space (8.854×10^{-12} F/m), m_e is the rest mass of an electron (9.107×10^{-31} kg) and N is the electron concentration in electrons per cubic meter (m^{-3}). Combination of the equation for the plasma frequency f and the refractive index μ provides an analytical expression for μ in terms of the carrier frequency f and the electron concentration N as

$$\mu = 1 - \frac{40.3}{f^2}N. \tag{2.7}$$

Following the procedure given in [13], the refractive index can be written in terms of the phase refractive index μ_p and the group refractive index μ_g as

$$\mu_p = 1 - \frac{40.3}{f^2}N\ , \tag{2.8}$$

and

$$\mu_g = 1 + \frac{40.3}{f^2}N. \tag{2.9}$$

Using the relation to speed of propagation given in (2.2), the group velocity and the phase velocity can be written as

$$v_p = \frac{c}{1 - \frac{40.3}{f^2}N}\ , \tag{2.10}$$

and

$$v_g = \frac{c}{1 + \frac{40.3}{f^2}N}. \tag{2.11}$$

Thus, in a GPS signal, the phase and group velocity differ from free-space propagation velocity in equal amounts. The signal modulated by the PRN codes and navigation messages is delayed and the carrier phase is advanced. The path length difference for the phase and group velocities can be calculated respectively. The path length S

between the satellite s and the receiver r due to the ionosphere can be defined as [6]

$$S = \int_r^s \mu \, dS. \tag{2.12}$$

The true geometric length can be defined as

$$p = \int_r^s 1 \, dS. \tag{2.13}$$

Thus, the path length difference, $\Delta S - p$, can be evaluated as

$$\Delta S - p = \int_r^s \mu \, dS - \int_r^s 1 \, dS. \tag{2.14}$$

Substituting for the appropriate value of μ, the phase and group path length differences are given respectively by:

$$\Delta S_p = \int_r^s (1 - \frac{40.3}{f^2} N) \, dS - \int_r^s 1 \, dS \tag{2.15}$$

$$\Delta S_g = \int_r^s (1 + \frac{40.3}{f^2} N) \, dS - \int_r^s 1 \, dS \tag{2.16}$$

ΔS_p and ΔS_g are small in comparison with the true path length ($\approx$ 20000 km vs. $\approx$ 10 m), thus dS can be changed to dl and the equation can be simplified by integrating along the line-of-sight path [6]. ΔS_p and ΔS_g can be respectively expressed as

$$\Delta S_p = -\frac{40.3}{f^2} \int_r^s N \, dl \ , \tag{2.17}$$

and

$$\Delta S_g = \frac{40.3}{f^2} \int_r^s N \, dl. \tag{2.18}$$

In (2.1) TEC was defined as $\int_r^s N \, dl$. Thus these equations can further be simplified to

$$\Delta S_p = -\frac{40.3}{f^2} I \ , \tag{2.19}$$

and

$$\Delta S_g = \frac{40.3}{f^2} I. \tag{2.20}$$

If the actual distance to the satellite were known, the TEC could be obtained directly from (2.19) and (2.20). However, this quantity is not known and only pseudo-range

measurements are available. These pseudo-ranges are calculated from information received by the satellite that contains the exact time the message was transmitted. The receiver uses the time difference with respect to its own internal clock to calculate the distance, assuming the wave travels at the speed of light [6]. For each satellite, the dual-frequency GPS receiver, derives two pseudorange observables (P_1 and P_2) and observables (L_1 and L_2). These observables are related to the true satellite to receiver range ρ as follows::

$$P_1 = \rho + \Delta S_{g,1} + \tau_1^r + \tau_1^s \ , \tag{2.21}$$

$$P_2 = \rho + \Delta S_{g,2} + \tau_2^r + \tau_2^s \ , \tag{2.22}$$

$$L_1 = \rho + \Delta S_{p,1} + N_1\lambda_1 + \epsilon_1^r + \epsilon_1^s \ , \tag{2.23}$$

and

$$L_2 = \rho + \Delta S_{p,2} + N_2\lambda_2 + \epsilon_2^r + \epsilon_2^s. \tag{2.24}$$

The measured carrier phase ranges (expressed in units of length) on the L1 and L2 frequencies respectively are represented by L_i where $[i = 1, 2]$. P_i are the measured code ranges. The true geometrical range, clock offsets, troposphere delay and other negligible delays are represented by a non-dispersive delay term ρ. λ_i is the wavelength of the carrier and N_i represents the unknown integer cycle ambiguity. τ_i and ϵ_i are hardware delays in the receiver and transmitter. The difference between these measured quantities allows us to directly determine the TEC:

$$P_I = P_2 - P_1 = 40.3(\frac{1}{f_2^2} - \frac{1}{f_1^2})I + B_r + B_s \ , \tag{2.25}$$

and

$$L_I = L_1 - L_2 = 40.3(\frac{1}{f_2^2} - \frac{1}{f_1^2})I + (N_1\lambda_1 - N_2\lambda_2) + B'_r + B'_s \tag{2.26}$$

The code range offset P_I is absolute but very noisy [14]. L_I on the other hand is smooth, but can suffer from a significant unknown integer cycle ambiguity, represented by $(N_1\lambda_1 - N_2\lambda_2)$. This, however, can easily be fixed by mapping the L_I curve onto the P_I curve using a least squares fit [15] - a process referred to as levelling. In the MIDAS software package the levelling is performed by shifting L_I by a value equal to the difference between the mean of L_I and P_I. This is illustrated in Fig. 2.4. The values of P_I are used only to adjust the mean value of L_I to correct for the unknown bias terms in 2.26. The result is a single adjusted absolute TEC value per observation

given by

$$P_I^F = 40.3(\frac{1}{f_2^2} - \frac{1}{f_1^2})I + B_r + B_s. \tag{2.27}$$

However, B_r and B_s are respectively receiver and satellite inter-frequency biases and are defined as:

$$B_r = \tau_2^r - \tau_1^r,$$

and

$$B_s = \tau_2^s - \tau_1^s.$$

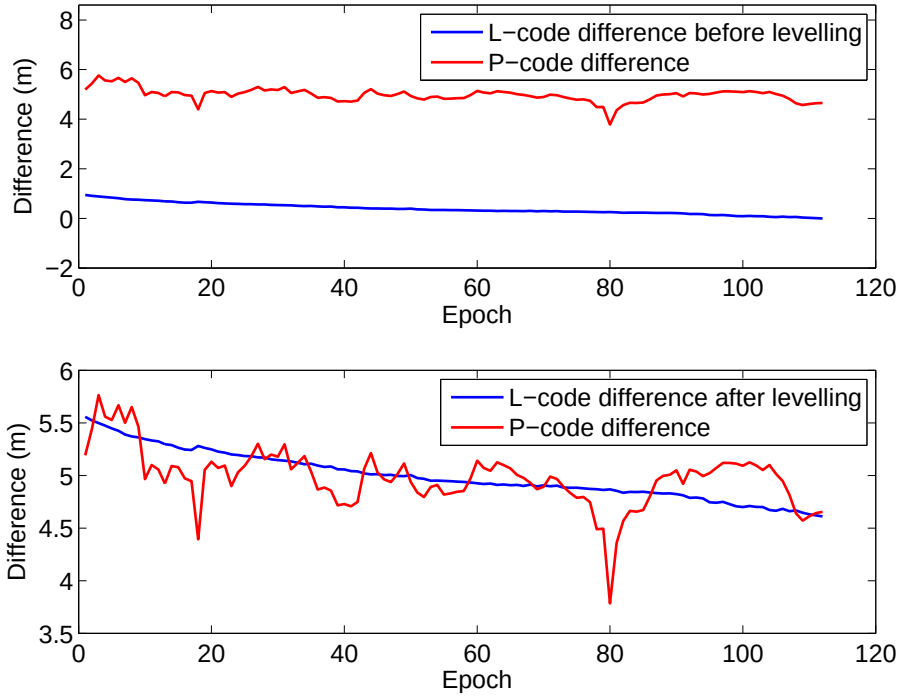

FIGURE 2.4: MIDAS levelling using the difference between the L_I mean and P_I mean as offset.

The interfrequency bias is a constant TEC offset which causes a shift in the absolute TEC level - an effect *similar* to the TEC phase ambiguity shown in Fig. 2.4. The bias is caused by hardware delays in the transmitter and receiver and is dependent on hardware characteristics. However, bias values differ between satellites and receivers since every device has unique hardware. Bias values as large as 30 TECU have been recorded. Clearly, estimating and correcting for these biases will form a very important part of the tomographic process. Estimating the bias is a subject that is discussed worldwide and estimation methods differ. For instance, if a terrestrial static GPS receiver is located close to an ionosonde (discussed in Section 2.3), the measurements

from the GPS and the ionosonde can be calibrated to estimate the bias of the receiver and satellites. However, when dealing with a mobile receiver which is not close to any other land-based measurement devices, this is not possible. Bias considerations and how the bias is estimated in MIDAS is discussed in Section 2.2.4.

2.2.3 TEC to electron density maps

Historically, the "thin shell" method was widely used to convert TEC measurements from GPS receivers to vertical TEC. Since the ray path from the satellite to the receiver is not perpendicular to the ionosphere, this ray path measures the slant TEC (STEC). The vertical TEC is defined as the STEC mapped to a level perpendicular to the ionospheric layer. The "thin shell" method models the ionosphere as an infinitely thin shell located at a fixed height above the Earth. Slant TEC values are obtained from GPS measurements and are mapped to vertical TEC on a 2-D plane by using a mapping function. This method, however, does not give a 3-D representation of the electron density in the ionosphere and although it is useful for GPS and other transionospheric error correction and space physics applications, it is of little value for HF communication path propagation prediction, which requires ray tracing through a 3-D ionosphere for the case where the exact position of the receiver is not known. This method also suffers from the uncertainty as to a suitable altitude for the thin shell.

Tomography is a technique first used in medical sciences, where a patient's body is irradiated with X-rays along a number of intersecting paths. From the absorption by the body of the X-rays along each ray path through the body, the density of the object can be "recreated" as a 3-D image. To explain this process, consider the 2x2 grid in Fig. 2.5 representing four columns of different density (indicated by j) in a four-element rectangular cylinder which is infinite in length in the direction perpendicular to the page. The quantity measured along each of the ray paths indicated by index i, is equal to the density represented by the number in the pixel multiplied by the length of the line passing through the block (similar to a line integral). The problem addressed by tomography is the determination of the unknown density in the block, given the series of observations of line integrals along lines that intersect each of the blocks of interest. Let i represent the indices of the projections, j the indices of the pixels, x_j the unknown density in the i^{th} pixel, A_{ij} the line distance in each pixel and b_i the measured line integral - then the following system of equations can be derived

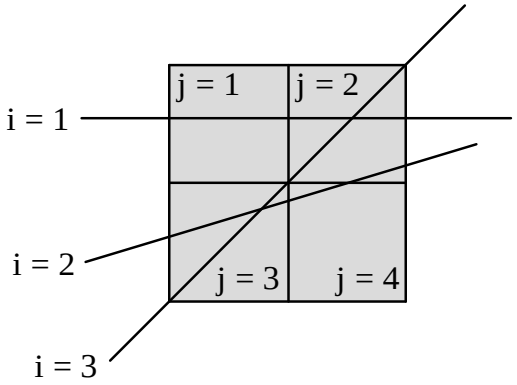

FIGURE 2.5: Simple example grid to illustrate CIT [14].

for the system shown in Fig. 2.5:

$$b_1 = A_{11}x_1 + A_{12}x_2 \ , \tag{2.28}$$

$$b_2 = A_{22}x_2 + A_{23}x_3 + A_{24}x_4 \ , \tag{2.29}$$

and

$$b_3 = A_{32}x_2 + A_{33}x_3. \tag{2.30}$$

This can be written in matrix form as:

$$\mathbf{Ax} = \mathbf{b} = \begin{bmatrix} A_{11} & A_{12} & 0 & 0 \\ 0 & A_{22} & A_{23} & A_{24} \\ 0 & A_{32} & A_{33} & 0 \end{bmatrix} \begin{bmatrix} x_1 \\ x_2 \\ x_3 \\ x_4 \end{bmatrix} = \begin{bmatrix} b_1 \\ b_2 \\ b_3 \end{bmatrix} \tag{2.31}$$

The coefficient matrix A is determined completely by the geometry of the pixels and the ray paths, and is independent of the densities in each of the pixels. If a sufficient number of projections can be obtained, the vector $\mathbf{x}$ of unknown densities can be solved by inversion of the matrix $\mathbf{A}$. Since TEC is effectively a line integral of the density of electrons along the ray path, this method can be directly applied to ionospheric tomography, where the measured quantity corresponds to the TEC, the projections correspond to the ray paths from the satellite to the receiver and the unknown quantity is the electron density in each voxel traversed by the ray paths [16]. The elements of the coefficient matrix $\mathbf{A}$ can generally be viewed as defining the relationship between the contribution to the slant TEC along the i_{th} ray path of the j_{th} voxel with electron

density x_j [17]:

$$A_{ij} = \frac{\delta b_i}{\delta x_j}. \tag{2.32}$$

However, because of the limited number of projections available from GPS, and the absence of horizontal projections, the matrix $\mathbf{A}$ can be highly ill-conditioned and thus be non-invertible. The solution can be constrained by incorporating some a priori information into the form of the unknown electron density $\mathbf{x}$.

Recently a new algorithm for 4-D time-dependent CIT, called MIDAS, was suggested [10]. This method builds on the basis of 2-D CIT, but also includes a time-dependent parameter in the inversion to account for variability in the ionosphere and of GPS satellite positions, so that it can incorporate TEC observations made at different times. As in the 2-D case, a grid of 3-D blocks is constructed. Each block in the grid is referred to as a voxel. These voxels are modelled by a 3-D version of (2.31), assuming that the electron concentration x_i within each voxel is constant. As mentioned earlier, the problem is that not all voxels contribute to a measurement - in other words, not all voxels are penetrated by rays from the satellites. Thus a priori information must be incorporated to constrain the inversion to acceptable solutions. The necessity of adding some a priori information to TEC measurements to perform tomographic image development has been demonstrated in [17]. In more recent studies this need was established analytically and several methods were developed to incorporate some external data into the tomographic process [18]. Basis functions are chosen to represent an initial rough approximation of the spatial electron distribution N_{e0}. Different weights are assigned to this rough approximation in order to match the basis functions to the measurements. It is known that the horizontal plasma structures in the ionosphere are statistically well presented by means of a power law spectrum, with spatial covariance equal to the Fourier transform of such a spectrum [19]. Thus the statistical properties can be used to weigh the influence of the measured quantities against the a priori information [19]. This property is used to interpolate or extrapolate from overdetermined voxels into underdetermined voxels. The method used in MIDAS was adapted from the stochastic inverse theory method proposed in [19], where a set of vertical orthonormal functions (Empirical Orthogonal Functions) created from known ionospheric models are used to model the vertical electron density distribution and the horizontal electron density distribution by a spherical harmonic expansion from a Fourier basis [10]. The Empirical Orthogonal Functions (EOFs) are used to model the vertical electron density profile. Some widely used models will be discussed in the next section.

2.2.4 The MIDAS inversion process

To explain the MIDAS inversion process, each aspect will briefly be discussed.

2.2.4.1 Empirical orthogonal functions (EOFs)

There are two one dimensional models integrated in the MIDAS package that can be used as EOFs: the Chapman model and the Epstein model. External models, such as the International Reference Ionosphere (IRI), can also be integrated into the MIDAS inversion as a basis function. Each of these models and its parameters will briefly be discussed.

Chapman Layer

As mentioned in Section 2.2.2 one of the best-known ionospheric electron density models is the Chapman layer model [9], developed by Sidney Chapman in 1931. In this model the ionosphere is characterised by using the balance between ionisation and recombination of the gases of the upper atmosphere. The simple nature of this layer was deducted from the relationship between exponentially decreasing neutral gas density and the increase in solar ionisation density as altitude increases. Fig. 2.6 illustrates the formation of the Chapman layer.

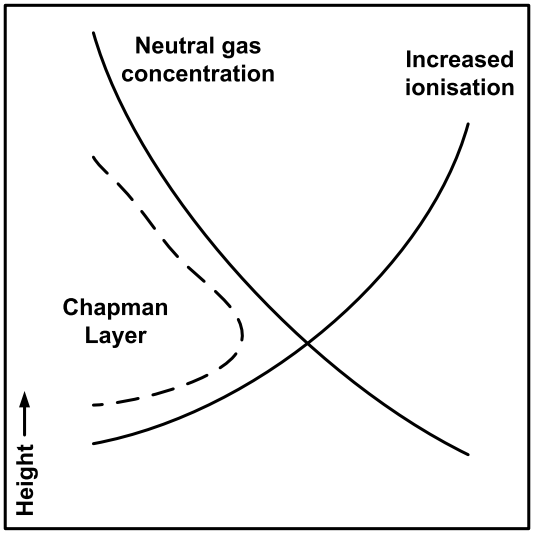

FIGURE 2.6: Representation of the Chapman layer based on the gas density and ionisation intensity as a function of height.

According to the Chapman model, the electron density distribution N with altitude h is given by:

$$N(h, X) = N_0 e^{(1-z-sec(\chi)e^{(-z)})} \quad where \quad z = \frac{(h - h_0)}{H} , \tag{2.33}$$

where N_0 is the peak electron density at height h_0, H is the scale height and χ is the solar zenith angle, i.e. the angle between the vertical direction (zenith) and the ray path from the sun as seen from the observation point. The scale height H is defined as the vertical distance over which electron density decreases by factor of e. Since the F layer is the layer with the highest electron density, with the F2 layer present in daytime, the peak height and scale height is usually referred to as h_mF2 and H_mF2 respectively.

Epstein profiles

In 1977 H.G Booker first suggested the use of a single analytical function to represent the vertical electron density profile [20]. It comprises a set of non-overlapping Epstein functions which are used to determine this single analytical function. In [20] Rawer maintains that this method is not economical and suggests the use of overlapping functions, reducing the complexity and parameters of the function. Epstein functions have similar characteristics similar to the Chapman profile - such as the peak electron density and the scale height. An in-detail discussion of Epstein functions is beyond the scope of this dissertation and the reader is referred to [20] for further reading.

International Reference Ionosphere (IRI)

The International Reference Ionosphere (IRI) is an international project sponsored by the Committee on Space Research (COSPAR) and the International Union of Radio Science (URSI). This project was started in the mid-sixties because of the need for a model that specified ionospheric and thermospheric parameters for the design and control of space-based instrumentation [21]. The model comprises a monthly average of the ionospheric conditions based on various measurements made by ground- and space-based instrumentation. Some of the more recent satellites, equipped with instruments for space-based ionospheric measurements, that the IRI uses include KOMPSAT, ROCSAT and TIMED. The IRI model provides averages of the electron density, ion composition (O^+, H^+, N^+, He^+, O_2^+, NO^+, $Cluster^+$), ion drift and ion temperature in the range 60 km - 1 000 km [22]. The IRI model source code is freely available

from the IRI webpage (`http://modelweb.gsfc.nasa.gov/ionos/iri.html`) - the latest version released is IRI2007. Fig. 2.7 shows an example of the electron density profile over Marion Island (geographic coordinates: $-46.8750°$ latitude, $37.7983°$ longitude) obtained from the IRI2007 model for the period 01:00 to 06:00 UT on 2010-01-01.

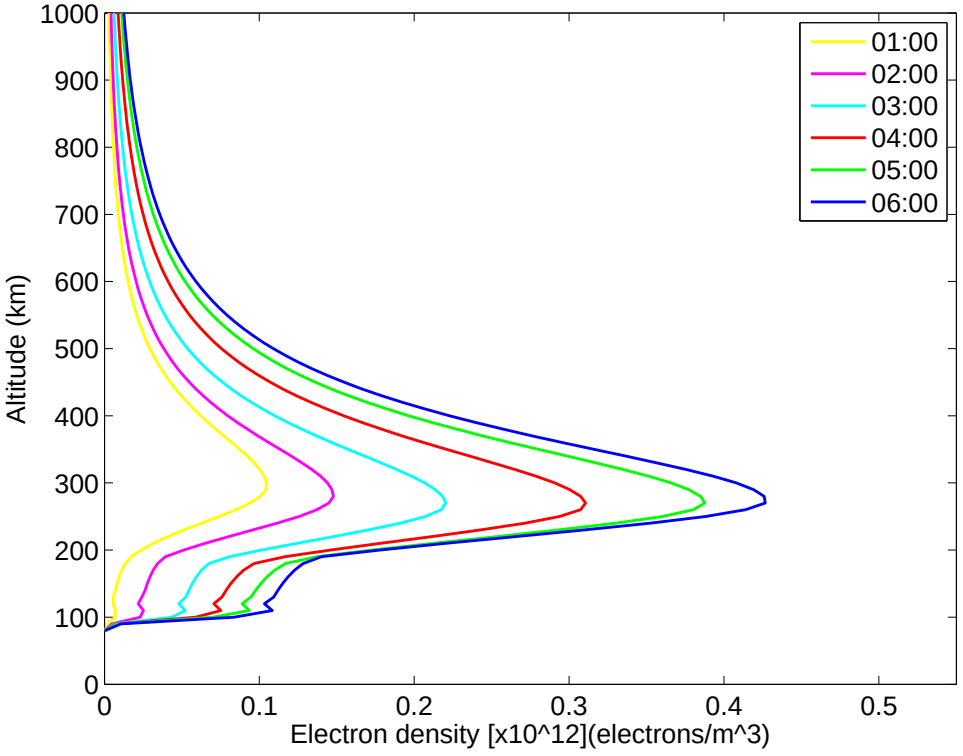

FIGURE 2.7: Vertical electron density profile generated by the IRI2007 model for Marion Island for the period 01:00 - 06:00 UT on 2010-01-01.

2.2.4.2 Matrix inversion

Following the procedure outlined in [10], using the basis functions to transform the original problem, and using an orthonormal presentation for $\mathbf{x}$ ($\mathbf{x} = \mathbf{XW}$), the inversion problem is now transformed from the form in (2.32) to that shown in (2.34):

$$\mathbf{b} = \mathbf{AXW} \ , \tag{2.34}$$

where $\mathbf{W}$ represents the relative contributions (weights) of the basis functions. The variable $\mathbf{X}$ in (2.34) contains the basis functions. $\mathbf{AX}$ defines the basis set of line integrals of electron density. The relative contributions of the basis functions, $\mathbf{W}$, can

be defined as

$$\mathbf{W} = (\mathbf{AX})^{-\mathbf{1}}\mathbf{b} \ , \tag{2.35}$$

where $\mathbf{W}$ is the maximum likelihood solution for the inverse matrix $(\mathbf{AX})^{-\mathbf{1}}$. $\mathbf{AX}$ can be decomposed by applying singular value decomposition (SVD) - LU decomposition can also be used - to the inverse of the matrix to obtain two orthogonal matrices $\mathbf{V}$ and $\mathbf{U}$, with a diagonal matrix of singular values, $\mathbf{w}$ [10]:

$$(\mathbf{AX})^{-\mathbf{1}} = \mathbf{V}(diag(\frac{1}{\mathbf{w}}))\mathbf{U}^T. \tag{2.36}$$

The relative contributions of the basis functions $\mathbf{W}$ can now be found by matrix inversion:

$$\mathbf{W} = (\mathbf{AX})^{-\mathbf{1}}\mathbf{b} = (\mathbf{V}(diag(\frac{1}{\mathbf{w}}))\mathbf{U}^T)b. \tag{2.37}$$

The unknown electron density $\mathbf{x}$ can now be retrieved using the orthonormal presentation. The time-dependency is implemented in a similar manner by defining a matrix where the change in TEC ($\mathbf{c}$) is a function of the differences in ray path geometry $\mathbf{D}$ and the change in electron density $\mathbf{y}$ [10]:

$$\mathbf{Dy} = \mathbf{c} \tag{2.38}$$

This equation is solved for $\mathbf{y}$ using a similar method - by converting the matrix to an orthonormal presentation and solving for $\mathbf{G}$ in

$$\mathbf{DXG} = \mathbf{c} \ , \tag{2.39}$$

where the unknown term $\mathbf{G}$ represents the linear changes in coefficients of basis functions:

$$\mathbf{G} = (\mathbf{DX})^{-\mathbf{1}}\mathbf{c}. \tag{2.40}$$

Thus,

$$\mathbf{y} = \mathbf{XG}. \tag{2.41}$$

Fig. 2.8 shows a vertical TEC map generated by MIDAS during a magnetic storm on 2000-07-15.

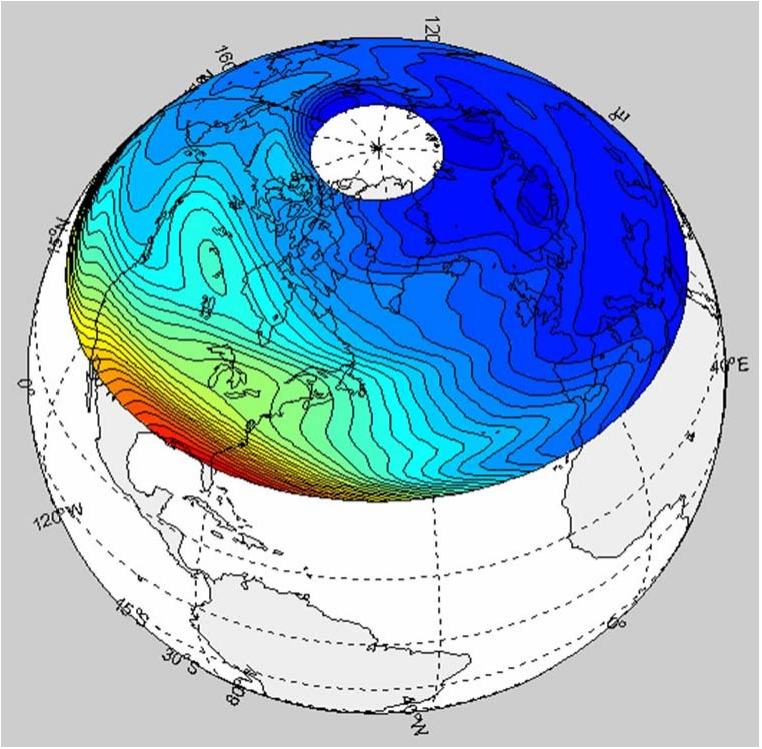

FIGURE 2.8: Total electron content (in TECU) 2000-07-16 at 00:00:00 - generated by MIDAS [23]. The colours indicate different TEC values.

2.2.4.3 Estimation of interfrequency biases

The receiver and satellite biases, B_r and B_s, are shown in (2.27) and discussed in Section 2.2.2.1. In essence, the MIDAS inversion solves the following simplified equation given in Section 2.2.3:

$$\mathbf{Ax} = \mathbf{b}.$$

However, in the inversion process, $\mathbf{x}$ is converted to $\mathbf{XW}$, where $\mathbf{X}$ represents the basis functions and $\mathbf{W}$ represents the relative contributions (weights) of the basis functions. The inversion does not always produce a perfect match between the measured STEC and the relative contributions of the basis functions. Therefore, a residual vector $\mathbf{z}$ can be defined as the difference between the observations and the inversion results:

$$\mathbf{Ax} - \mathbf{b} = \mathbf{z}. \tag{2.42}$$

MIDAS assumes that each component of the residual vector z_i is the sum of one unique receiver bias and one unique satellite bias [14]. Thus, a system of equations can be

formed to determine the sum of the satellite and receiver biases as unknowns:

$$\mathbf{B_r} + \mathbf{B_s} = \mathbf{z} = \begin{bmatrix} B_{r1} & B_{s1} \\ B_{r2} & B_{s2} \\ B_{r3} & B_{s3} \\ \dots & \dots \end{bmatrix} = \begin{bmatrix} z_1 \\ z_2 \\ z_3 \\ z_4 \end{bmatrix} \tag{2.43}$$

Although each satellite-receiver pair can be determined uniquely, the solutions for each satellite and receiver are non-unique, since there are fewer independent equations than unknowns. However, to obtain more accurate values of the unique satellite and receiver biases, the mean of these biases can be calculated over a longer period. Fig. 2.9 shows an example of the mean bias obtained with data from the Binyamin Shmuter (BSHM) GPS receiver in Israel over a period of 24 hours. The dark green line represents the mean interfrequency bias for the receiver computed over 24 hours. The red points represent an estimate of the interfrequency bias for each hour, and the green points indicate that no solution was possible [14]. It is clear that the hourly bias can differ from the daily mean bias by as much as 8 TECU. The daily mean TEC calculated here is broadly in agreement with values found in the literature.

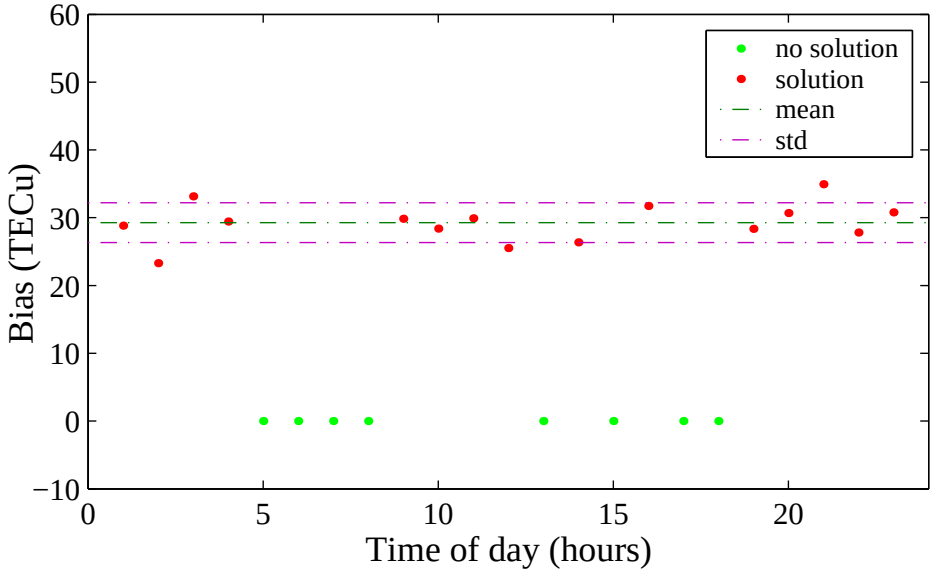

FIGURE 2.9: Interfrequency code biases computed for receiver BSHM on 2001-03-28. Taken from [14], with permission.

Once bias values have been obtained, these can be subtracted from the observed slant TEC value to obtain the true slant TEC.

2.3 OTHER ELECTRON DENSITY MEASUREMENT TECHNIQUES

Several other techniques are currently used to characterise the ionosphere. These include ionosondes, incoherent scatter radars and satellites. To appreciate the simplicity of using GPS signals for tomography, the basic principles of each of these methods will now be discussed.

2.3.1 Ionosondes

The ionosphere allows signals transmitted above a certain frequency to pass through from the bottomside - this is called the critical frequency. Any frequency below the critical frequency will be reflected from the ionosphere at a discrete height from different layers of ionisation [12]. The critical frequency is proportional to the electron density in the ionosphere. As the frequency of the signal increases, it penetrates the ionosphere further to where the electron density is higher, until it eventually passes through the ionosphere and exits into space. This property of the ionosphere is used to map the electron density from the bottomside by using ionosondes. Ionosondes provide the simplest way of characterising the ionosphere. The ionosonde transmits signals at different frequencies and receives reflections from the ionosphere. It uses the delay t of the transmitted signal relative to the received (reflected) signal to calculate the height h' at which the wave was reflected by assuming that the wave travels of at the speed of light c i.e.,

$$h' = \frac{ct}{2}.$$

This height is called the virtual height, since the wave is not only reflected, but is also propagated through a series of refractive layers, eventually returning to Earth. An illustration of virtual height is shown in Fig. 2.10. A series of signals at different frequencies are transmitted and an electron density profile is obtained. An example of such a profile is shown in Fig. 2.11.

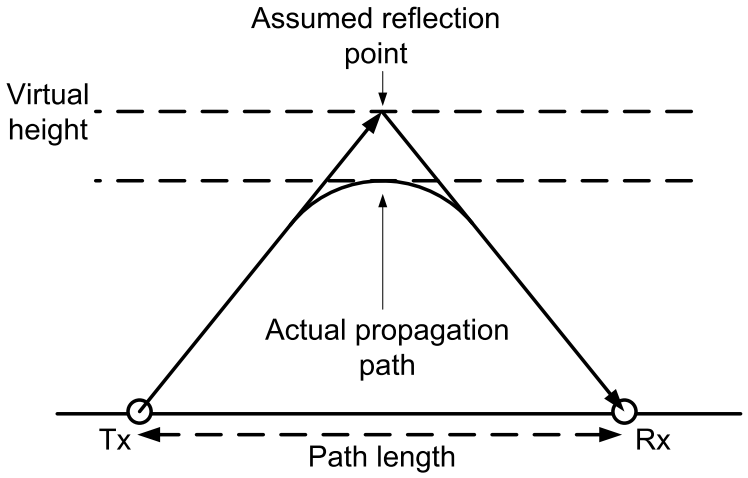

FIGURE 2.10: Virtual height geometry of the skywave path.

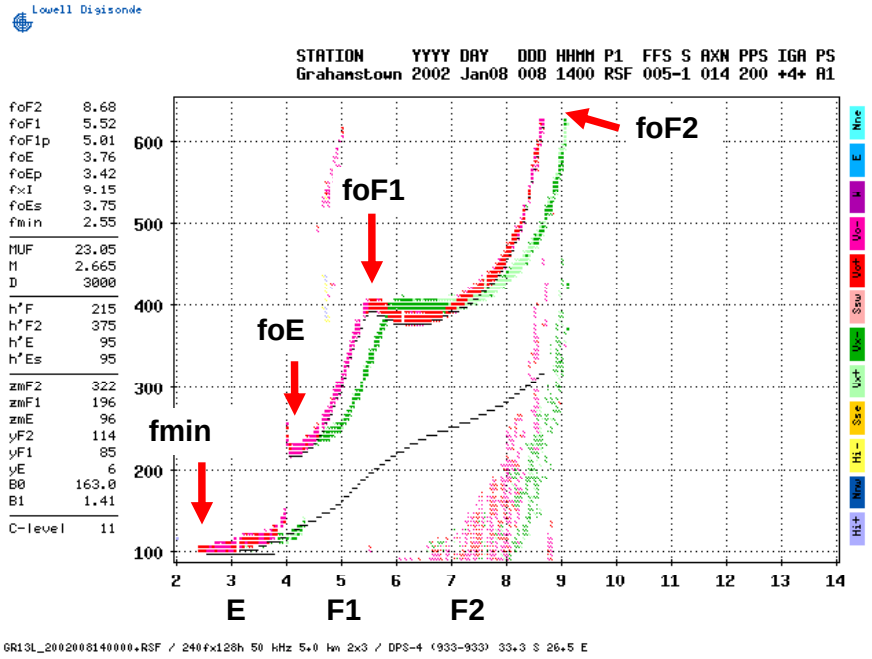

FIGURE 2.11: Ionogram of virtual height as a function of frequency - Grahamstown. The peak frequency for each layer is shown and characterised by frequency on the x-axis and height to which it travels on the y-axis. Taken with permission from the Hermanus Magnetic Observatory.

The maximum usable frequency (MUF) is defined as the upper frequency limit that can be used for communication between two points and is calculated from the critical frequency by multiplying by a MUF factor which is a function of the transmission distance [2]. The maximum electron density can be found by using the approximation:

$$f_c \approx 9 \times 10^{-6} \sqrt{N_m} \ , \tag{2.44}$$

where f_c is the critical frequency in megahertz, and Nm is the peak electron density expressed in electrons per cubic meter ($/\mathrm{m}^3$). Ionosondes can only characterise the ionosphere from the bottom and can only obtain ionograms up to $foF2$, the critical frequency of the F2 layer. This drawback of the ionosonde does not allow the determination of the topside electron density profile from ionosonde measurements. A conversion of the various critical frequencies are performed in order to obtain the electron density.

2.3.2 Incoherent scatter radars

Incoherent scatter radars (ISR) are ground-based instruments that are used to measure various properties of the ionosphere. ISR's, unlike ionosondes, can obtain measurements from the topside ionosphere and can also measure a variety of parameters such as neutral density, temperature and composition [9]. Incoherent scatter radars take advantage of the fact that electrons are capable of scattering electromagnetic waves. The radar beam creates an incoherent scatter echo, which is detected by the receivers. These echoes are extremely weak, and as a result large receiver antennas and high-powered transmitters are necessary. To build and operate incoherent scatter radars is extremely expensive and this limits the number of ISR's currently in operation - there are currently no ISR's in Africa. The reader is referred to [9] for more information regarding incoherent scatter radars.

2.3.3 Rockets and satellites

Several satellites have been and are currently operating as topside sounders of the ionosphere. These include ATS1, ATS3, GOES, SIRIO, ATS6, ETS II, KOMPSAT, ROCSAT and TIMED [9]. Satellites, however, are expensive to build and operate and have a very limited resolution due to its long orbit duration. Rockets make *in situ* measurements of irregularities not easily measured by ionosondes - such as the

sporadic E-layer [9]. Rockets, however, are also expensive to build and only provide a single measurement data set per launch.

2.4 IONOSPHERIC TOMOGRAPHY AND A MOBILE RECEIVER

All current ionospheric measurement techniques discussed in Section 2.3 (ionosondes, incoherent scatter radars, rockets and satellites) and currently used dual-frequency GPS receivers are limited to fixed land-based stations. Since the ocean covers 70.8% of the Earth's surface, only approximately 29.2% of the ionosphere can be characterised by land-based instruments. The coverage is even worse in the southern hemisphere, where the ratio of land to ocean is one to four. Fig. 2.12 shows the theoretical South Atlantic GPS dual-frequency receiver coverage by island- and continent-based GPS receivers. An ionospheric peak density height of 350 km is assumed with a signal elevation angle cutoff of 10 degrees. Only GPS signals 10 degrees above the horizon are taken into account.

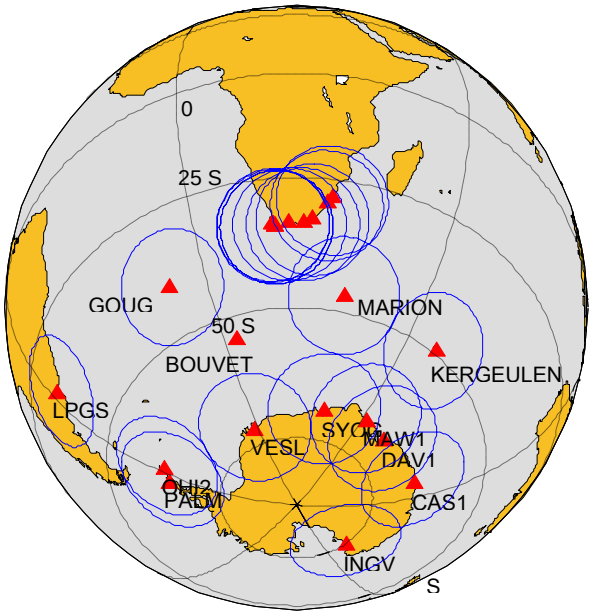

FIGURE 2.12: Theoretical South Atlantic GPS dual-frequency receiver coverage by island- and land-based GPS receivers. An ionospheric peak density height of 350 km is assumed with a signal elevation angle cutoff of 10° - with permission from [4].

Employing mobile GPS dual-frequency receivers on various vessels traversing the Atlantic Ocean on a daily basis, would compliment observations collected by the receivers shown in Fig. 2.12. To test the viability of using a mobile GPS receiver for ionospheric tomography, a dual-frequency GPS receiver was installed on the SA Agulhas, the South African polar research vessel.

2.4.1 Mobile and static GPS receivers

One of the possible advantages of using mobile GPS receivers as opposed to static receivers lies in the ability to have a much higher spatial resolution of observations per time interval. For a fixed observation time, the angular resolution of the measured STEC for a mobile receiver will be higher, thus providing more observations of the distribution of electrons. To illustrate, consider the following scenario. Fig. 2.13 shows the signals reaching a static receiver in a two-dimensional plane as the GPS satellite is in orbit for three sampling intervals.

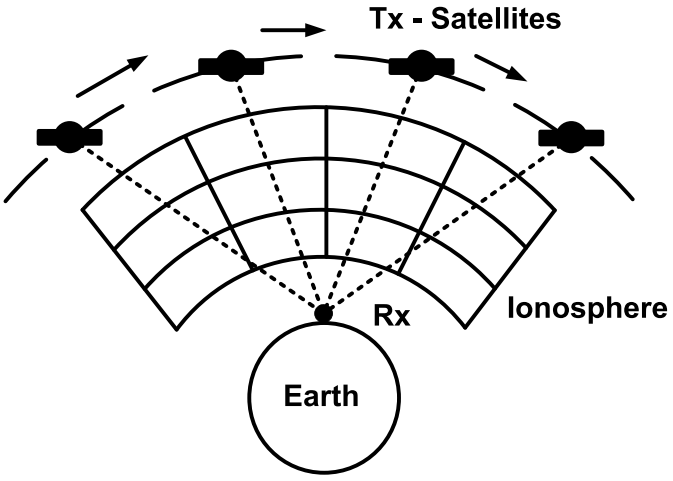

FIGURE 2.13: A simplified 2-D representation of the signals received by a static receiver for a duration of three sampling intervals.

Fig. 2.14 shows the signals reaching a mobile receiver as the GPS satellite is in orbit for three sampling intervals. The assumption is that in the 2-D plane, the satellite and the mobile receiver move in opposite directions.

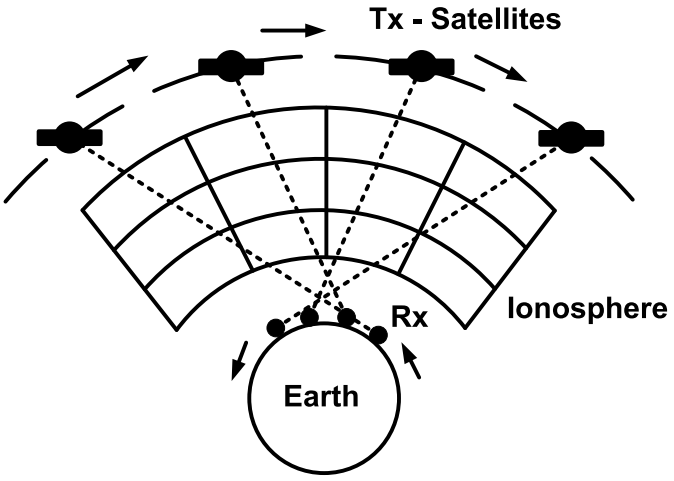

FIGURE 2.14: A simplified representation of the signals received by a mobile receiver for a duration of three sampling periods.

It can be seen that the voxels in Fig. 2.14 have a slightly higher angular coverage than provided by its static counterpart shown in Fig. 2.13. It can be argued that the initial movement of the receiver would cause the voxel block on the right-hand side of the 2-D grid in Fig. 2.14 to have only one epoch observation (caused by the movement of the receiver away from this block). However, the number of measurements per voxel is dependent upon the voxel resolution, the receiver speed and the sampling rate. Although a major difference in the number of signals penetrating the voxels is not clearly visible in this simplified example, the possible increase in spatial resolution is shown.

Chapter 3 presents verification of the modified MIDAS package by simulation and Chapter 4 by experimental work. The simulations in Chapter 3 theoretically compare a static and a mobile receiver.

2.4.2 Multi-Instrument Data Analysis System (MIDAS) for mobile receivers

The author of this dissertation compiled a new MATLAB package for preprocessing observations from mobile GPS receivers. To perform tomographic inversion with MIDAS as discussed in Section 2.2.3, the MIDAS package had to be adapted for a mobile GPS receiver. The use of observations from a mobile GPS receiver differs in several aspects from the use of observations from a static GPS receiver.

- **Data quality**
  Static receivers have been in use for some time, and the GPS observables obtained from these receivers have a certain accepted quality. However, with a mobile receiver, this is the first time that a receiver is on a mobile platform and data quality analysis and filtering will form an important aspect of the inversion process. The data may exhibit erratic behaviour and this must be quantified and analysed. An analysis of the data quality is presented in Chapter 4.

- **Static vs. changing position**
  With static receivers, MIDAS uses the same static receiver position and satellite orbit positions. However, with a mobile receiver, every observation has a unique receiver position associated with it. It is therefore very important that the position matches the epoch (a single observations of slant TEC by a single ray path from transmitter to receiver), or results will be inaccurate. It may also be the case that the receiver location is not always directly available (due to logging problems or missing data) for each epoch and some processing may have to be performed to determine its position.

- **Data format**
  With multiple data formats needed to store GPS observations - such as GPS parameters, position and data quality - it is important to preprocess the raw data for use in the MIDAS software.

2.5 CONCLUDING REMARKS

In this chapter a brief overview of the theoretical aspects of space physics and of the algorithms which form the basis for this research were presented, including the ionosphere, the South Atlantic Anomaly (SAA) and GPS ionospheric tomography. The MIDAS inversion process and the parameters that have an influence on results were discussed. A number of other ionospheric characterisation techniques were described with regard to how they differ from ionospheric tomography.

CHAPTER 3

ALGORITHM VERIFICATION - SIMULATIONS

In this chapter, an initial simulation based verification for the use of the MIDAS package for a mobile receiver is presented. A model ionosphere was created using the IRI2007 model and used to calculate slant TEC values, using measurements from a simulated mobile GPS receiver and the actual GPS satellite orbits. The slant TEC values obtained from the IRI2007 model ionosphere were inverted using MIDAS to obtain electron density maps. These maps were compared to the known IRI2007 electron density maps. The influence of the speed, sampling interval and whether the receiver is static or mobile on the accuracy of the electron density maps was analysed.

3.1 METHOD

The model ionosphere generated from the IRI2007 model is shown in Figs. 3.1 and 3.2. These figures were produced using the electron density map generated by the IRI2007 model at 12:30 UT on 2010-01-01 over Gough Island. The simulated receiver is located on route to Gough Island (37°S, 12°W). To simulate the vertical movement of a mobile receiver (for instance due to the influence of wave motion on the level of the ship), random "noise" on the uniform distribution interval 0-8 m was added to the height of the mobile receiver. The IRI2007 electron density map will henceforth be referred to as the simulated electron density map.

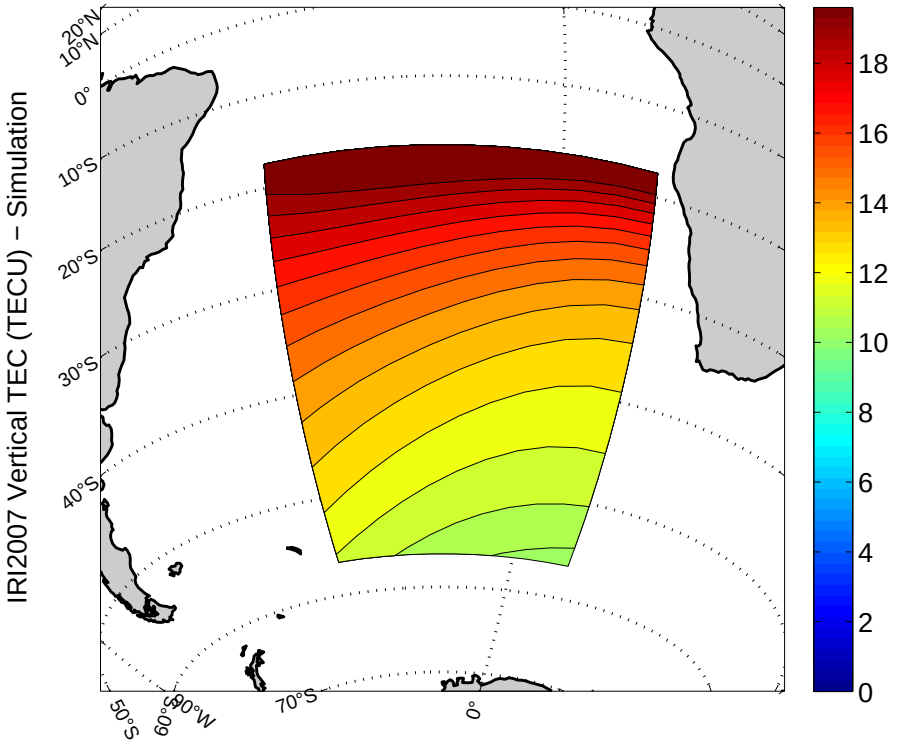

FIGURE 3.1: IRI2007 vertical TEC map over Gough Island at 12:30 UT on 2010-01-01 (day of year 1). The colours indicate total electron content in TECU.

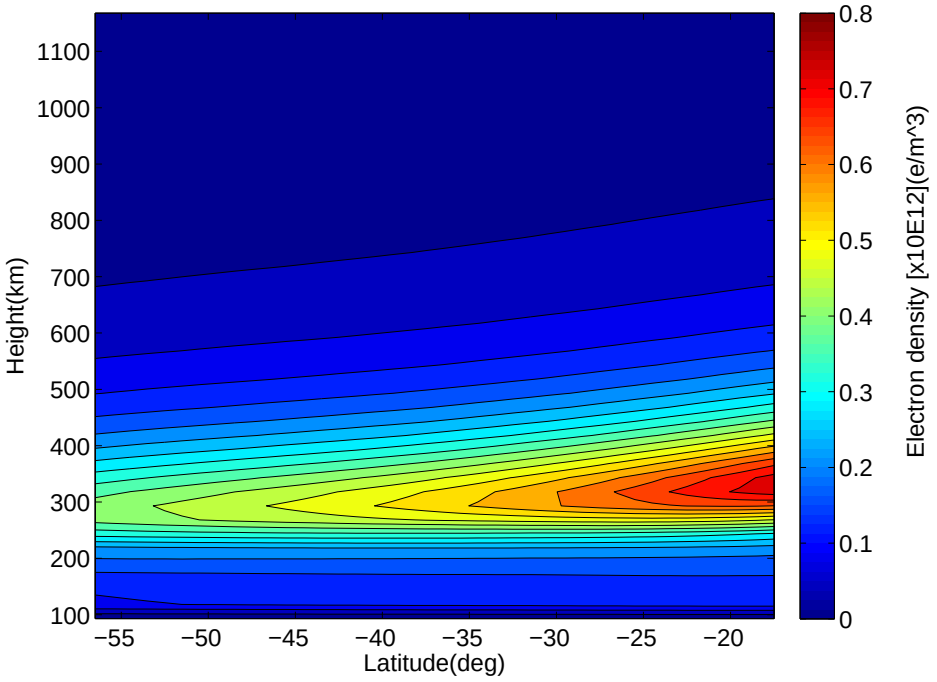

FIGURE 3.2: IRI2007 electron density distribution for a longitude of 30 degrees at 12:30 UT on 2010-01-01 (day of year 1). The colours indicate electron density ($\frac{\times\times 10^{12}}{\mathrm{m}^3}$).

As described in Chapter 2, ionospheric tomography is not a simple process. There are many factors that influence the inversion and as a result, a number of assumptions have to be made to successfully quantify ionospheric tomography. In this study the author has tried to take into account and quantify as many factors as possible. Unfortunately, some of these factors are not controllable and thus the factors that are controllable have to be relied on to obtain optimal results. The following elements of the tomography process were considered. A brief discussion of each follows.

- Satellite elevation cutoff angle
- Inversion grid range
- Ionospheric structure dimensions (not controllable)
- Data collection period
- Ray path density
- Sampling time
- Mobile receiver speed and direction
- Basis functions (Empirical Orthogonal Functions - EOFs)
- Interfrequency bias (Section 2.2.4.3)

Satellite elevation angle cutoff

Multipath is a phenomenon where signals from the satellite are reflected off a reflective surface and are added to the signals received on a direct path from the transmitter. This is a common problem especially on the oceans - the surface of the ocean is one continuous reflective body and the upper structure of a ship provides many reflective surfaces which may be above the level of the GPS antenna. These signals cause errors in the estimated pseudorange and phase. Multipath is more likely in signals originating from a low elevation angle above the horizon. Although multipath is not an issue for a simulated receiver, only simulated ray paths above a certain elevation angle are considered. Any signal received from a satellite below this elevation angle is removed from the STEC data set. Multipath for an actual GPS receiver is discussed in Chapter 4.

Inversion grid range

The inversion grid is the three dimensional geographical area of the ionosphere that MIDAS uses for the inversion. Due to the shape of the Earth, only the area above the horizon visible from the receiver can be penetrated by ray paths. As a result, the geographical range for which STEC values are available are limited by the visibility of GPS satellites above the horizon. If an inversion is performed outside this range, the results will not be a direct product of actual observations but of the predicted change in electron density in that direction. Thus, the optimal distance from the receiver where a reasonably trustworthy inversion can be performed must be found. The criteria for this level of confidence may differ, however, for this study the accuracy and availability of STEC values were considered. To ensure that the ray paths and corresponding STEC values available cover most of the inversion grid, the grid was initialized so that at the receiver position, halfway through the time of observation, the lowest ray path included in the data (filtered by the *Satellite elevation angle cutoff* explained above) would penetrate the edge voxel in the chosen grid, starting at a known height (from the lower limit to the upper limit, depending on grid model used, see *initgrid.m*). To calculate this distance, the Earth is modelled as a flat surface and all distances are assumed to be linear rather than following the curvature of the Earth. The incidence angle is specified by the MIDAS user using the *Satellite elevation angle cutoff* as well as the height. Thus, by using simple trigonometry, the distance from the receiver can be calculated. This is shown in Fig. 3.3.

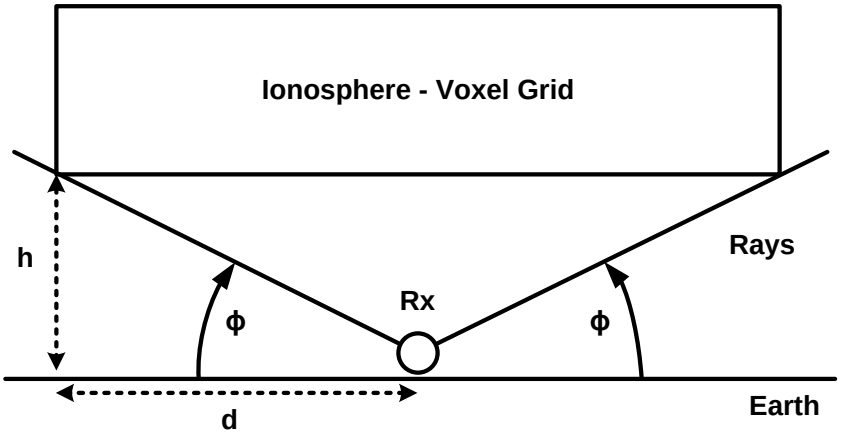

FIGURE 3.3: Calculation of the horizontal limits of the inversion grid used with a simulated receiver. For a mobile receiver (Rx), the receiver location is taken as its position halfway through the period of observation.

Since h (grid initialization and ionospheric height) and the angle ϕ (*Satellite elevation*

angle cutoff) is known, the distance d can be calculated according to

$$d = \frac{h}{tan\phi}. \tag{3.1}$$

This distance d is used for the horizontal limits of initializing the inversion grid.

Ionospheric structure dimensions (not controllable)

Structures such as peaks and troughs in electron density are typically found in the ionosphere. The geometric dimensions of these features play an important role in the inversion process, since they determine how many rays pass through these structures. A variation in the dimensions of the features (peaks and valleys in the electron density) will result in more or fewer ray paths traversing the features, thus influencing the amount of information about each structure available for the inversion. Unfortunately, in the ionosphere these dimensions are uncontrollable and the controllable variables of the algorithm - such as voxel density and sampling interval - have to be adapted to get optimal results.

Data collection period

The ionosphere is a dynamic medium affected by multiple factors beyond human control - such as coronal mass ejections originating from the Sun. The ionospheric properties can be approximated as being stationary on a time scale of minutes, but the variation in consecutive slant TEC values from ray paths are small due to the long orbit times of the GPS satellites [14]. The typical observation span from a high-elevation satellite is approximately 30 degrees per hour. The difference between subsequent STEC observations at intervals of a minute or less is therefore insignificant. Thus, STEC observations taken at short intervals have a very low spatial resolution and the capture of adequate changes in electron density which are needed successfully reproduce an electron density map that conveys the changes in the ionosphere are limited. For this reason, a time-dependant parameter was introduced into the MIDAS algorithm and only blocks of STEC values spanning an hour are used for inversions. For a mobile receiver, the movement of the receiver during the hour must be considered, whereas a static receiver measures the data at the same position for an hour.

Ray path density

The ray path density is defined as the number of ray paths passing through the grid

for which the inversion is performed. This concept is explained in Figs. 2.13 and 2.14 for a static and a mobile receiver respectively. Following from the MIDAS inversion process as discussed in Section 2.2.3, as more ray paths pass through the inversion grid, more STEC values are available and more information regarding the change in electron density is available. The electron density map obtained via inversion becomes less dependent on the choice of basis functions and more on the STEC values obtained.

Sampling interval

The sampling interval is the time interval between the samples the GPS receiver selects from the GPS observables received from the GPS satellite. Referring to Figs. 2.13 and 2.14, theoretically, if the signal is sampled more often, more ray paths will pass through the inversion grid. However, decreasing the duration of the sampling interval will increase the required processing power and time, as well as storage space. Additionally, subsequent slant TEC samples taken at a very short sampling interval do not differ significantly, so the increase in available observables is not proportional to the increase in the size of the matrix that needs to be inverted. Ideally, a trade-off between the sampling interval, processing power and performance gain should be reached.

Mobile receiver speed and direction

Theoretically, the speed at which the receiver is moving will have an effect on the ray path density and coverage angle obtained. As the speed of the receiver decreases, the characteristics will resemble that of a static receiver more closely and with the same resolution as a static receiver. The degree of influence this will have on the result was verified and is discussed in Section 3.2.3.

Basis functions

The importance of the basis functions used in the MIDAS inversion is discussed in Section 2.2.3. To determine optimal basis function parameters, the influence of different parameters on the accuracy of electron density maps obtained by inversion were analysed. This analysis is presented in Section 3.1.2.

Interfrequency bias

For the simulation, the effect of transmitter or receiver differential code biases was not considered. Biases will be discussed and analysed in Chapter 4.

3.1.1 Performance evaluation

The purpose of the simulations were to compare the electron density maps obtained through inversion with those of the IRI2007 model (known) ionosphere - thus to evaluate the performance of the inversion algorithm and its dependence on the various controllable parameters, before it is applied to GPS observables obtained from a real receiver presented in Chapter 4. Initially, quantitative and qualitative analyses were performed. The quantitative analysis was based on the root mean square (RMS) electron content voxel-per-voxel difference between the electron density map generated by inversion and the one based on the IRI2007 model ionosphere. However, it was found that the differences in RMS values were very small (in the order of approximately 0.01×10^{12} $\frac{\text{e}}{\text{m}^3}$) and did not seem to provide conclusive results. To illustrate, consider Fig. 3.4. Fig. 3.4(a) shows the MIDAS-obtained vertical TEC map for a sampling interval of 30 seconds and Fig. 3.4(b) shows the MIDAS-obtained vertical TEC for a sampling interval of 3600 seconds. The RMS difference between the voxel-per-voxel electron density map of the VTEC map shown in Fig. 3.4(a) and the model ionosphere is 0.0722×10^{12} $\frac{\text{e}}{\text{m}^3}$, and 0.0697×10^{12} $\frac{\text{e}}{\text{m}^3}$ for the result in 3.4(b). The difference is 0.0025×10^{12} $\frac{\text{e}}{\text{m}^3}$ - a mere 0.3% of the maximum electron density (0.82113×10^{12} $\frac{\text{e}}{\text{m}^3}$) of the IRI2007 model ionosphere. However, if the VTEC maps in Fig. 3.4 are studied, there is a clear difference in electron distribution which is not apparent from the quantitative results. At low latitudes, the VTEC obtained with a sampling interval of 30 seconds clearly has a higher correlation with the model VTEC in Fig. 3.4(c). At higher latitudes, the VTEC map with a sampling interval of 3600 seconds seems to have a better correlation with the model VTEC. This does not produce a conclusive result. Thus, only qualitative analysis methods will be used in this chapter. The qualitative analysis involves comparing VTEC maps obtained from electron density maps. The best value for the parameter being evaluated will be chosen by visually (qualitative) comparing the VTEC maps.

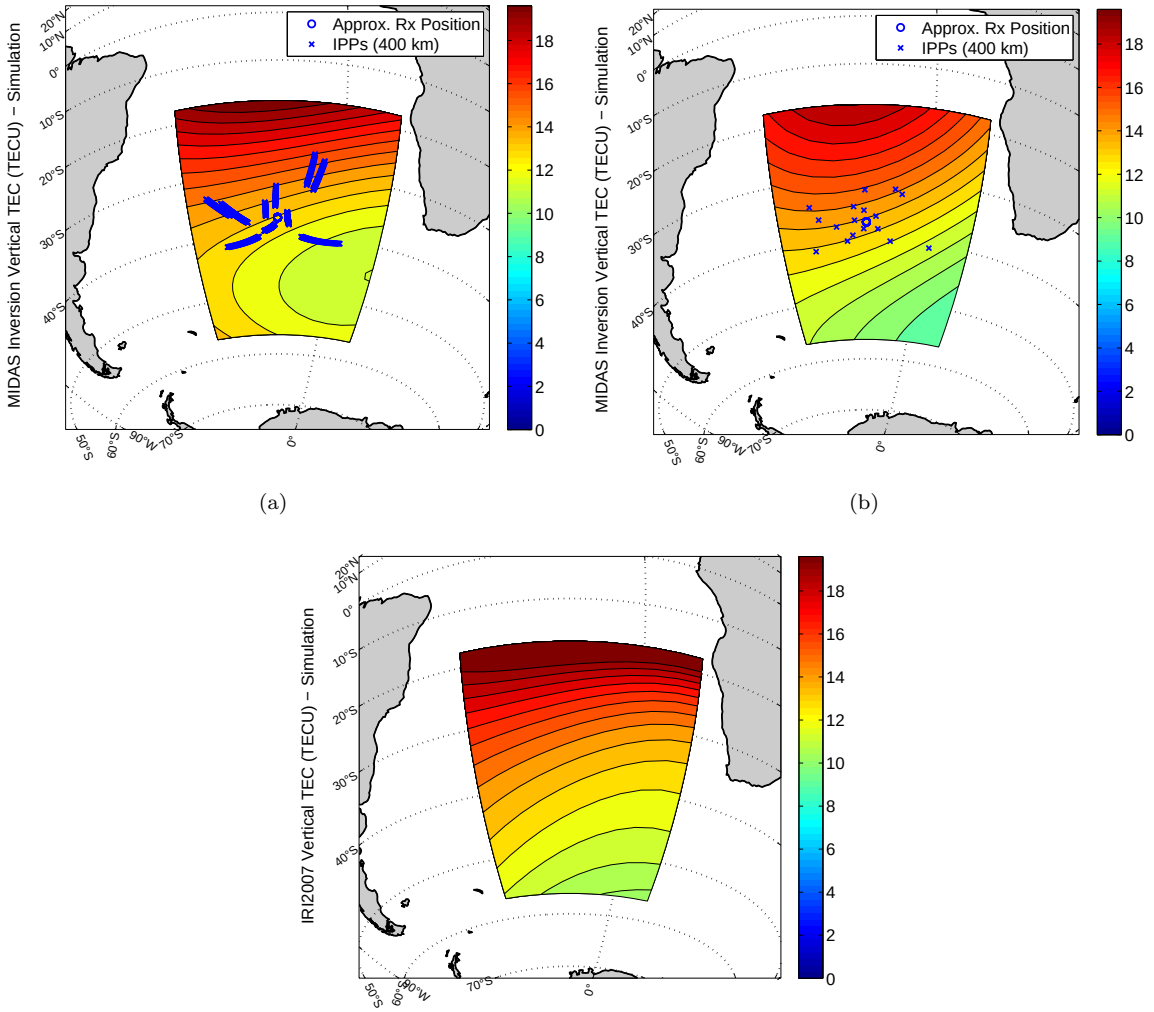

FIGURE 3.4: Comparison of VTEC maps: (a) Sampling rate of 30 seconds, (b) Sampling rate of 3600 seconds and (c) Model IRI2007 VTEC.

3.1.2 Determination of basis functions (EOFs)

The basis functions (also known as EOFs) used in the MIDAS inversion have a significant influence on the results of the inversion, as discussed in Chapter 2. There are three factors that play a major role in determining the EOFs: type of EOF (Chapman, Epstein etc.), the number of EOFs used and the external information incorporated into the calculation of the EOFs. In this dissertation, only one-dimensional EOFs will be used. The available 1-D EOFs in MIDAS are the Chapman and the Epstein models. To determine the optimal parameters for EOF generation, the electron density map obtained by inversion was compared to the known IRI2007 model for different values of several parameters.

3.1.2.1 Model-dependant basis function parameters

MIDAS needs two model-dependent parameters which are characteristic of both the 1-D models available (Chapman and Epstein), namely the peak height (h_mF2) and the bottomside scale height (H_mF2). The reader is referred to Section 2.2.4.1 for more information on these variables. The IRI2007 model will be used for the estimation of these parameters. The IRI model is the standard model of the ionosphere currently being used by the International Telegraphic Union (ITU). The IRI model can provide a electron density profile given the date, time, latitude, longitude and height of the profile in question.

To incorporate a priori information into the formation of these EOFs, the peak electron density N_mF, and peak height, h_mF2, obtained from the IRI2007 model were used as model-dependent parameters for the basis functions. The simulated receiver is located on route to Gough Island (37°S, 12°W). The IRI2007 vertical electron density profile at 12:30 UT for 2010-01-01 (same as the model IRI2007 ionosphere) at these coordinates is shown in Fig. 3.5.

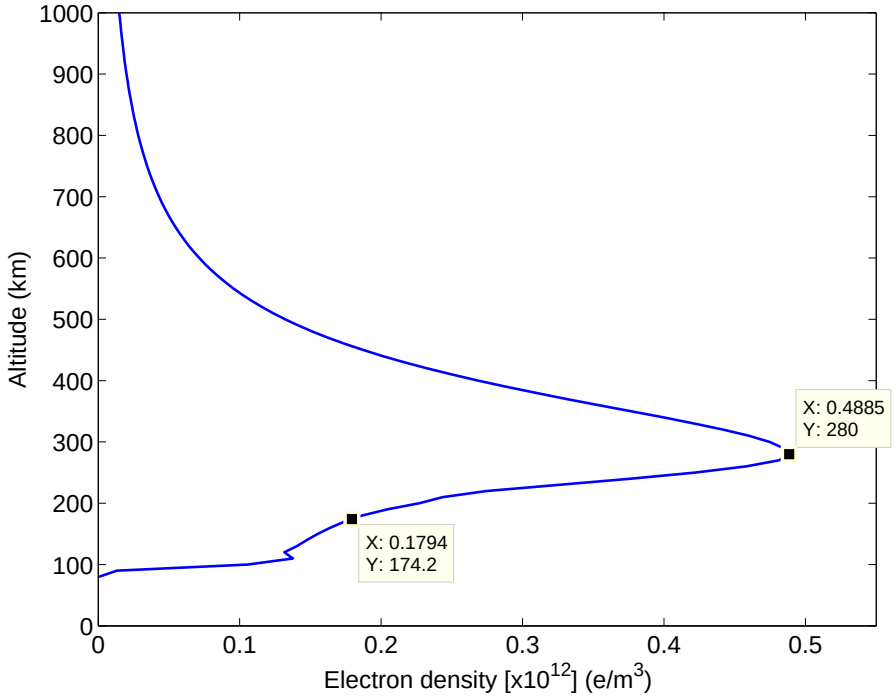

FIGURE 3.5: IRI2007 electron density at (-37,-12) [lat,lon] at 12:30 UT on 2010-01-01.

From the IRI2007 generated profile, N_mF2 was found to be 0.4885×10^{12} $\frac{e}{m^3}$, and the corresponding peak height, h_mF2 equal to 280 km. The electron density at the scale height could then be calculated according to the relation discussed in Section 2.2.4.1:

$$N_H = \frac{N_mF2}{e} \ ,$$

where $e = 2.718281$. N_H was found to be 0.179×10^{12} $\frac{e}{m^3}$. From the IRI2007 profile, the scale height was approximately 105.8 km (factor e reduction from 280 km to 174.2 km). The scale height was rounded off to 105 km. Thus, for the simulation, the following primary EOF model-dependent parameters were used:

- Peak height: 280 km, Scale height: 105 km.

3.1.2.2 IRI2007-based EOF generation

Regardless of how the model-dependent parameters are determined (explained in Section 3.1.2.1), the optimal model-independent parameters used for EOF generation need to be determined. Since simulations are performed using a known model, electron density maps can easily be compared for different values of the model-independent parameters. Three model-independent variables were changed in the EOF generation settings in order to determine their optimal values:

- Type of EOFs - CHAPMAN or EPSTEIN
- Number of EOFs used - 1,3,5,7
- Order of longitude (Mmax) and latitude (Nmax) harmonics - 16,12,8,4

The peak height and scale height of the primary profile above the simulated receiver's position was determined by the process explained in Section 3.1.2.1:

- Peak height: 280 km, Scale height: 105 km

To generate more EOFs, the procedure outlined in [24] was followed, where more EOFs are added either side of the primary EOF generated by the IRI2007 model:

- Three basis functions used

  - Peak height: 250 km, Scale height: 105 km
  - Peak height: 280 km, Scale height: 105 km
  - Peak height: 310 km, Scale height: 105 km

- Five basis functions used
  - Peak height: 250 km, Scale height: {95,105} km
  - Peak height: 280 km, Scale height: 105 km
  - Peak height: 310 km, Scale height: {105,115} km

- Seven basis functions used
  - Peak height: 250 km, Scale height: {95,105} km
  - Peak height: 280 km, Scale height: 95,105,115 km
  - Peak height: 310 km, Scale height: {105,115} km

Fig. 3.6 shows a plot of the EOFs generated if five Chapman model EOFs are used.

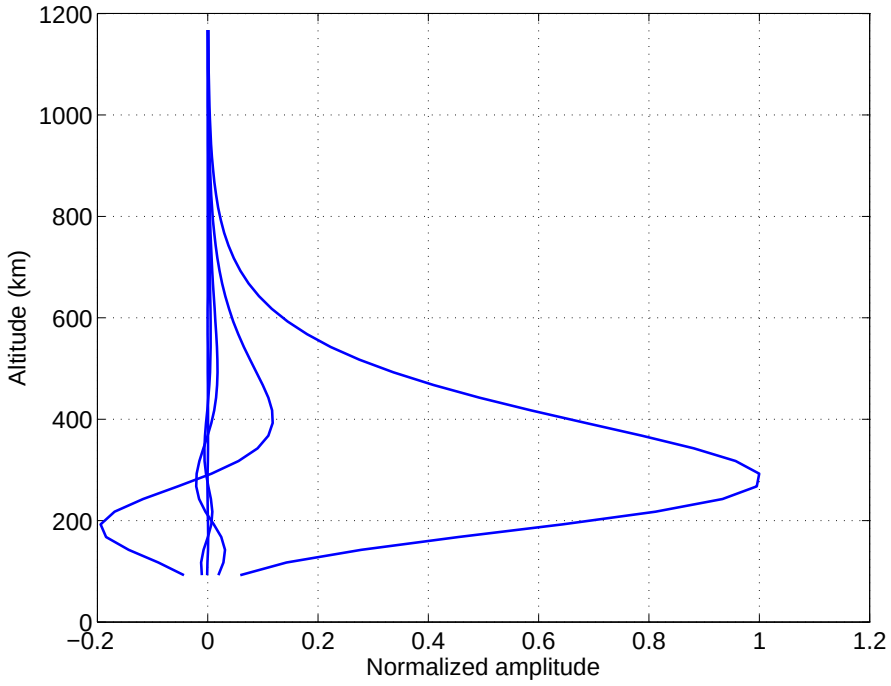

FIGURE 3.6: Five Chapman-based EOFs.

Initially, only an analysis based on the type and number of EOFs was performed for a fixed order of longitude (Mmax) and latitude (Nmax) harmonics (Nmax/Mmax = 8/8). Fig. 3.7 shows the VTEC maps using Epstein profiles, and Fig. 3.8 using Chapman profiles. In Fig. 3.7 differences are clearly visible, especially in absolute VTEC at low latitudes and in the change in VTEC at higher latitudes. However, there is no significant difference in rate of change in VTEC and Figs. 3.7(a)-(d) show a resemblance to the model VTEC in Fig. 3.7(e). For the sake of computational simplicity, one Epstein EOF provides the best performance.

Fig. 3.8 shows that, similar to the Epstein-based VTEC maps, there is no significant difference between the use of one Chapman EOF and seven Chapman EOFs. However, as in the Epstein case, more differences are visible in the VTEC rate of change at higher latitudes. The VTEC map with seven EOFs seems to have the best correlation to the model VTEC map at higher latitudes, but overestimates the peak VTEC at low latitudes. On the other hand, the use of one Chapman EOF provides a better correlation with the model ionosphere at low latitudes, but does not match the VTEC rate of change at higher latitudes. These differences are, however, minor and the author believes that the increased computational complexity for determining and calculating additional EOFs are unnecessary and that one EOF is adequate. Fig. 3.7 and Fig. 3.8 indicate that one Chapman EOF provides the best correlation to the model ionosphere - especially due to the lower rate of change at high latitudes. Thus one Chapman EOF was used to investigate the choice of the order of longitude (Mmax) and latitude (Nmax) harmonics.

The range of Nmax and Mmax considered was between 4 and 16. Fig. 3.9 shows a comparison of VTEC maps as a function of the order of longitude (Mmax) and latitude (Nmax) harmonics. It can be seen in Fig. 3.9 that if a higher order of harmonics (Nmax/Mmax) is used, additional higher frequency variations are introduced into the VTEC map. The purpose of the EOFs is to provide a basis on which the STEC values can be mapped. However, it seems that if a high order of longitude and latitude harmonics is used, the STEC values are dominated by variations in latitude and longitude. For this reason, the use of only one Chapman-based EOF with (Nmax/Mmax = 4/4) is considered optimal and will be used in this chapter.

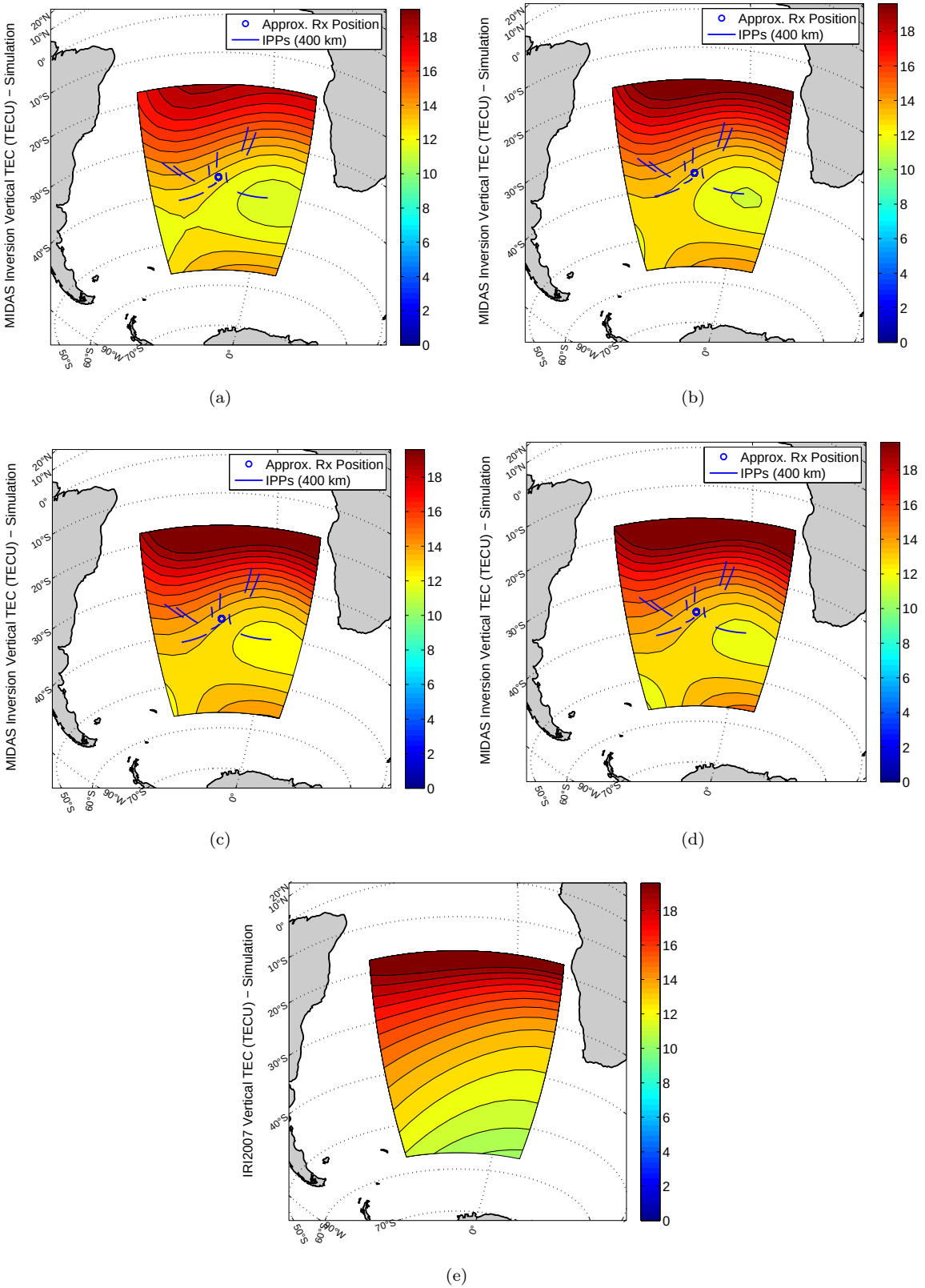

FIGURE 3.7: Comparison of VTEC maps using Epstein profiles: (a) One EOF, (b) Three EOFs, (c) Five EOFs (d) Seven EOFs, (e) Model IRI2007.

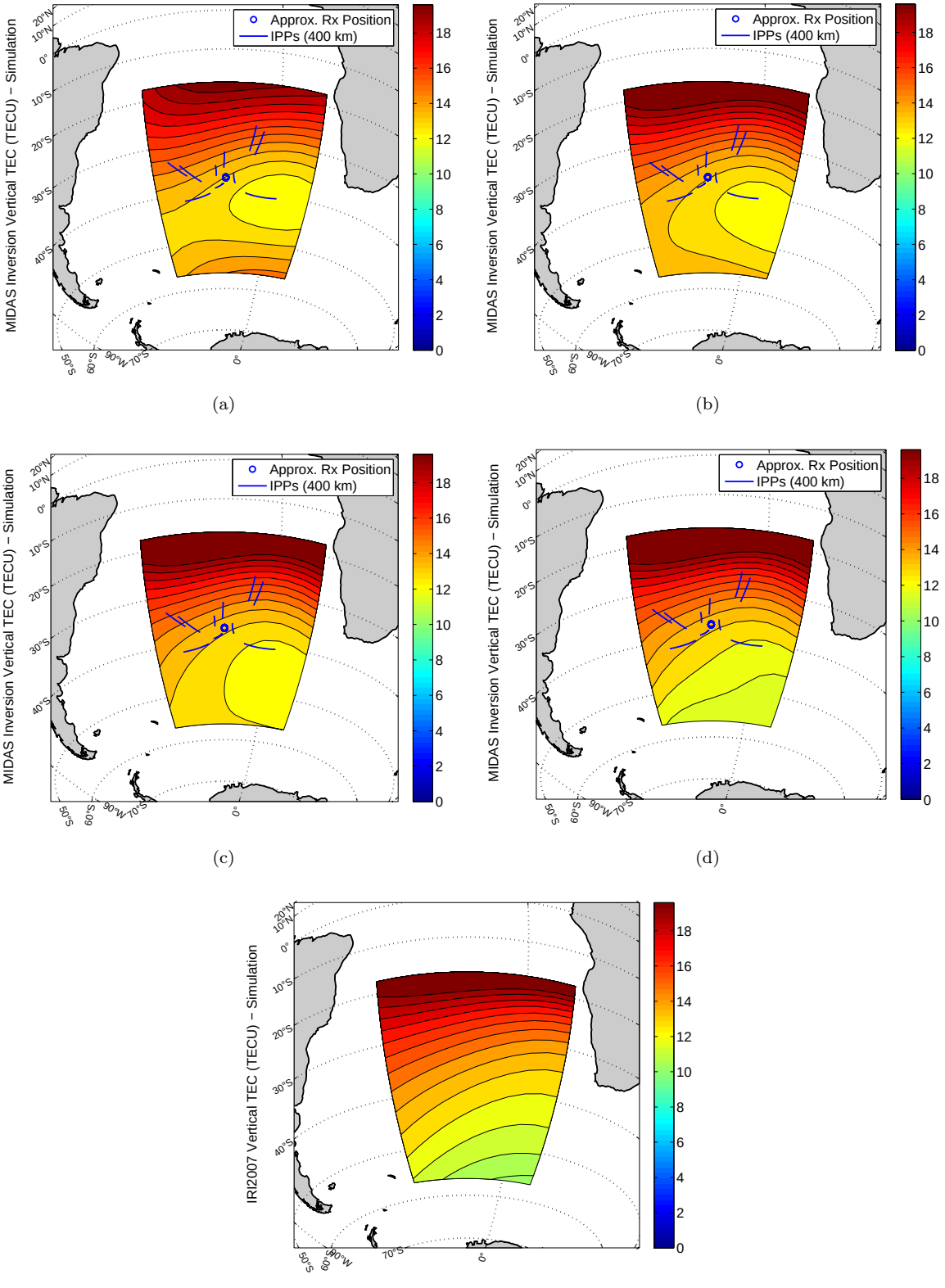

FIGURE 3.8: Comparison of VTEC maps using Chapman profiles: (a) One EOF, (b) Three EOFs, (c) Five EOFs (d) Seven EOFs, (e) Model IRI2007.

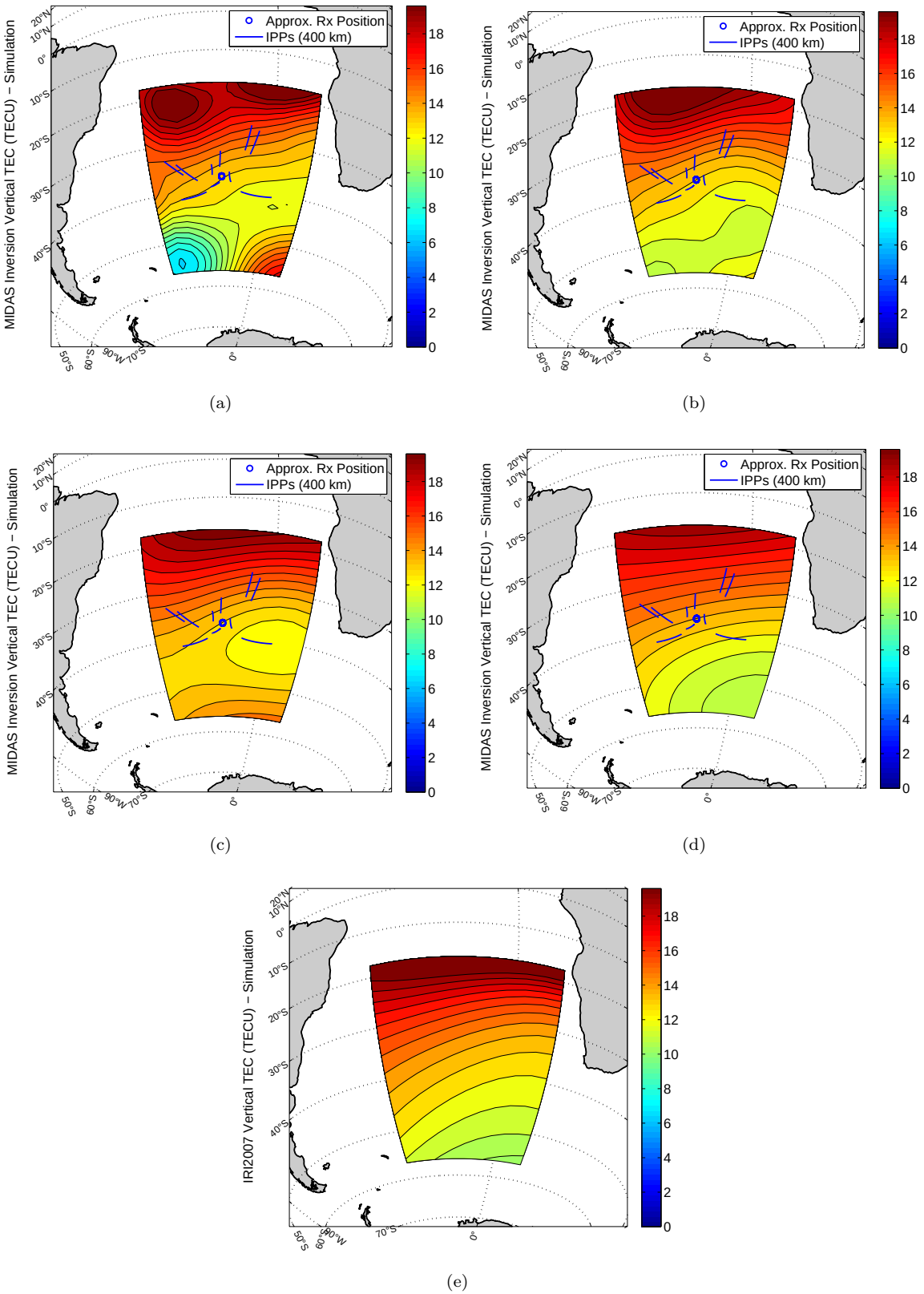

FIGURE 3.9: Comparison of VTEC maps as a function of longitude (Mmax) and latitude (Nmax) harmonics: (a) Chapman (Nmax/Mmax = 16/16), (b) Chapman (Nmax/Mmax = 12/12), (c) Chapman (Nmax/Mmax = 8/8), (d) Chapman (Nmax/Mmax = 4/4), and (e) Model IRI2007.

The differences between the electron density map generated with the MIDAS inversion and the map of the actual electron density of the ionosphere play a very important role in the MIDAS bias estimation, as discussed in Section 2.2.4.3. An analysis on EOF generation with bias estimation is performed in Chapter 4.

3.1.3 MIDAS inversion settings

Table 3.1 shows the MIDAS inversion settings common to all inversions in Chapter 3. All unique parameters used are specified at each inversion.

TABLE 3.1: MIDAS inversion settings common to all inversions.

MIDAS Inversion Settings	
Number of EOFs	1
Type of EOF	Chapman
Nmax/Mmax	4/4
280 km (IRI2007)	105 km (IRI2007)

3.2 RESULTS

The influence of the following factors on the accuracy of the inversion process were simulated:

- Static versus mobile receiver performance
- Sampling interval and performance
- Receiver speed and performance

The performance evaluation was done in accordance with the performance analysis method discussed in Section 3.1.1.

3.2.1 Static and mobile receiver performance

The performances of a simulated static receiver and a simulated mobile receiver were compared. To simulate the movement of the SA Agulhas research vessel, the simulated mobile receiver moved at a speed of 10 knots (18.52 km/h), which is the approximate speed of the SA Agulhas under normal ocean conditions. Fig. 3.10 shows the VTEC maps for a static and for a moving receiver, as well as the model ionosphere.

Discussion and conclusion

Fig. 3.10 shows no significant difference in VTEC between a static and a mobile receiver moving at 18.52 km/h. There is a slight and insignificant difference at higher latitudes. The results suggest that there is a very small difference between electron density maps generated from using observables from mobile and static GPS receivers. This may be true for magnetically quiet conditions, but the author believes that during magnetic storms, the high variation in the ionosphere may be better modelled by a mobile receiver because of the slight increase in resolution, as explained in Section 2.4.1.

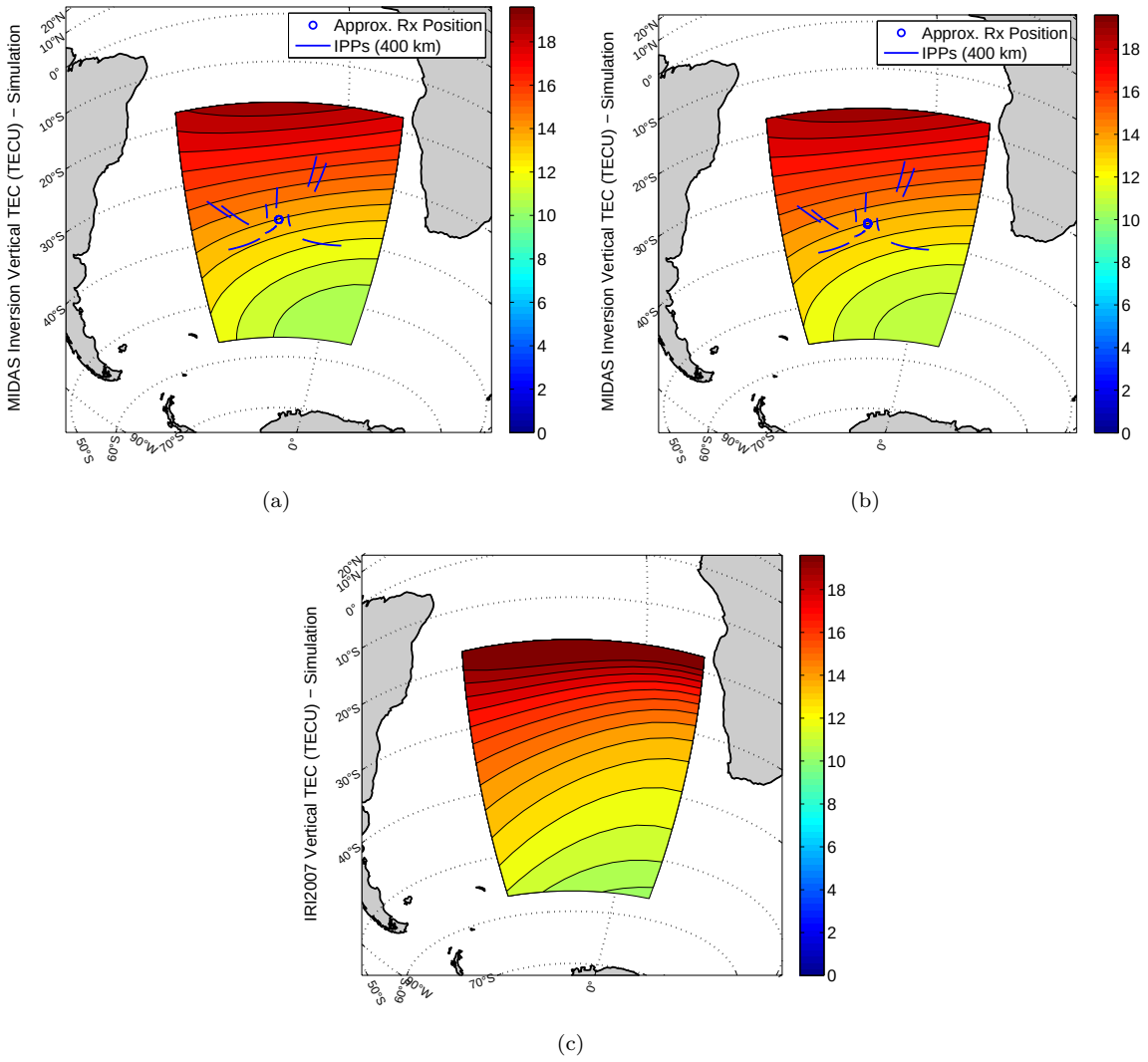

FIGURE 3.10: VTEC maps based on the use of a static and a mobile GPS receiver: (a) Static GPS receiver, (b) Mobile GPS receiver, (c) Model IRI2007.

3.2.2 Sampling interval and performance

To analyse the trade-off between sampling interval and performance specific to a mobile GPS receiver, the sampling interval was simulated for the following range of values:

$$T_s = [30\ 300\ 1800\ 3600] \text{ seconds.}$$

Fig. 3.11 shows VTEC maps for different values of the sampling interval, as well as the model ionosphere.

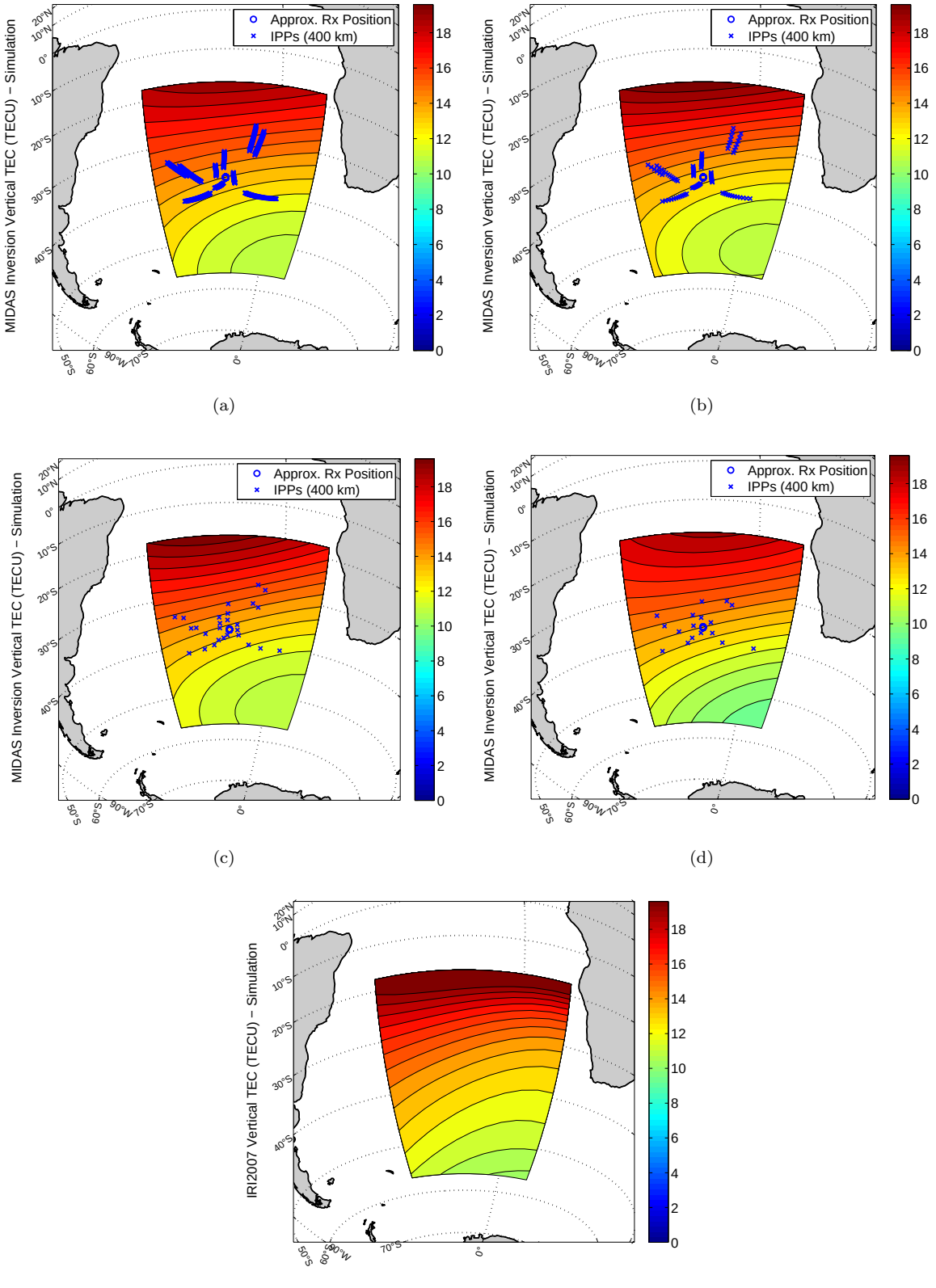

FIGURE 3.11: VTEC maps as a function of sampling rate: (a) $T_s = 30\ s$ (1071 STEC values), (b) $T_s = 300\ s$ (104 STEC values), (c) $T_s = 1800\ s$ (27 STEC values), (d) $T_s = 3600\ s$ (17 STEC values) and (e) Model IRI2007.

Discussion and conclusion

Fig. 3.11 shows slight differences in VTEC for different sampling rates. The ionospheric pierce points on Fig. 3.11 are indicated with crosses to show the exact point of penetration at a height of 400 km. A slight and insignificant difference is observed at approximately 50° latitude and higher VTEC can be seen at 20° latitude for a sampling rate of 300 and 1800 seconds. However, these differences fall outside the ray paths providing STEC values to the MIDAS package and the VTEC maps are expected to differ slightly. The results suggest that there are very small differences between electron density maps based on observables using 30 to 3600 second sampling intervals. However, this holds true for a simulated case with the assumption that all satellites are visible. In Fig. 3.11(d) it can be seen that even for a very low sampling rate of 3600 seconds, there are still seventeen STEC values available for use by the MIDAS package that completely characterise the rate of electron density change in the area around the receiver. In magnetically quiet conditions, seventeen STEC values would most probably provide adequate information for determining the rate of change in electron density. When using actual GPS receivers, all satellites are not always visible and all GPS observables are not always available, with the result that the rate of change in electron density of the ionosphere may not be completely characterised around the receiver, as will be shown in Chapter 4. During magnetic storms, greater variation in electron density can be expected. Therefore, the sampling rate must be higher to obtain a resolution capable of characterising areas with a high rate of change. It is the opinion of the author that the results presented here do not give a definite indication of the optimal sampling rate to be used and that the lowest sampling rate attainable must be used, taking into account storage and processing power limitations. If a higher sampling rate is used, more observables are available and more accurate electron density maps can be produced which take into account data quality and satellite visibility factors. These aspects will be addressed in Chapter 4.

3.2.3 Receiver speed and performance

For an analysis of the effect of the receiver speed on the accuracy of the inversion, the performance of the following range of speeds was considered:

$$Speed = [5\ 15\ 25\ 35\ 45]\ \text{knots} = [9.26\ 27.78\ 46.3\ 64.82\ 83.34]\ \frac{\text{km}}{\text{h}}$$

Since the current study is based on a GPS receiver installed on a research vessel, typical ship speeds were chosen - 5 knots for an Antarctic research ship in stormy conditions and 45 knots for the speed of a military vessel. Fig. 3.12 shows VTEC maps for different simulated speeds of the mobile receiver, as well as the model ionosphere.

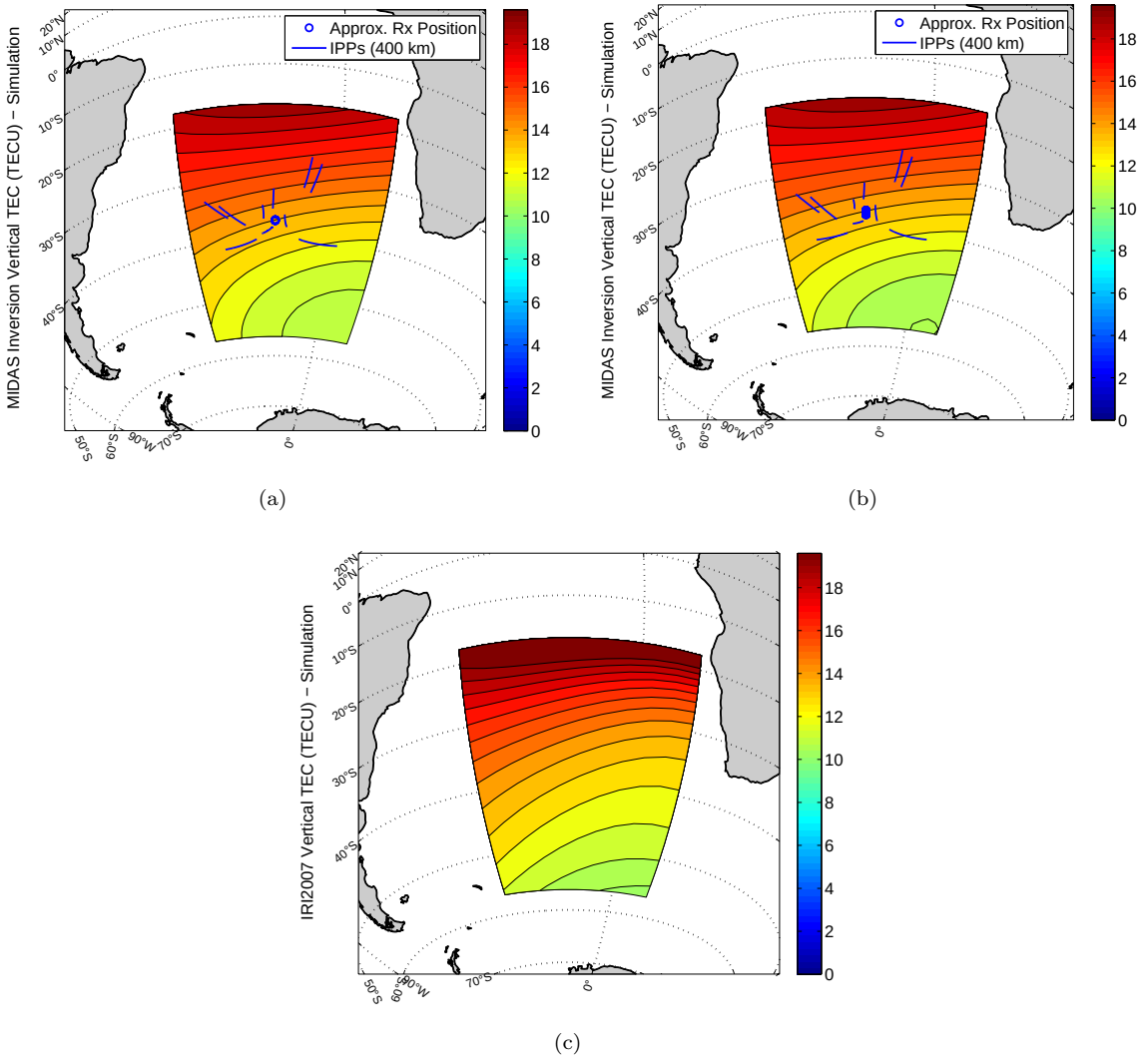

FIGURE 3.12: VTEC maps as a function of simulated GPS receiver speed: (a) Speed = 5 knots, (b) Speed = 45 knots and (c) Model IRI2007.

Discussion and conclusion

The VTEC maps for 15, 25 and 35 knots are not shown in Fig. 3.12, because there are no significant changes in VTEC between 5 knots and 45 knots. As discussed in Section 3.2.2, the author believes that an increase in speed would produce a higher resolution.

However, a higher resolution can also be obtained by increasing the sampling rate and then the GPS receiver speed becomes insignificant.

3.3 CONCLUSION

In this chapter a model ionosphere was generated using the IRI2007 model and a simulated GPS receiver was used to obtain sampled STEC values from the model ionosphere. The MIDAS package was used to calculate electron density maps using these STEC values and the accuracy of the inversion was investigated for several parameters. The construction of appropriate EOFs was discussed and several optimal parameters for the simulation were determined. Comparisons of vertical total electron content maps were made as a function of the mobility or not of the GPS receiver, sampling rate of GPS observables and GPS receiver speed. No significant differences between VTEC maps were found for all three analyses. However, the author believes that if a higher resolution map of the ionosphere is needed, a mobile GPS receiver moving faster with a higher sampling rate would provide more accurate results. These factors would also play a more prominent role if a real GPS receiver were used, because satellite visibility and data quality are not perfect, as it were with a simulated ionosphere and GPS receiver. Experimental work with GPS observables from a dual-frequency GPS receiver on a research vessel is presented in Chapter 4.

CHAPTER 4

EXPERIMENTAL VERIFICATION

In this chapter the results of experimental work are presented and verified by means of various analyses which includes a comparison with ionosondes, static land-based GPS receivers and HF propagation path algorithms. It is assumed that the reader has studied Chapter 2 and 3 and understands the basic concepts behind GPS tomography.

In order to draw a conclusion on the the viability of using a single dual-frequency GPS receiver on a ship for ionospheric tomography and the eventual viability of implementing a mobile GPS dual-frequency receiver network, all aspects of the tomographic process have to be considered. These include the collection of GPS observables, their preprocessing and the generation of electron density maps from the observables. GPS data preprocessing to the point where the data can be used for the inversion, requires steps such as quality checking, format conversions and optimization, just to mention a few. All data pre-processing was performed with the mobile GPS toolbox developed in MATLAB by the author. The quality of the observables obtained from the mobile GPS receiver installed on the SA Agulhas and the processing thereof are discussed in Section 4.1.

To verify the electron density maps generated from the GPS observables measured by the SA Agulhas GPS receiver, the results were compared to electron density profiles generated by the ionosonde at the Hermanus Magnetic Observatory (HMO) at a time when the SA Agulhas was close to Hermanus, South Africa (see Section 4.3).

The results were also compared to electron density maps generated from observables measured by static land-based GPS receivers at a time when the SA Agulhas was near the static receivers at Cape Town and Gough Island. These results are presented in Section 4.4. Further verification was done by comparing the HF path predictions using the IRI2007 model and the maps obtained by the mobile GPS receiver to known HF propagation paths (see Section 4.5).

4.1 DATA QUALITY

Data quality refers to the measure of suitability of data for its intended purpose or use. In the case of ionospheric tomography, data quality refers to the suitability of the GPS receiver observables for successful use throughout the tomographic inversion process. The simulations performed in Chapter 3, prove with a fair amount of certainty that ionospheric tomography using a mobile GPS receiver can produce useful results, given that the observables are perfect, such as those used in the simulation. Unfortunately, GPS observables acquired from actual dual-frequency GPS receivers are not perfect and may be influenced by factors beyond human control. What follows is a discussion of data quality criteria and preprocessing, and the external factors that possibly influence the quality of GPS observables.

4.1.1 Data quality control parameters and preprocessing

Variables contained in satellite observations

As discussed in Chapter 2, certain variables are needed to calculate total electron content from raw GPS observables. These variables include $L1$, $L2$, $P1$ and $P2$. If the $P1$ observable is not available, the course acquisition (C/A) code $C1$ can be used instead of $P1$ for calculating P_I, and from the mean of P_I the offset required for levelling L_I. The raw satellite observation data can be filtered to check whether all the required variables are available for at least a fraction of the period of interest. If the satellite observation data contains the complete set of L and P variables, tomography can be performed. If not, the observables originating from this satellite cannot be used in the MIDAS inversion. In the mobile GPS toolbox, a minimum number of satellite with complete observation sets per time period can be specified. If the number of satellites with complete observation sets is less than this specification for a specified

time period, the observable set is flagged as inadequate for the generation of accurate electron density maps and no maps are generated for this period. The user specifies the *number of valid satellite observations per time period*, and the observables are scanned accordingly. However, a satellite may be flagged as not containing the complete set of variables for the specified period, but may still contain valid epochs. This is discussed in *total number of ray paths*. Satellites with a complete set of L and P (or C/A) variables, will henceforth also be referred to as valid satellites.

Ray path elevation angle threshold

Multipath is a phenomenon where signals from the satellite are reflected off a reflective surface and are added to the signals received on a direct path from the transmitter. This is a common problem especially on the oceans - the surface of the ocean is one continuous reflective body and the upper structure of the ship provides many reflective surfaces above the level of the GPS antenna. Due to multipath, signals may even seem to be originating from under the horizon. The vessel is a metal structure and many structures on the ship act as a reflective surface, especially since the GPS antenna is not installed above all the metal objects on the ship. For instance, the smokestack rises above the GPS antenna. The location of the smokestack relative to the GPS antenna can be seen in Fig. 4.1. In an attempt to reduce this effect, an elevation angle cutoff was introduced. The elevation angle is the angle above the horizon from where the signal seems to be originating. Any signals received from below this cutoff angle are removed from the slant TEC data set. Ideally, only ray paths originating from above all structures surrounding the GPS antenna should be used. However, making the elevation angle cutoff too high could lead to the loss of useful information. The trade-off involved when choosing the elevation angle for the SA Agulhas GPS receiver, is illustrated in Figs. 4.2 and 4.3. Fig. 4.2 shows the ionospheric pierce points (IPP's) as a function of azimuth and elevation for the land-based SUTH (Sutherland) GPS receiver (32.38°S, 20.81°E) on 2005-11-05. GPS data from the Cape Town receiver was not available on this day. Sutherland was the closest land-based receiver with 24 hours of data on 2005-11-05. All IPP's are clearly visible for all elevation and azimuth values except for $250° - 300°$, which is caused by the 55° inclination of the orbital path of the GPS satellites. Fig. 4.3 shows the ionospheric pierce points as a function of azimuth and elevation for the AGHL (SA Agulhas) GPS receiver on 2005-11-05. Here an additional "hole" (indicated by a red oval) can clearly be seen in the IPP's between $250° - 300°$ azimuth and $0° - 30°$ elevation. Since the SA Agulhas was anchored in

the Cape Town harbour on this day, it was easy to determine that this hole in GPS visibility was caused by the smoke stack of the vessel. Based on Fig. 4.3 the elevation angle threshold should be set at 30° to eliminate the possible multipath effects of the smoke stack. However, many observations which seem valid (following the satellite orbit) would be lost - such as the observations under an elevation of 30° for an azimuth of $0° - 150°$. Considering the trade-off between losing GPS observables and reducing the effects of possible multipath, an elevation angle of 20° was chosen.

FIGURE 4.1: The position of the GPS antenna relative to the smokestack on the SA Agulhas vessel - with permission from [4].

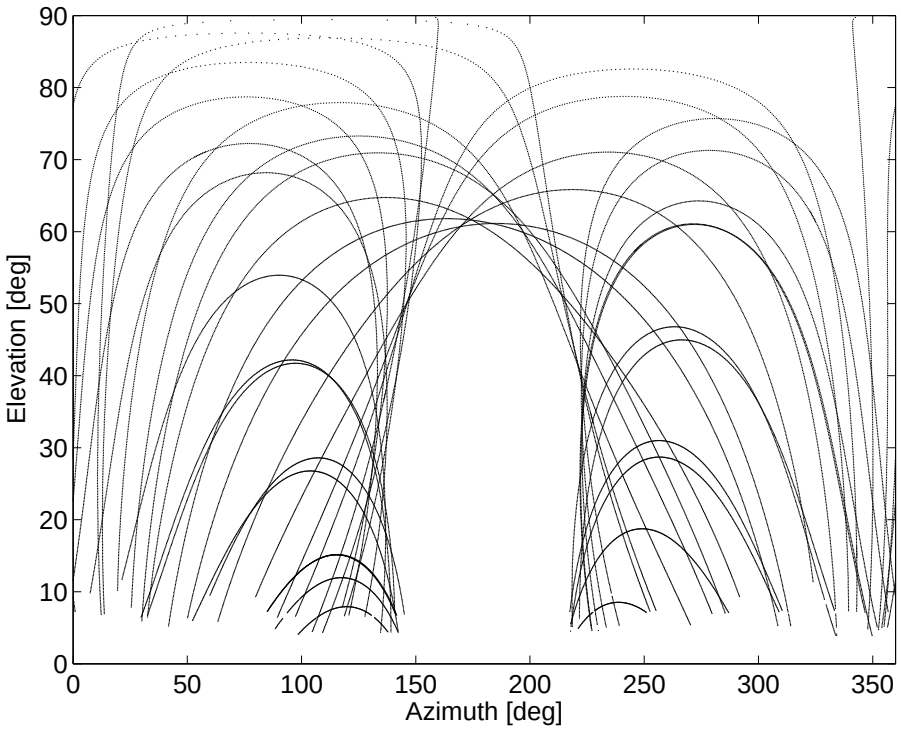

FIGURE 4.2: Ionospheric pierce points as a function of azimuth and elevation for the SUTH (Sutherland) GPS receiver on 2005-11-05.

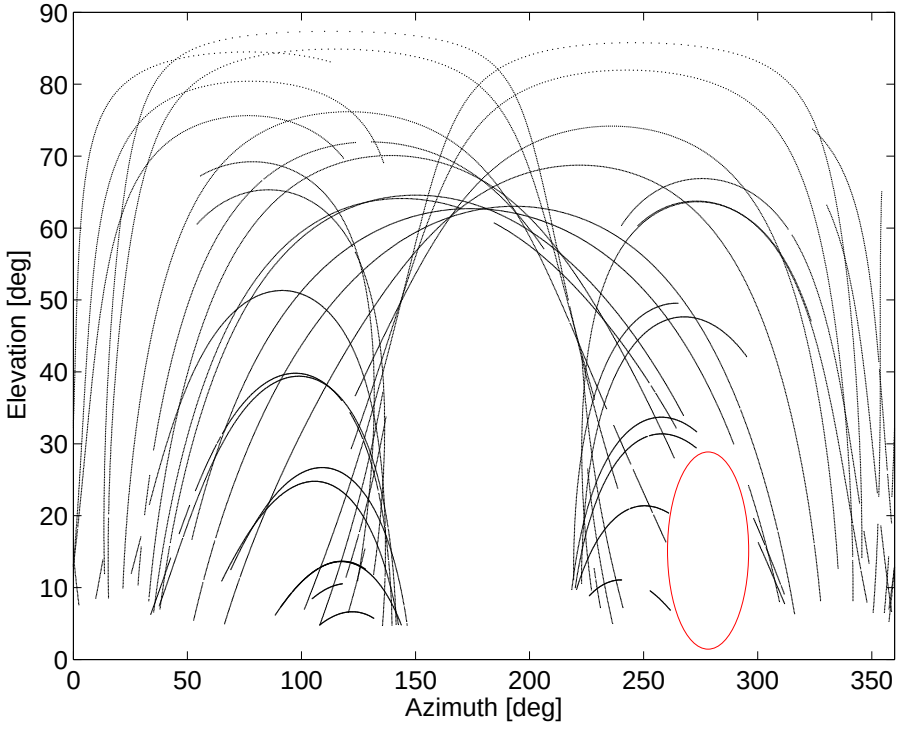

FIGURE 4.3: Ionospheric pierce points as a function of azimuth and elevation for the AGHL GPS receiver on 2005-11-05. The red oval indicates the loss of satellite visibility due to the smoke stack on the SA Agulhas.

Total number of ray paths

Filtering satellites to those which produce a complete observation is only one step in the filtering process, and this does not guarantee a large number of valid GPS observables. To illustrate, consider the MIDAS inversion process. The built-in filter for observables of the MIDAS algorithm only uses slant TEC values which form part of at least six contiguous observations without any interruptions - for a sampling interval of 30 seconds this is equal to three minutes. However, suppose slant TEC values for the time period 01:00 - 02:00 from the SA Agulhas GPS receiver observables can be generated. For this period, there may be 8 satellites with complete observables. However, these observables may only have been recorded during the period 01:00 - 01:10, after which the receiver was switched off. Since the 10 minute interval is larger than the minimum value for the MIDAS filtering, the slant TEC values would be used. This would give the impression that the data is adequate, but in actual fact the observables cover a very limited period of observation and in effect a very limited geographical area. To avoid this scenario, the GPS raw observable data is also filtered according to total epochs observed (total slant TEC observations per period) before inversion is performed. The criteria state that, for observables from a given period to be acceptable for inversion, all the visible satellites must have all the required observables for at least a specified period. The formula for deriving the minimum number of epochs is:

$$Epochs_{min} = x(F_t) \ , \tag{4.1}$$

where x is the number of ray paths an ideal receiver would have had - for instance, with a sampling interval of 30 s and a period of one hour, the receiver should have 120 observations per visible satellite. F_t is the minimum fraction of the ideal number of ray paths. The slant TEC data set must have at least $Epochs_{min}$ valid slant TEC values to be used for the inversion. If not, the GPS observable data set for the period is flagged as inadequate for the generation of accurate electron density maps.

Cycle slips

Fig. 4.4 shows a comparison between slant TEC (LTEC) values for specific satellites recorded by the GPS receiver on the SA Agulhas (AGHL) and the land-based Cape Town GPS receiver (CTWN, 33.95°S, 18.47°E) for the time period between 05:00 - 06:00 UT on 2010-05-20 (day of year 140) after bias correction. The SA Agulhas was close to the Cape Town receiver during this period and ideally, the slant TEC for each satellite should be the same, whether observed from the SA Agulhas or from the

land-based receiver. In Fig. 4.4 the slant TEC values clearly follow the same trend. However, a TEC jump is visible in the SA Agulhas data around epoch 70 for satellite PRN0019.

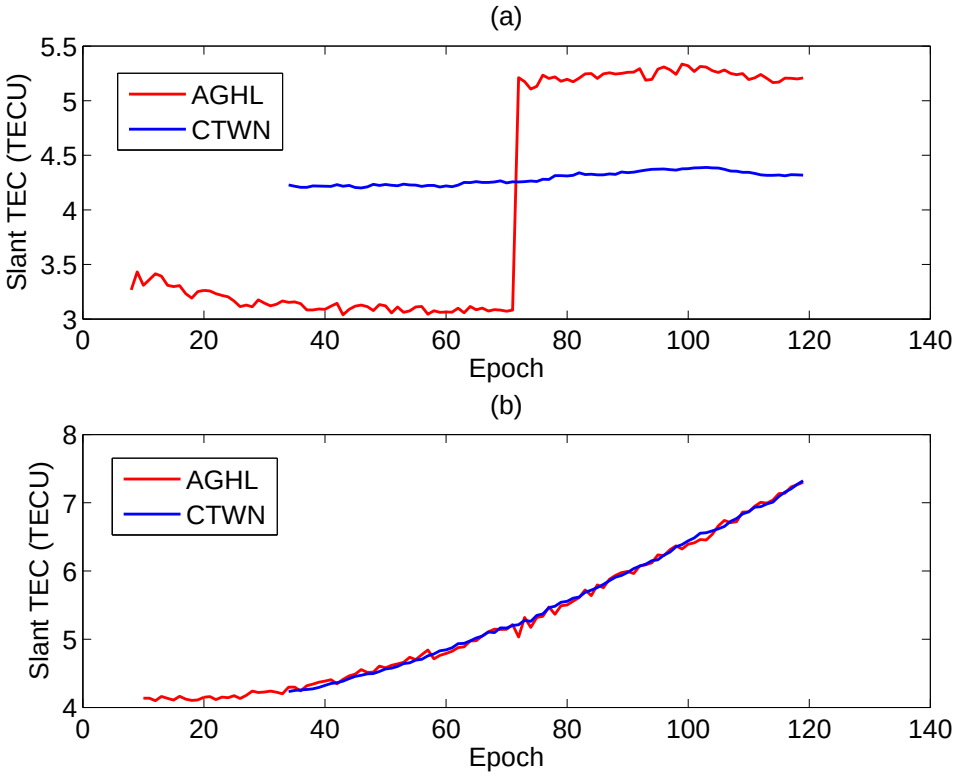

FIGURE 4.4: Slant TEC comparison (without cycle slip correction) of the SA Agulhas (AGHL) and Cape Town (CTWN) GPS receivers for the time period 05:00 - 06:00 UT on 2010-05-20 (day of year 140): (a) Satellite PRN0019. (b) Satellite PRN0023.

The TEC jumps in the slant TEC values may have a significant effect on the inversion results since the TEC level is shifted (in the case of PRN0019) by about 2 TECU. These TEC jumps are caused by cycle slips. At GPS signal lock, an integer number is arbitrarily assigned to the cycles measured by the L observables. When an interruption of signal occurs, this integer number has to be re-assigned and the result is that the adjacent carrier phase observable may jump by an integer number of cycles [3]. The result is a jump in the LTEC. To correct for cycle slips, LTEC observations are filtered before levelling (refer to Section 2.2.2.1) and any variation of the LTEC value larger than a specified threshold value, is flagged as a cycle slip and a level correction is made. The value of this threshold was set at 1.5 TECU by a process of trial and error in an effort to find an optimal value. This agrees with the cycle slip definition defined as 1.5 TECU used in the literature [25]. This correction is shown in Fig. 4.5. Levelling to

the PTEC, as explained in Chapter 2, is done after the cycle slip correction has been made. For more information on cycle slips, the reader is referred to [3].

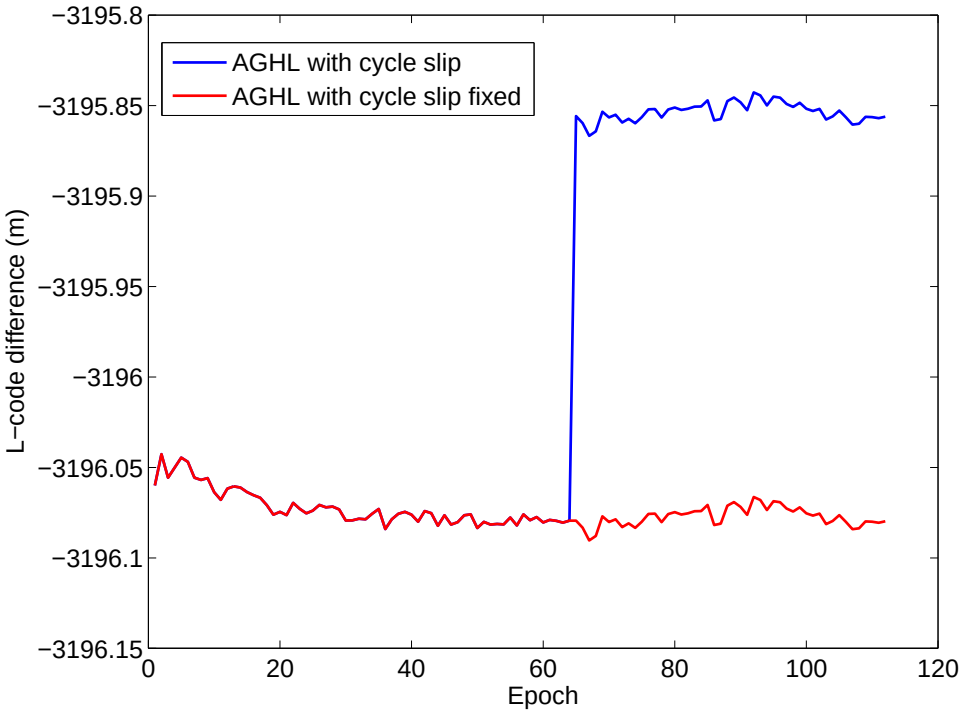

FIGURE 4.5: AGHL cycle slip correction on the L observable measured carrier phase range difference (m) (with a threshold equivalent of 1.5 TECU) for satellite PRN0019 between 05:00 - 06:00 UT on 2010-05-20 (day of year 140). Up to the cycle slip, both lines are exactly the same.

Data variation

Besides the jump in LTEC caused by cycle slip, there is a high epoch-per-epoch variation in slant TEC values in the AGHL observations in Fig. 4.4. Due to the sensitivity of the inversion process (caused by the sparseness of slant TEC values), large variations can cause the algorithm to reach a solution which differs from the actual electron density. To extract the electron density map, only the trend of the STEC values is needed. Thus, the high frequency variations in the STEC can be removed. To smooth the STEC, the moving average smoothing method was used. In this method, each value is determined from an average of a number of STEC samples taken before and after the sample. The output y at epoch n is given by (4.2):

$$y(n) = \frac{\sum_{k=\frac{-w}{2}}^{\frac{w}{2}} (s(n+k))}{w}\ , \tag{4.2}$$

where w represents the window width of the data samples used, y the output and s the input STEC. Smoothed values for STEC values within $\frac{w}{2}$ samples of the outer limits of the data set are obtained by shifting the summation in order to still use w samples for the smoothing. Fig. 4.6 shows an example of STEC from the SA Agulhas GPS receiver smoothed with a sample window of 6 samples.

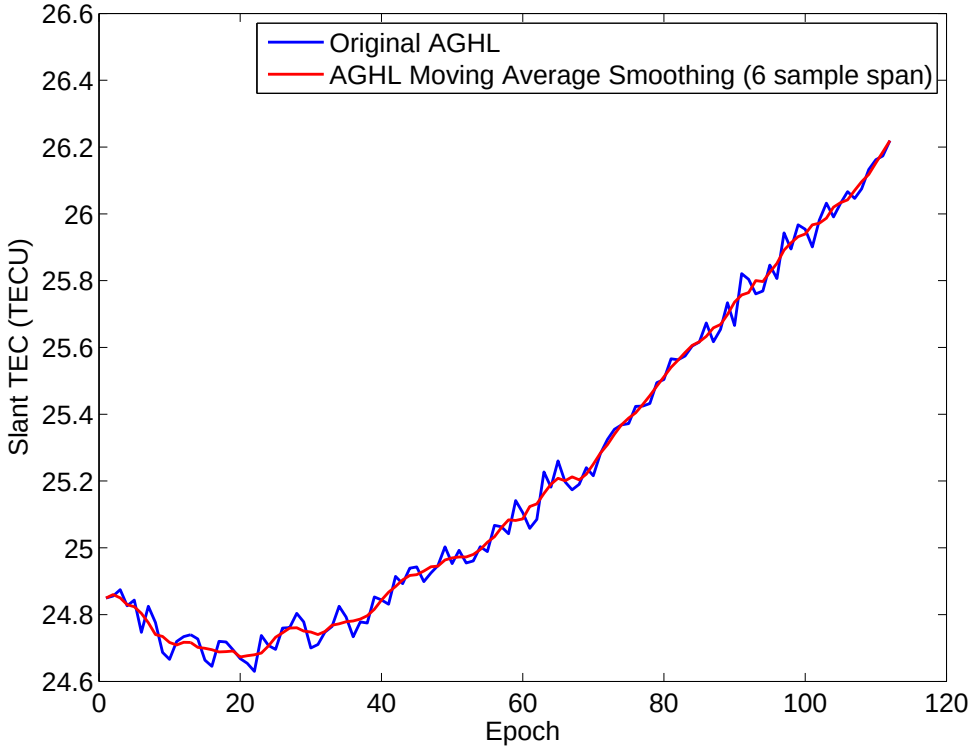

FIGURE 4.6: Slant TEC data smoothing using moving averaging with a sample width of 6 samples - equivalent to 3 minutes of data with a sampling interval of 30 s.

In Fig. 4.6 the trend of the STEC is intact. Using this method stabilizes the data input without any loss of important information regarding the distribution of the electrons.

4.1.2 External factors influencing data quality

The only prominent difference between the GPS receiver installed on the SA Agulhas and any other land-based GPS receiver is the fact that the SA Agulhas is constantly moving. For this reason, it is reasonable to suspect that differences in the quality of GPS observables from the SA Agulhas GPS receiver and land-based receivers, such as CTWN, are caused by the movement of the antenna and receiver. The movement of the GPS antenna on the SA Agulhas is directly proportional to the movement of the ocean surface. The oscillatory movement of the ship extends into three axis directions

and may introduce phase errors. Although GPS position accuracy is subject to some ambiguity, oscillatory movement of the ship increases the rate of change of the position. The movement may also promote multipath errors - the vessel is made of reflective material and the movement may have an erratic influence on signal propagation. A correlation analysis of the quality of data and the state of the ocean surface in order to quantify the influence of the state of the ocean surface on the usability of the GPS observables is presented in Section 4.1.3.

4.1.3 Correlation between the number of valid observation and the state of the ocean surface

4.1.3.1 Method and results

To determine whether there is a correlation between the quality of the data (in terms of the number of satellites with complete observable sets, also referred to as valid satellites, as discussed in Section 4.1.1) and the state of the ocean surface, a correlation analysis of these two variables was performed.

The Intergovernmental Oceanographic Commission of UNESCO (IOC) Sea Level Station Monitoring Facility project developed via a collaboration between the Flanders Marine Institute (VLIZ) and the Ocean Data and Information Network for Africa (ODINAFRICA) project of the International Oceanographic Data and Information Exchange (IODE). Initially it was focussed on monitoring sea levels around Africa. However, it later expanded to a global monitoring service. These stations sample the ocean level every minute providing tidal variations as well as wave height variation. The wave height variation can be used to gauge the level of turbulence of the ocean surface. One of the monitoring stations is located on Marion Island, the South African research island which is visited by the SA Agulhas research vessel at least once per year. The sea level monitoring station on Marion Island is shown in Fig. 4.7.

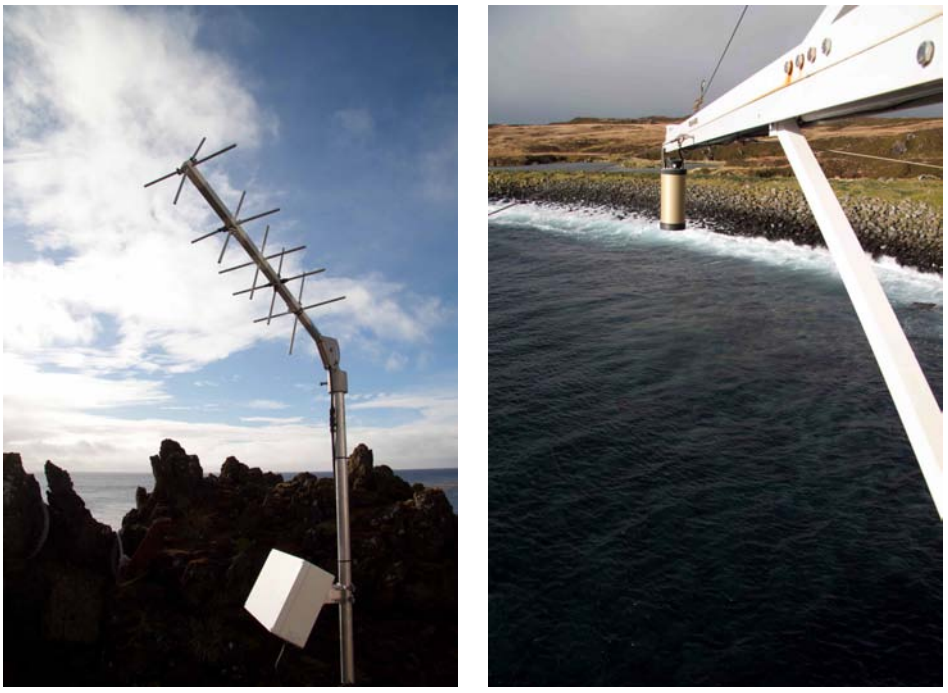

(a) (b)

FIGURE 4.7: Experimental setup of the IOC sea level monitoring station on Marion Island: (a) The antenna for data transmission, (b) The sea level sensor.

To correlate the number of valid satellites with the turbulence of the ocean surface, a period was chosen when the SA Agulhas was close to Marion Island. The vessel usually remains within a few kilometres from Marion Island during periods when a replacement overwintering team is dropped off and the team returning to South Africa embarks. In 2010 the ship visited Marion Island several times to transport staff members involved in the construction of the new base. It can be expected that the relative variation in data from the sea level monitor and the variation of the waves experienced by the vessel should be similar. A period of twenty five days was chosen for the analysis - 2010-04-16 (day of year 106) until 2010-05-10 (day of year 130). A correlation analysis was performed of the two variables for this period of 25 days. Fig. 4.8 shows the position of the SA Agulhas during this period.

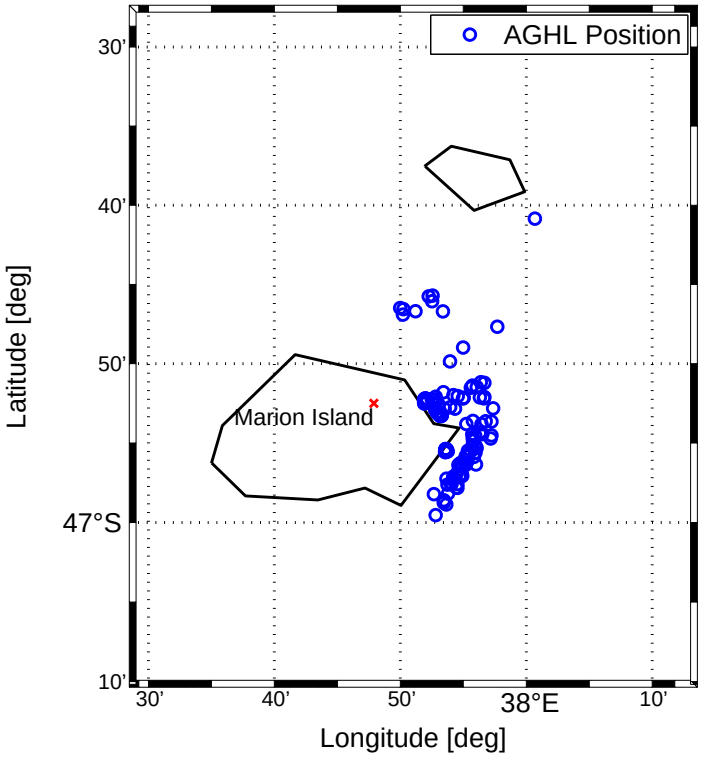

FIGURE 4.8: Positions of the SA Agulhas research vessel from 2010-04-16 (day of year 106) until 2010-05-10 (day of year 130).

Fig. 4.9(a) shows the wave height variation data (in meters) at Marion Island for the period of twenty five days. The sinusoidal component represents the tidal variation and the variation from this sinusoidal-like behaviour represents the turbulence of the ocean surface. Fig. 4.9(b) shows a sample of the data for the period 2010-06-06 to 2010-06-08 when a storm was brewing. The ocean surface seems to indicate a high variation around the sinusoidal tidal variation. Fig. 4.10 shows a sample of the number of valid satellites for 2010-06-06 (day of year 126) to 2010-06-08 (day of year 128), corresponding to the storm period in Fig. 4.9. To determine whether there is a correlation between the number of valid satellites and the sea turbulence for the period of 25 days, the sinusoidal variation of the sea level observations had to be removed to separate the surface movement from the tidal variation. The tidal variation however, is not clearly defined and cannot easily be calculated, as shown in Fig. 4.9. The MATLAB curve fitting function was used to estimate the tidal variation. The Smoothing Spline Method was used and the residuals (difference between the data and the fit) were used as data for the variation in wave height.

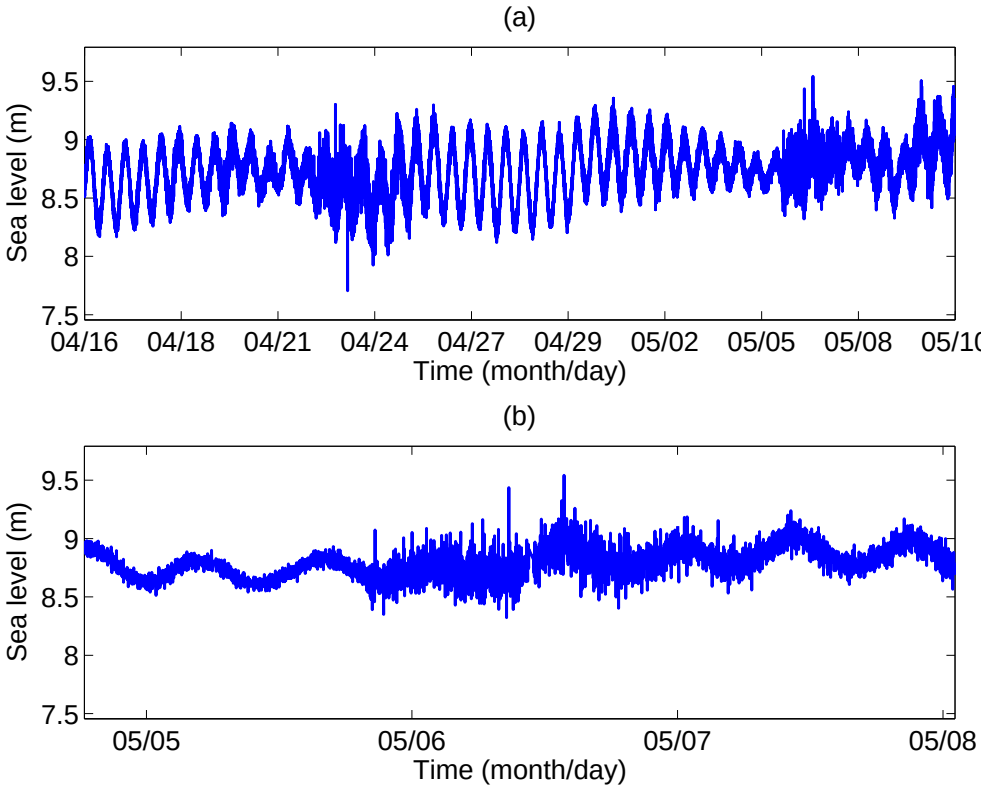

FIGURE 4.9: Wave height variation on Marion Island: (a) 2010-04-16 (day of year 106) to 2010-05-10 (day of year 130), (b) 2010-05-06 (day of year 126) to 2010-06-08 (day of year 128)

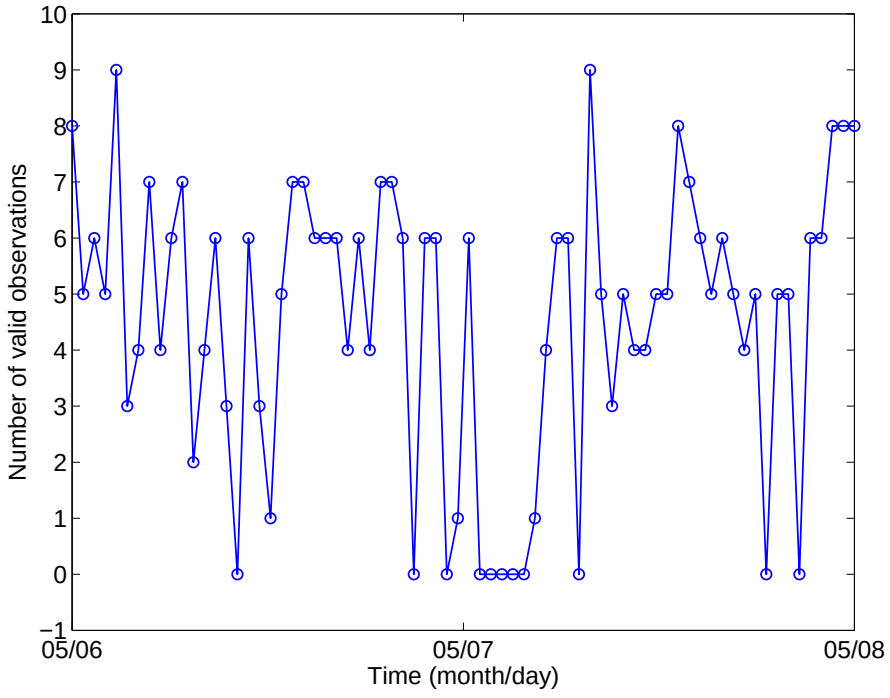

FIGURE 4.10: Number of valid satellites (satellites with complete observable sets) for 2010-06-06 (day of year 126) to 2010-06-08 (day of year 128).

Fig. 4.11(a) shows the estimation of the tidal component for the period of 25 days, and Fig. 4.11(b) shows the estimation for approximately two days.

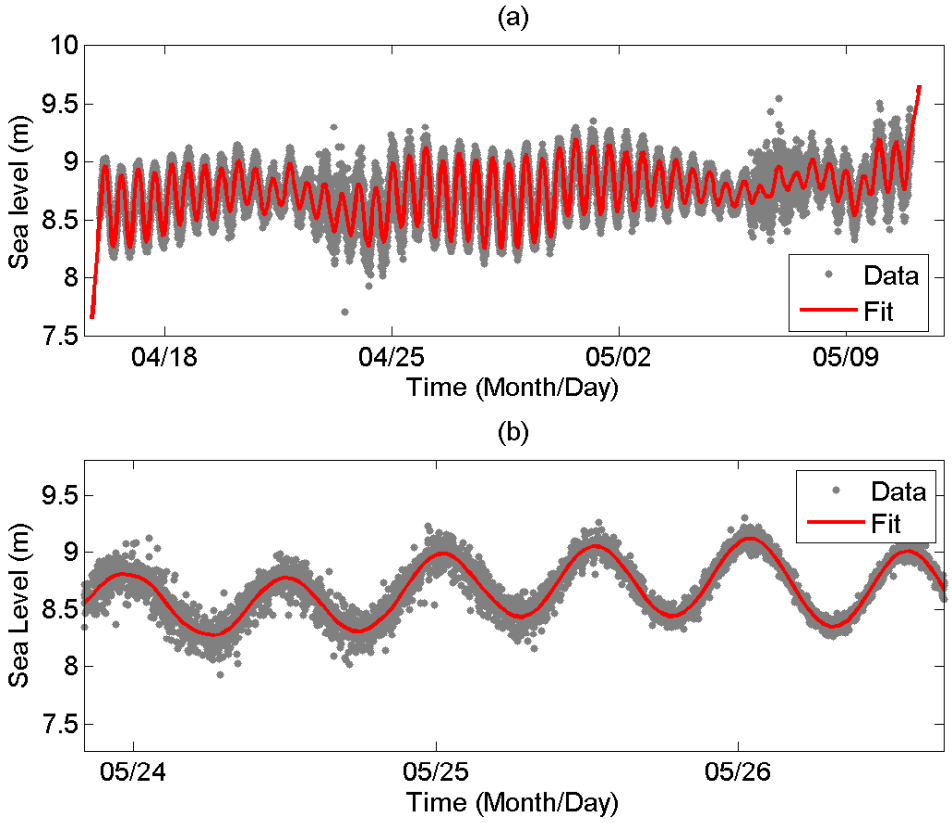

FIGURE 4.11: Wave height variation estimation from tidal variation on Marion Island for 2010-04-16 (day of year 106) until 2010-05-10 (day of year 130).

With the wave height variation now available, an hourly variation analysis was done and a correlation of ocean state with GPS data availability could be performed. To eliminate instances where the receiver could have been turned off, hours with no valid satellites were removed from the wave height variation data set before any calculations were made. An hourly wave height variation should provide a measure of how much the height of the waves vary. In other words, a turbulent sea would have a high variation around the tidal component. Since the sea level monitor samples the wave height every minute, the standard deviation of the wave height variation per hour was calculated using the 60 samples per hour. Table 4.1 shows the data characteristics of the number of valid satellites observed by the SA Agulhas receiver and the wave height variation detected by the Marion Island sea level monitor for the 25-day period.

TABLE 4.1: Data characteristics of the sea level monitor on Marion Island and the number of valid satellites observed by the GPS receiver on the SA Agulhas research vessel.

Sea Level Observations Data Characteristics	
Maximum residual	0.9031 m
Maximum hourly standard deviation	0.1584 m
Minimum hourly standard deviation	0.0263 m
SA Agulhas Data Characteristics	
Maximum valid satellites	11
Minimum valid satellites	1
Mean valid satellites	5.3889 /hour
Standard deviation	1.8020

The maximum and minimum standard deviation of the wave height variation may seem small compared to the magnitude of waves in the ocean, but the sea level monitor is located on shore (Fig. 4.7) in order to have a fixed reference level, so the variation of coastal sea levels may be significantly lower than those farther from the coastline. The correlation analysis is based on the relation between the standard deviation of the sea level per hour and the number of valid satellites per hour. However, instead of performing a correlation analysis over the full 25 days and standard deviation range, the standard deviation of the wave height variation was divided into subsets and the analysis was performed for the standard deviation of the wave height variation and the number of valid satellites corresponding to that specific standard deviation range. This would provide some additional information on the distribution of the standard deviation of the wave height variation over 25 days. The total range of the standard deviation of the wave height variation is divided in four subsets and used as levels. The maximum and minimum of these subsets correspond to the maximum and minimum hourly standard deviation. The ranges are defined in Table 4.2.

TABLE 4.2: Standard deviation of the wave height variation ranges for correlation analysis.

Range 1	0.0263 to 0.0593
Range 2	0.0593 to 0.0923
Range 3	0.0923 to 0.123
Range 4	0.123 to 0.158

Table 4.3 shows the results of the correlation analysis of the four ranges, as well as the percentage of sea level measurements falling into each respective range.

TABLE 4.3: Results of correlation analysis of quality of ship data and sea levels.

Results - Wave height variation and fraction of sea level observations			
Std. deviation range		0.0263 - 0.0593	
Correlation:	-0.0385	% sea level observations	63.1
Std. deviation range:		0.0593 - 0.0923	
Correlation:	0.0801	% sea level observations	20.6
Std. deviation range:		0.0923 - 0.125	
Correlation:	0.0880	% sea level observations	14.33
Std. deviation range:		0.125 - 0.158	
Correlation:	-0.714	% sea level observations	2

Fig. 4.12 shows a plot of the correlation coefficient as a function of range index defined in Table 4.2.

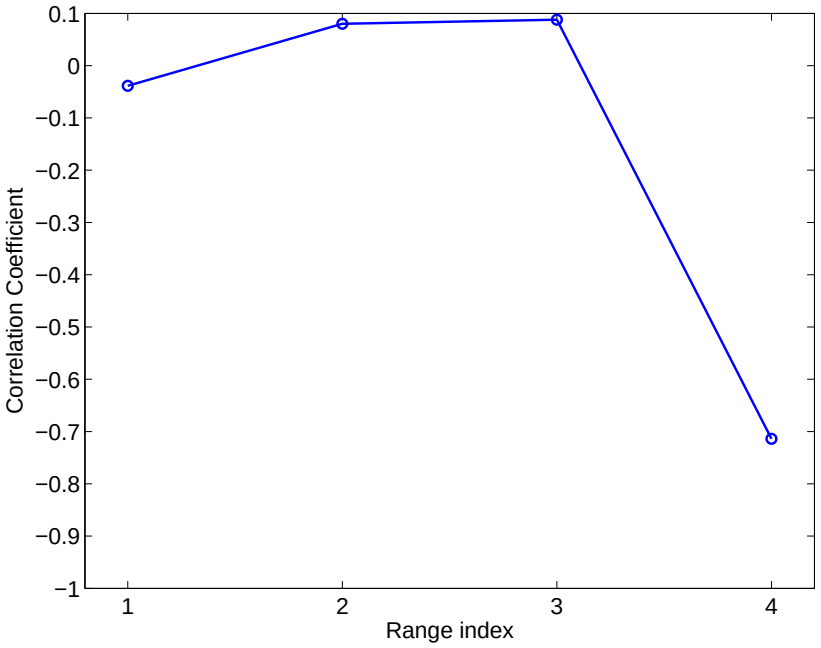

FIGURE 4.12: Correlation coefficients for sea level standard deviation and number of valid satellites.

Table 4.3 and Fig. 4.12 show that at low deviation levels, the correlation between wave height variation and number of valid satellites is close to zero. The number of valid satellites in this range are assumed to be independent of the ocean surface turbulence. However, at high wave height variation levels, a stronger negative correlation can be seen. This means that as the variation in the ocean surface increases (ocean surface becomes more uneven), the number of satellites with complete observable sets decrease. However, as seen in Table 4.3, the percentage of GPS observations affected by rough

sea levels only constitutes a minor 2 % of the 25 days of observations and is not significant. Fig. 4.13 shows a comparison of the normalised number of valid satellites and normalised wave height variation for the highest range of wave height variation (0.123 m to 0.158 m). A negative relationship can clearly be seen - this results in the negative correlation coefficient.

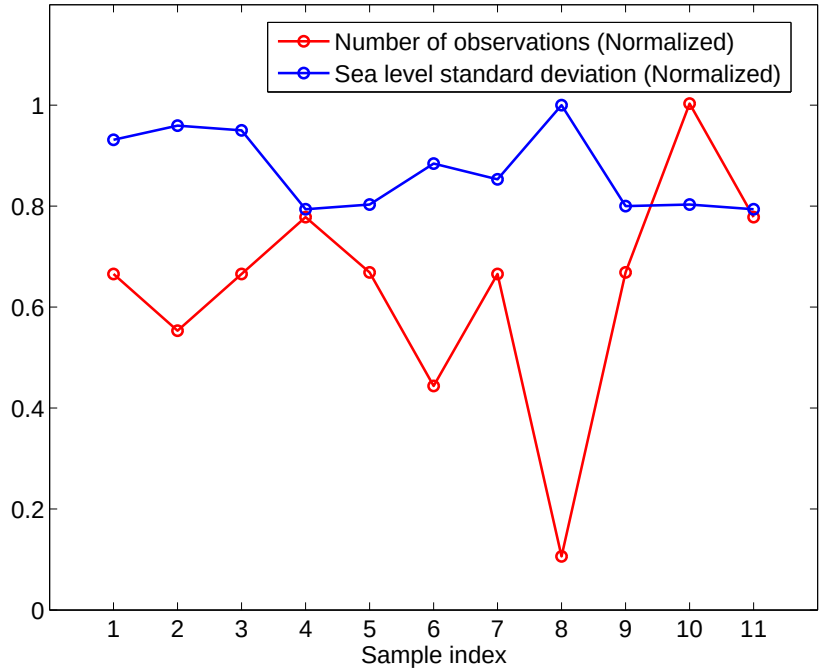

FIGURE 4.13: Normalised number of valid satellites and normalised wave height variation for the highest range of wave height variation.

4.1.3.2 Conclusion

The results suggest that the turbulence of the ocean surface only has a correlation with the number of valid satellites in extremely rough conditions. During the period studied, this data formed only a mere 2 % of the total data set for 25 days. In conclusion, the state of the ocean surface does not have a significant effect on the number of satellites with complete observable sets and further analyses needs to be done to determine the cause of the decrease in data quality from a mobile GPS receiver as opposed to a static GPS receiver.

4.2 METHOD USED FOR EXPERIMENTAL VERIFICATION

Three analyses were performed to verify the electron density maps obtained by using observables from a mobile dual-frequency GPS receiver.

1. A comparison was made between the electron density height profiles generated via inversion using observables from a mobile GPS receiver and the profiles from an ionosonde currently in operation at the Hermanus Magnetic Observatory (HMO), South Africa.

2. A comparison was made between electron density maps generated from observables from the GPS receiver on board the SA Agulhas and those generated from observables from static land-based GPS receivers for a period when the ship was near such land-based receivers.

3. A comparison was made between predicted HF propagation paths and propagation results from the HF Beacon experiment. The predictions were based on electron density maps generated from GPS observables from the SA Agulhas GPS receiver as well as electron density maps generated using the IRI2007 model.

An in-depth discussion of each of these methods are presented in the sections that follow.

GPS observables used for the verification were collected from the Ashtech Z-FX dual-frequency GPS receiver on board the SA Agulhas. As far as is known, this is the only vessel with a mobile dual-frequency receiver for the purpose of ionospheric tomography. The author personally monitored the data collection as a participant in the annual relief voyage to Antarctica during the period December 2009 to February 2010 and also during a construction voyage to Marion Island in August 2010. A schematic of the experimental setup is shown in Fig. 4.14. Fig. 4.15 shows pictures of the different components installed on board the SA Agulhas. The data was collected and downloaded via portable storage during each voyage.

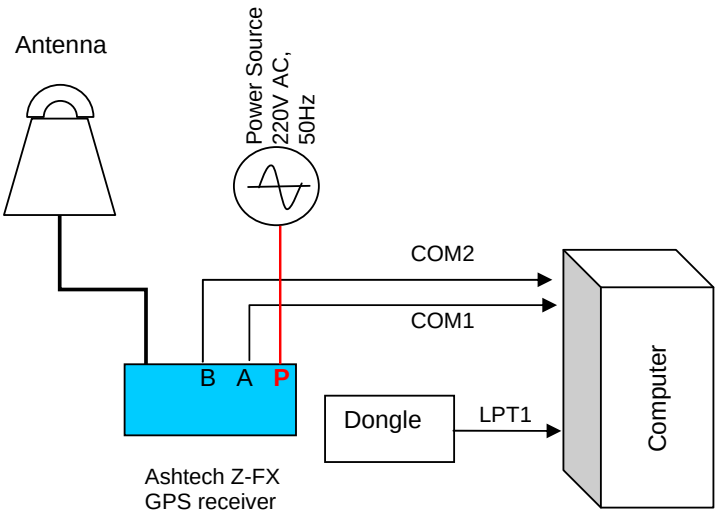

FIGURE 4.14: Experimental setup of the dual-frequency Ashtech GPS receiver on board the SA Agulhas. Taken from [26], with permission.

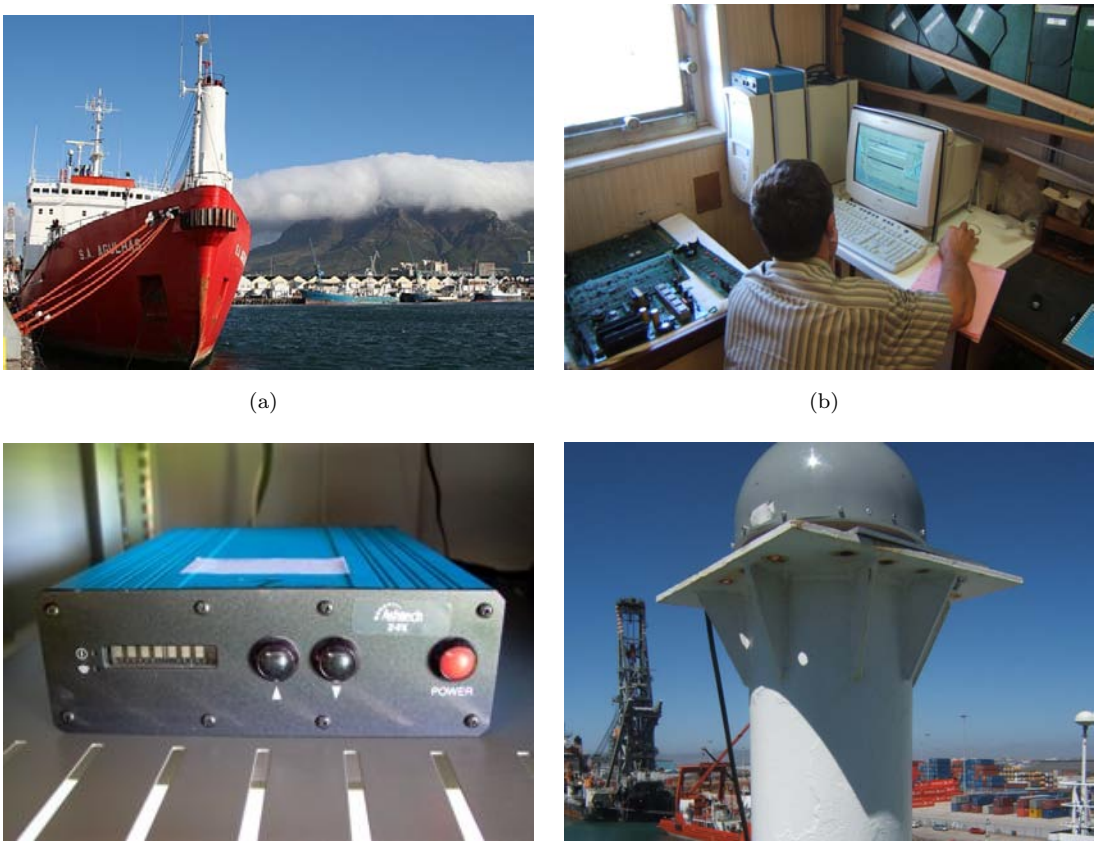

(a) (b)

(c) (d)

FIGURE 4.15: Experimental setup on the SA Agulhas: (a) The SA Agulhas research vessel, (b) The receiver and computer setup on the SA Agulhas, (c) The Ashtech Z-FX GPS receiver (d) The Ashtech choke ring antenna installation on the SA Agulhas. Taken from [26], with permission.

4.2.1 Bias estimation and its considerations

Interfrequency bias was briefly discussed in Chapter 2 and is defined as the TEC observation offset caused by hardware delays in satellites and receivers. Recall that the receiver offset B_r and the satellite offset B_s are evident in (2.27):

$$P_I^F = 40.3(\frac{1}{f_2^2} - \frac{1}{f_1^2})I + B_r + B_s.$$

The Multi-Instrument Data Analysis System (MIDAS) package used for the TEC inversion in this dissertation does contain a bias estimation function. This function implements the method discussed in Section 2.2.4.3 and adds the biases to the slant TEC input data to obtain bias-corrected slant TEC values. As mentioned in Section 2.2.4.3, more accurate bias results could be obtained if the hourly biases were averaged over a longer period of time. Ideally, once the bias values for a specific satellite or receiver are determined, this value should not change rapidly assuming there are no hardware changes. However, small drifts in bias values may be observed because of ageing hardware and other environmental effects. The Center for Orbit Determination in Europe (CODE), provides monthly average bias values for satellites in the GPS network. However, the advantage of using the MIDAS method for bias estimation is that, since MIDAS uses current TEC only to estimate the biases, MIDAS would detect changes in bias values (if a hardware change occurs in the satellite or receiver) sooner than the CODE bias values would detect a change. This was demonstrated for the Caiscais GPS receiver in Portugal [24], where a change of hardware on 2002-07-10 (day of year 191) could clearly be seen in the MIDAS bias estimation results (see Fig. 4.16). However, for the case in Fig. 4.16, the MIDAS method of determining biases did not seem to be reliable considering the variation of bias values. Dear [24] found that the RMS, mean and absolute differences between hourly bias values calculated by MIDAS for a specific day and the long-term CODE bias values were 2.005 nanoseconds (5.779 TECU), 0.354 nanoseconds (1.02 TECU) and 1.597 nanoseconds (4.603 TECU) respectively. Over a period of a year, the averaged sampled data bias values calculated by MIDAS and those released by CODE had RMS, mean and absolute differences of 1.643 nanoseconds (4.736 TECU), -0.473 nanoseconds (1.363 TECU) and 1.158 nanoseconds (3.338 TECU) respectively [24]. This does not show a significant increase in similarity and questions the accuracy of either method. Nevertheless, a good correlation exists between the bias values obtained by MIDAS and by CODE (98 % - 99 %) [24]. However, even within MIDAS, a certain level of variation exists

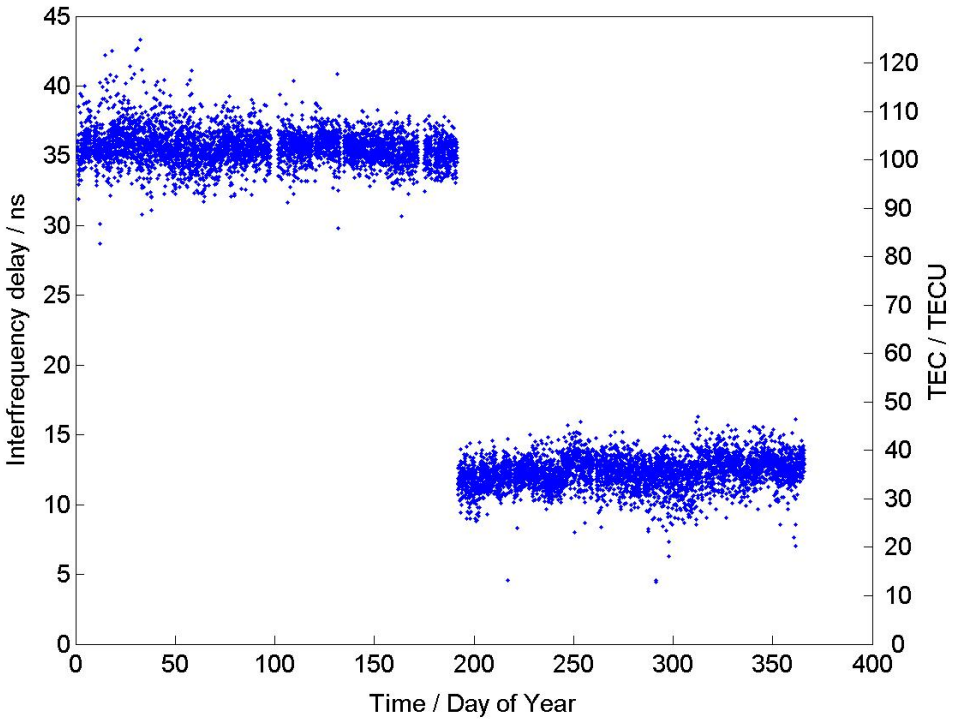

FIGURE 4.16: Cascais receiver interfrequency bias estimation using MIDAS. Taken from [24], with permission.

between bias estimation for the same satellites with different receivers. To illustrate, slant TEC for the Cape Town and SA Agulhas GPS receivers for 2010-05-20 (day of year 140) were analysed. On this day, the ship was relatively close to shore and close to the Cape Town receiver. Thus the RINEX observables and the slant TEC should have been similar for the same satellites. Fig. 4.17 shows a comparison of slant TEC values after MIDAS bias correction for two satellites during 05:00 - 06:00 UT for the CTWN and AGHL GPS receivers. It can clearly be seen that slant TEC values follow a similar trend, but are offset by a constant TEC value. Table 4.4 lists the absolute mean differences between the mean TEC values for the AGHL and CTWN receivers for 05:00 - 06:00 UT 2010-05-20 (day of year 140).

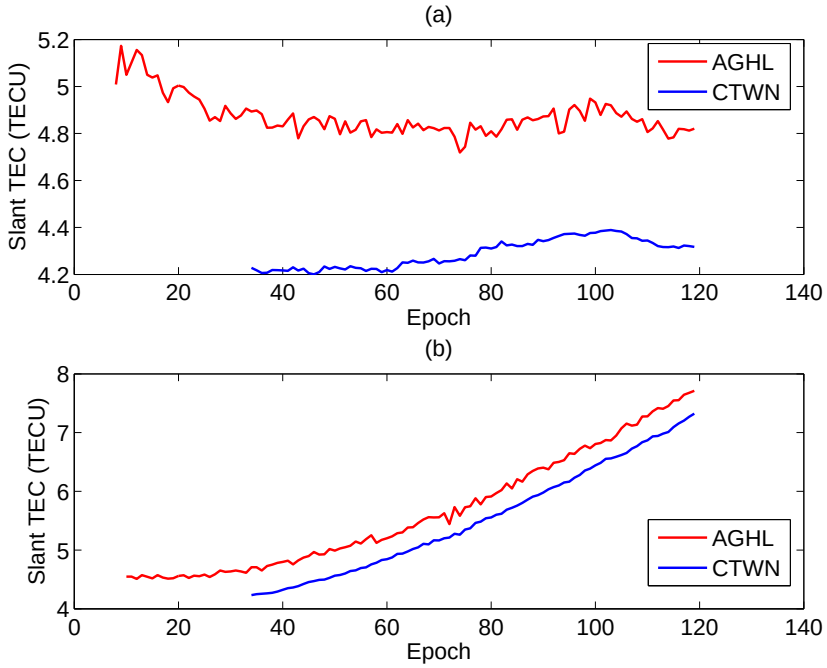

FIGURE 4.17: Slant TEC values for the Cape Town and SA Agulhas GPS receivers with bias correction for the time period 05:00 - 06:00 UT on 2010-05-20 (day of year 140): (a) Satellite - PRN0019. (b) Satellite - PRN0023.

TABLE 4.4: Absolute differences in bias values: AGHL-CTWN, 05:00 - 06:00 UT on 2010-05-20 (day of year 140).

Satellite PRN	3	6	7	13	16	19	23
Absolute difference (TECU)	1.899	2.1781	0.51344	1.9798	2.792	1.693	2.0784
Mean	1.8766 TECU						

The mean of the absolute differences of the bias offset between the satellite receiver pairs is shown in Table 4.4 as 1.8766 TECU, which is lower than the values which Dear [24] found in his comparison between the MIDAS method and CODE bias values. However, as mentioned in Section 2.2.4.3, the bias estimation is strongly dependent on the match between the measured STEC and the basis functions used, and differences in these parameters can also cause a variation in bias values. These effects are discussed in Section 4.2.2. The author believes that, based on the data presented, the extra processing needed to incorporate external data for bias correction - especially for a network of mobile receivers - is not worth the possible performance gain achieved by Dear [24]. Furthermore, this is only a performance gain if it is assumed that the CODE estimated bias values are more accurate than the MIDAS estimated bias values. However, if the process MIDAS follows in performing the TEC inversion is considered (discussed in Section 2.2.4), since the data values differ (although only with a relatively constant magnitude), the MIDAS inversion may produce a slightly different electron

density map. In the fortunate event that the research vessel is close to a land-based absolute electron density measurement instrument, such as an ionosonde, the vessel's electron density observations can be calibrated to the land-based electron density observations before the inversion is performed using a mean offset shift - a process similar to that used for levelling LTEC onto PTEC (explained in Chapter 2). However, when the research vessel is far from land, this is not possible.

Considering these factors, the author has chosen to accept the hourly bias values calculated by MIDAS, without any external data input or averaging. Further investigation into the estimation of bias values as determined by the basis functions is presented in Section 4.2.2.

4.2.2 Determination of basis functions (EOFs)

The process to determine optimal EOFs is similar to the process followed in Section 3.1.2. To determine the optimal parameters for EOF generation, absolute measurements provided by the Hermanus Magnetic Observatory ionosonde were used. The results of the MIDAS inversion were compared with the ionosonde results for a number of EOF parameters. The best results were chosen based on this comparison.

Considerations affecting bias estimation by MIDAS were discussed in Section 4.2.1. As mentioned, the MIDAS algorithm bias estimation values are strongly dependent on the residuals from the inversion results. The residuals however, are directly related to the EOFs (see Section 2.2.4.3 and 4.2.1). As a result, the bias values were also taken into account in the determination of the EOFs.

Since an ionosonde provides an absolute measuring technique, the absolute values obtained by the ionosonde can be compared to the values obtained by MIDAS.

Performance evaluation

Two criteria were taken into account for the comparison between ionosonde- and MIDAS-generated electron density profiles:

- Root mean square difference between the ionosonde electron density profile and the MIDAS electron density profile. The root mean square difference is defined

as:

$$RMSD = \sqrt{< (Ne_{model} - Ne_{inversion})^2 >} \, , \tag{4.3}$$

where "<>" indicates averaging over the difference of the two profiles. The advantage of using the RMSD lies in the fact that a larger weight is assigned to outliers. Electron density profiles typically have a peak of high electron density and areas of low electron density. The differences found in low electron density areas will generally be smaller because of a small electron density variation. However, differences at the peak electron density and the surrounding area may still be large. The RMSD emphasizes differences in the peak electron density areas.

- Bias offset between the ionosonde profile and the MIDAS-generated profile. It is generally known that electron density tends to zero at altitudes beyond 1 000 km. The electron density offset between the ionosonde profile and the MIDAS profile at an altitude of 900 km was used for this evaluation and correction.

4.2.2.1 Model-dependent basis functions parameters

To determine the model-dependent parameters for the experimental verification, the same procedure as with the IRI2007 model used in simulations was followed and the reader is referred to Section 3.1.2.1 for an explanation of this process.

4.2.2.2 Ionosonde-based EOF generation

Regardless of how the model-dependent parameters are determined (explained in Section 4.2.2.1), the optimal model-independent parameters used for EOF generation has to be determined. Fortunately, the SA Agulhas, on its voyages to Marion Island, passes within 15 km from the ionosonde at the Hermanus Magnetic Observatory and profiles from this ionosonde can be used to calibrate the independent parameters used for the EOF generation. The ionosonde profiles were obtained with permission from the Lowell Digital Ionogram Data Base (`http://ulcar.uml.edu/DIDBase/`).

During its return voyage from Marion Island, the ship was close to the HMO ionosonde during the period 08:00 - 09:00 UT on 2010-05-19 (day of year 139). The inversion results obtained from the observations made during this period were used for the ionosonde verification in order to determine the EOF parameters. Fig 4.18 shows

the position of the SA Agulhas during this period.

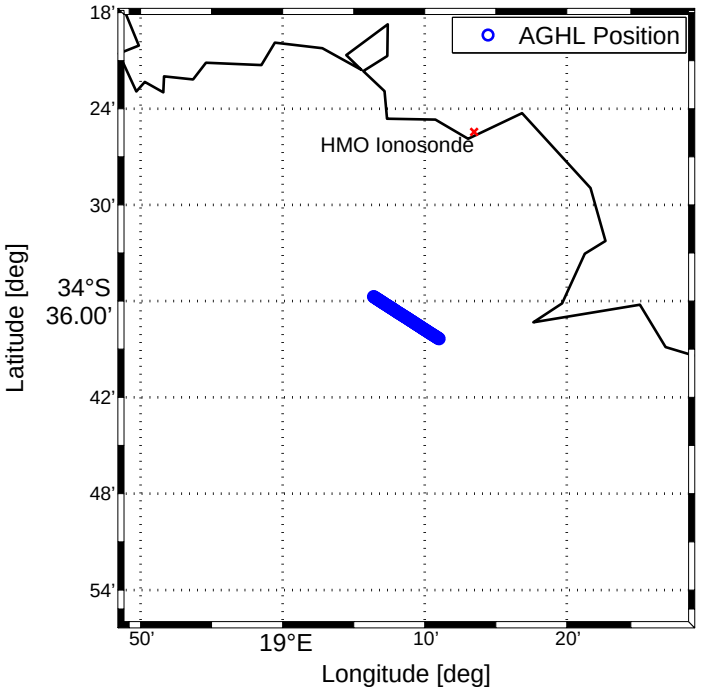

FIGURE 4.18: SA Agulhas position for the period 08:00 - 09:00 UT on 2010-05-19 (day of year 139).

Three model-independent variables were changed in the EOF generation settings to determine the optimal values:

- Type of EOFs - CHAPMAN or EPSTEIN.
- Number of EOFs used - 1,3,5,7.
- Order of longitude (Mmax) and latitude (Nmax) harmonics - 16,12,8,4.

The peak height and scale height of the primary profile above the ship's position was determined by the process explained in Section 4.2.2.1:

- Peak height: 230 km, Scale height: 55 km.

To generate more EOFs, the procedure outlined in [24] was followed, where more EOFs are added either side of the primary EOF generated by the IRI2007 model:

- Three basis functions used

  - Peak height: 200 km, Scale height: 55 km
  - Peak height: 230 km, Scale height: 55 km
  - Peak height: 260 km, Scale height: 55 km

- Five basis functions used
  - Peak height: 200 km, Scale height: {45,55} km
  - Peak height: 230 km, Scale height: 55 km
  - Peak height: 260 km, Scale height: {55,65} km

- Seven basis functions used
  - Peak height: 200 km, Scale height: {45,55} km
  - Peak height: 230 km, Scale height: 45,55,65 km
  - Peak height: 260 km, Scale height: {55,65} km

Initially, only analyses based on the type and number of EOFs were performed for a fixed order of longitude (Mmax) and latitude (Nmax) harmonics (Nmax/Mmax = 8/8). Table 4.5 shows the results for this analysis according to the performance evaluation criteria discussed in the introduction of Section 4.2.2. The optimal number of EOFs to be used were determined from these results and used to analyse the influence of Nmax and Mmax.

TABLE 4.5: Results - performance as a function of the type and number of EOFs used for 08:00 - 09:00 UT on 2010-05-19 (day of year 139).

EOF type	No. of EOFs	Nmax/Mmax	RMSD ($\times 10^{12}$ $\frac{e}{m^3}$)	Bias offset ($\times 10^{12}$ $\frac{e}{m^3}$)
CHAPMAN	1	8/8	0.0437	0.6429
CHAPMAN	3	8/8	0.0381	1.6133
CHAPMAN	5	8/8	0.0361	1.0904
CHAPMAN	7	8/8	0.045	0.9958
EPSTEIN	1	8/8	0.0308	0.338
EPSTEIN	3	8/8	0.0558	1.3895
EPSTEIN	5	8/8	0.0385	1.0864
EPSTEIN	7	8/8	0.0476	1.0196

Fig. 4.19 shows a plot of the results shown in Table 4.5.

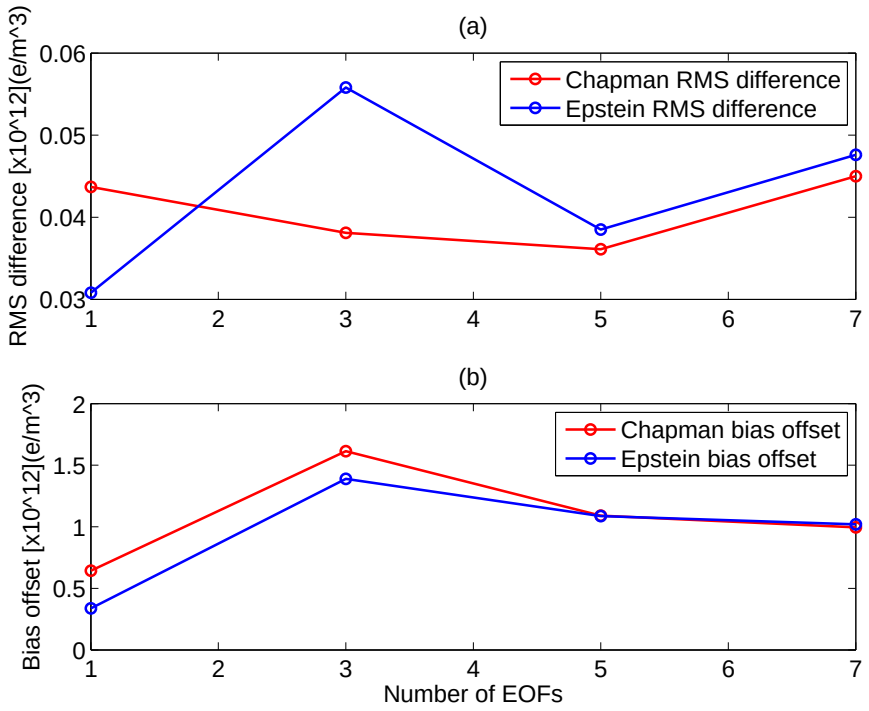

FIGURE 4.19: Performance as a function of the type and number of EOFs used for the period 08:00 - 09:00 UT on 2010-05-19 (day of year 139).

In Fig. 4.19 and Table 4.5, the RMS differences are very small and do not provide a definitive result, similar to the scenario discussed in Section 3.1.1. However, in terms of bias offset, the Epstein profile clearly has the lowest bias offset. This occurs when only one EOF is used. This means that in this case, the difference between the measured TEC and the basis functions cause the bias estimation algorithm in MIDAS to reach the correct bias value, as explained in Section 2.2.4.3. As a result, one Epstein profile EOF was used for the analysis of performance as a function of order of longitude (Mmax) and latitude (Nmax) harmonics. Results are shown in Table 4.6 and Fig. 4.20.

TABLE 4.6: Results - performance as a function of order of longitude (Mmax) and latitude (Nmax) harmonics for 08:00 - 09:00 UT on 2010-05-19 (day of year 139).

EOF type	No. of EOFs	Nmax/Mmax	RMS ($\times 10^{12}$ $\frac{e}{m^3}$)	Bias offset ($\times 10^{12}$ $\frac{e}{m^3}$)
EPSTEIN	1	16/16	0.1799	1.4698
EPSTEIN	1	12/12	0.0334	0.657
EPSTEIN	1	8/8	0.0308	0.339
EPSTEIN	1	4/4	0.0303	0.0000045

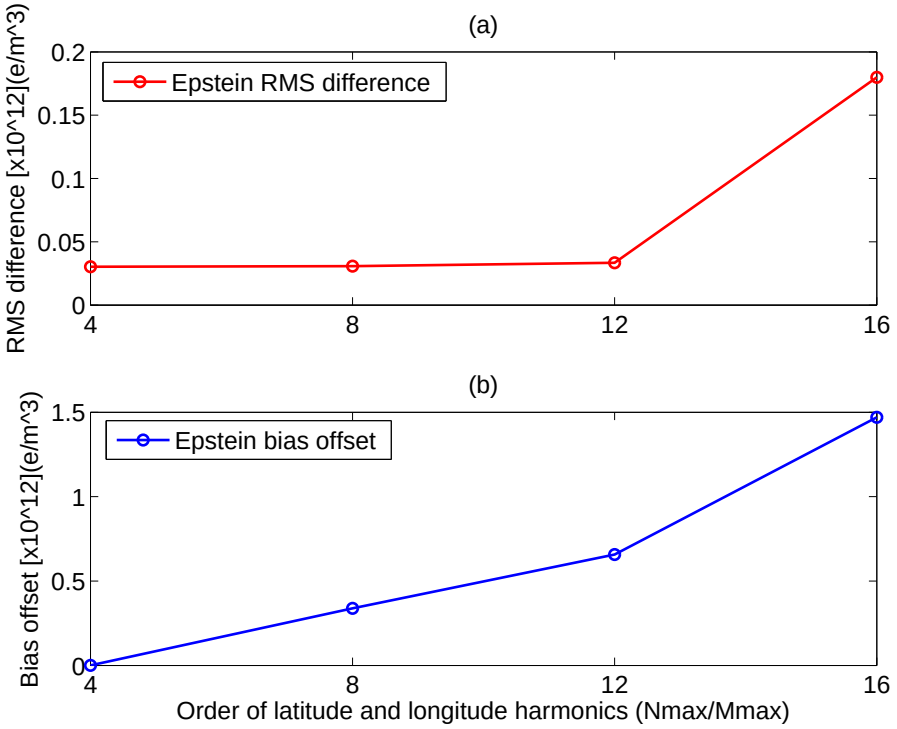

FIGURE 4.20: Performance as a function of the order of longitude (Mmax) and latitude (Nmax) harmonics used for the period 08:00 - 09:00 UT on 2010-05-19 (day of year 139).

Fig. 4.20 does not show a significant change in RMSD values from using [Nmax/Mmax = 12/12] compared to [Nmax/Mmax = 4/4], but shows a clear decrease in bias offset for decreasing order of latitude and longitude harmonics. The purpose of the order of the longitude and latitude harmonics variable is to make provision for higher order variations in the electron density distribution in the latitude and longitude plane. This variation is typically related to the severity of magnetic storms - in storm conditions the variations in the horizontal plane tend to be of a higher order than during magnetically quiet conditions. It may be that the current results are only accurate for quiet magnetic conditions - for the period of interest the magnitude of the DST index was 9 nT which is considered magnetically quiet. Furthermore, since the results suggest that the bias offset in comparison with an absolute measurement from an ionosonde is lower, this implies that the fit of the observations to the EOF used is better and the resultant residuals are more accurate (see sections 2.2.4.3 and 4.2.1). Figs. 4.21 and 4.22 shows a qualitative comparison of the results obtained by using one EOF with [Nmax/Mmax = 8/8] and [Nmax/Mmax = 4/4] respectively. In the case of [Nmax/Mmax = 4/4], the original MIDAS profile is not visible, because it is located directly underneath the theoretically "shifted" MIDAS profile - in other words the bias offset is negligible.

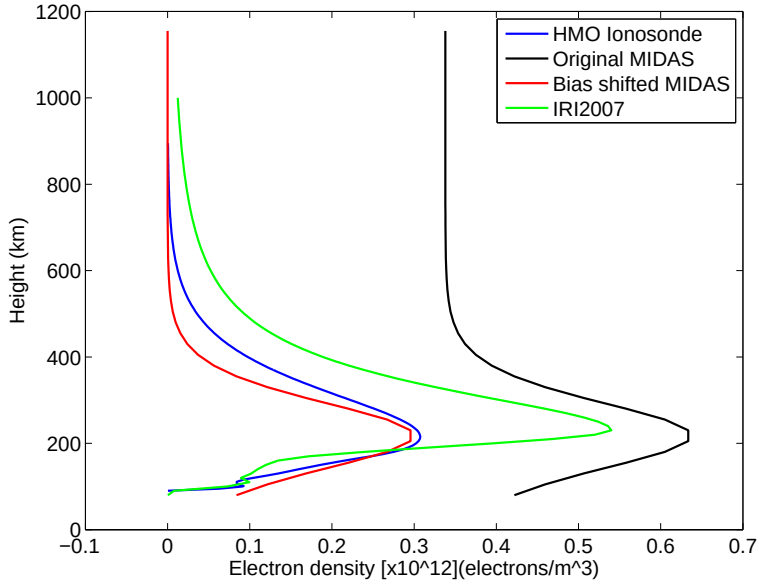

FIGURE 4.21: Comparison of electron density profiles using one EOF with Nmax and Mmax equal to 8 at the HMO Ionosonde for the period 08:00 - 09:00 UT on 2010-05-19 (day of year 139).

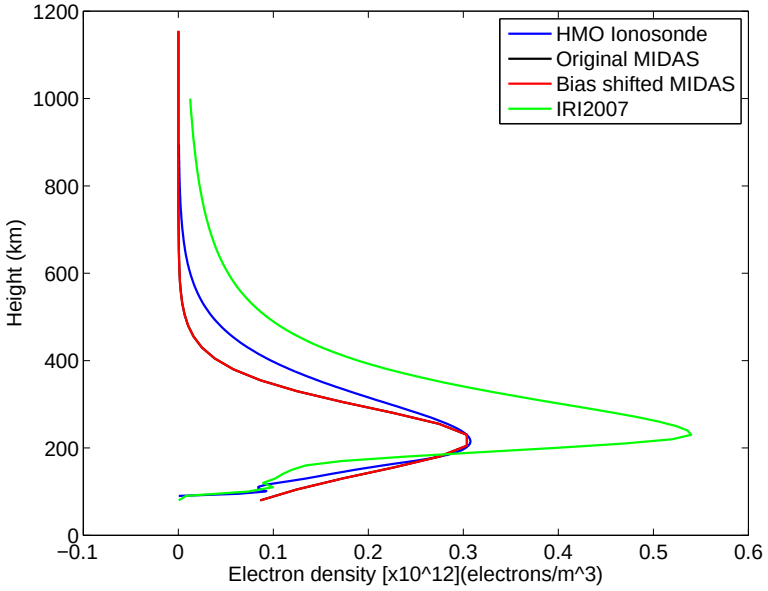

FIGURE 4.22: Comparison of electron density profiles using one EOF with Nmax and Mmax equal to 4 at the HMO Ionosonde for the period 08:00 - 09:00 UT on 2010-05-19 (day of year 139).

Based on this analysis, only one Epstein EOF with [Nmax/Mmax = 4/4] was used in this chapter.

4.2.3 Data quality and MIDAS inversion settings

The data quality settings (Section 4.1), and MIDAS inversion settings common to all inversions, are shown in Table 4.7.

TABLE 4.7: Data quality and MIDAS inversion settings common to all inversions.

Data quality settings	
Data smoothing sample width	6
Cycle slip correction THR	1.5 TECU
Elevation angle cutoff	20°
Minimum number of valid satellites	4
Minimum fraction of the ideal number of ray paths (F_t)	0.5
MIDAS Inversion Settings	
Number of EOFs	1
Type of EOF	Epstein
Nmax/Mmax	4/4

All other unique parameters used are specified in each section.

4.3 IONOSONDE VERIFICATION

Ionosondes are devices capable of measuring electron density profile values up to h_mF2, the critical height in the F2-layer, as discussed in Section 2.3.1. The electron density values measured by ionosondes are absolute, and provide a way of verifying absolute electron density values generated by the MIDAS inversion using GPS observables from the mobile GPS receiver.

4.3.1 Method

As discussed in Section 4.2.2.2, the SA Agulhas research vessel passes within 15 km of the ionosonde at the Hermanus Magnetic Observatory and profiles from this ionosonde can be used to verify the electron density maps obtained by the MIDAS inversion. The ionosonde profiles were obtained with permission from the Lowell Digital Ionogram Data Base. Since this ionosonde was used for EOF generation in Section 4.2.2.2, additional verifications should provide additional confirmation that the MIDAS inversion functions correctly. The IRI2007 model electron density profile for the period of interest was also compared with the HMO ionosonde electron density profile.

4.3.1.1 Performance evaluation

The same performance evaluation criteria used in Section 4.2.2 for EOF generation was used for the evaluation of the ionosonde verification.

4.3.2 Case study: 2010-04-08 (day of year 98)

Between 19:00 - 20:00 UT on 2010-04-08 (day of year 98), the SA Agulhas passed within 15 km of the HMO ionosonde on its outbound voyage to Marion Island. GPS observables from this period were used for the ionosonde verification. Fig. 4.23 shows the position of the ship during the period 19:00 - 20:00 UT on 2010-04-08 (day of year 98).

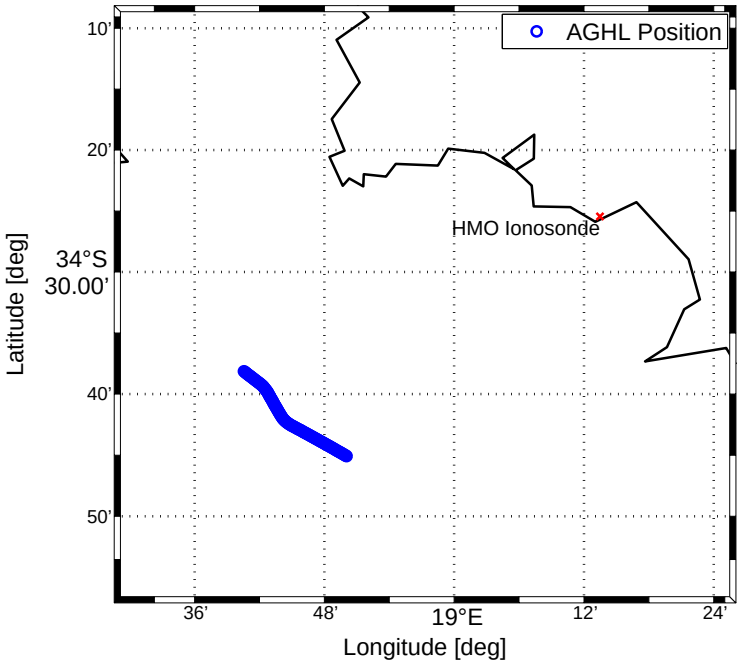

FIGURE 4.23: SA Agulhas position for the period 19:00 - 20:00 UT on 2010-04-08 (day of year 98).

Table 4.12 shows the inversion settings used, calculated as shown in Section 4.2.2.

TABLE 4.8: Settings for the AGHL-HMO electron density profile comparison for 19:00 - 20:00 UT on 2010-04-08 (day of year 98).

MIDAS inversion settings	
EOF peak height	**EOF scale height**
295 km (IRI2007)	70 km (IRI2007)

Fig. 4.24 shows a comparison of the electron density profiles directly above the ionosonde according to the AGHL-based profile, the IRI2007 model and the HMO ionosonde. Table 4.9 shows the results obtained with the performance criteria specified in Section 4.3.1.1.

TABLE 4.9: Results - comparison of AGHL and IRI2007 with HMO ionosonde electron density profiles for 19:00 - 20:00 UT on 2010-04-08 (day of year 98).

Profile	RMSD ($\times 10^{12}$ $\frac{e}{m^3}$)	Bias offset ($\times 10^{12}$ $\frac{e}{m^3}$)
AGHL	0.0473	0.000063
IRI2007	0.02	N/A

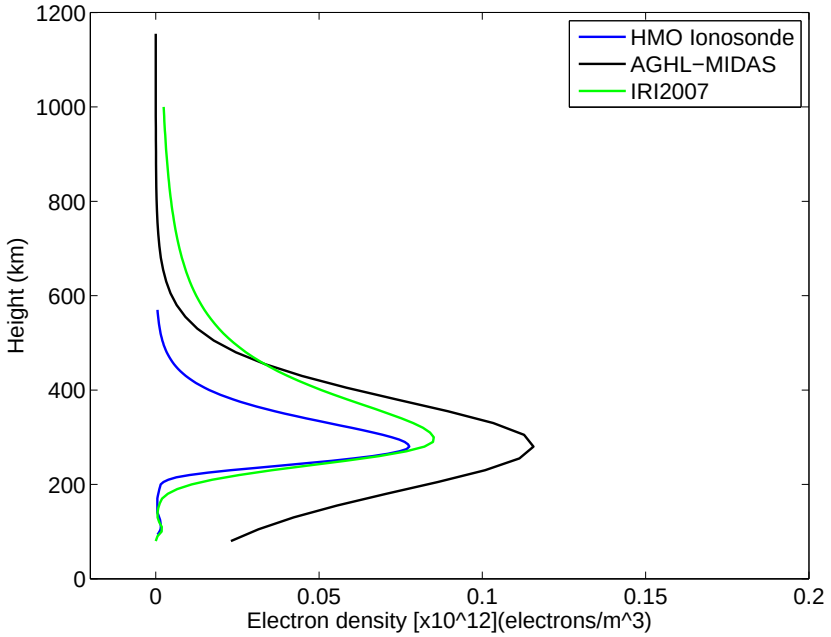

FIGURE 4.24: Comparison of the electron density profiles directly above the ionosonde according to the AGHL-based profile, the IRI2007 and the HMO ionosonde for the period 19:00 - 20:00 UT on 2010-04-08 (day of year 98).

In Fig. 4.24 the absolute difference between the AGHL-generated and the HMO ionosonde electron density profile may seem large. However, when the scale of the electron density are taken into account, the absolute differences are less than 0.1×10^{12} $\frac{\text{e}}{\text{m}^3}$ in magnitude. Since the profiles were generated at night time, the electron density is generally low. The RMSD value for the AGHL electron density profile and the HMO ionosonde profile agrees with values obtained in Section 4.2.2.2, (0.0303×10^{12} $\frac{\text{e}}{\text{m}^3}$) where the ionosonde data was used to generate EOFs. This demonstrates consistency in the results obtained.

4.3.3 Conclusion

The results obtained agree with the RMSD values obtained in Section 4.2.2.2 and thus demonstrate a consistency. There is a good correlation between the electron density profile obtained from the HMO ionosonde, which is an absolute measurement, and the electron density profile generated by the MIDAS inversion of GPS observables from the SA Agulhas.

4.4 STATIC GPS RECEIVER VERIFICATION

To verify that the GPS observables on board the SA Agulhas are received and processed correctly, electron density maps generated from mobile GPS receiver observables were compared to those generated from static GPS receiver observables. This does not necessarily mean that the inversions are correct, but it at least provides some assurance that the observables obtained from the ship and their processing are not arbitrary. Furthermore, data from static GPS receivers have been used for ionospheric tomography for some time. Thus if the profiles agree, it can be argued that ionospheric tomography using mobile GPS observables can also be deemed trustworthy.

TrigNet is a network of permanent continuously operating GNSS base stations distributed throughout South Africa. These stations are spaced approximately 100 km to 300 km. Fig. 4.25 shows the TrigNet network of GPS receivers in South Africa.

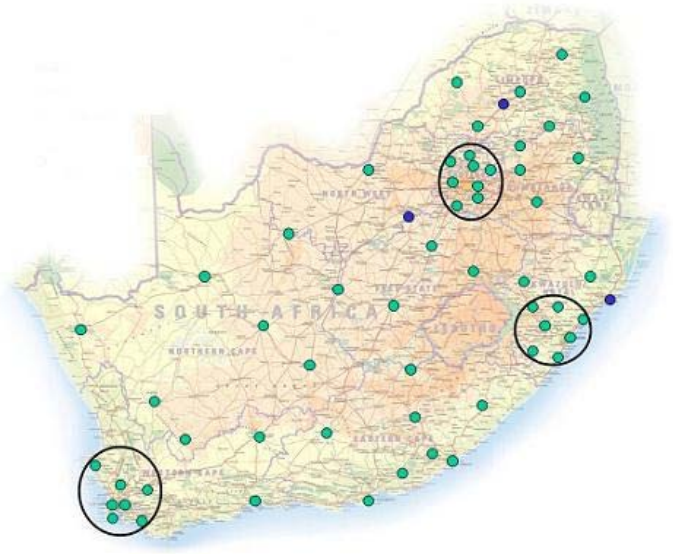

FIGURE 4.25: Trignet stations in South Africa - with permission from the Chief Directorate: National Geospatial Information (NGI)

Several receivers are located on the Cape coastline, close to the harbour where the SA Agulhas research vessel is docked. Furthermore, the South African National Antarctic Programme (SANAP) also has static GPS receivers installed at bases in Antarctica (SANAE) and on Marion Island and Gough Island. The SA Agulhas research vessel visits each of these locations at least once per year. Table 4.10 lists the static dual-frequency GPS receivers that can be used for the verification.

TABLE 4.10: Static dual-frequency GPS receivers that can compared with the SA Agulhas GPS receiver.

Location	ID	Coordinates (lat; lon)
Cape Town, SA	CTWN	−33.77°; 18.46°
Hermanus, SA	HNUS	−34.24°; 19.22°
Antarctica	SANAE	−71.67°; −2.84°
Marion Island	MAR	−46.87°; −9.88°
Gough Island	GOGH	−40.34°; 18.46°

Fig. 4.26 shows the position of each of these receivers. However, in this study, only GPS observables from the CTWN and GOGH static GPS dual-frequency receivers will be used for the verification.

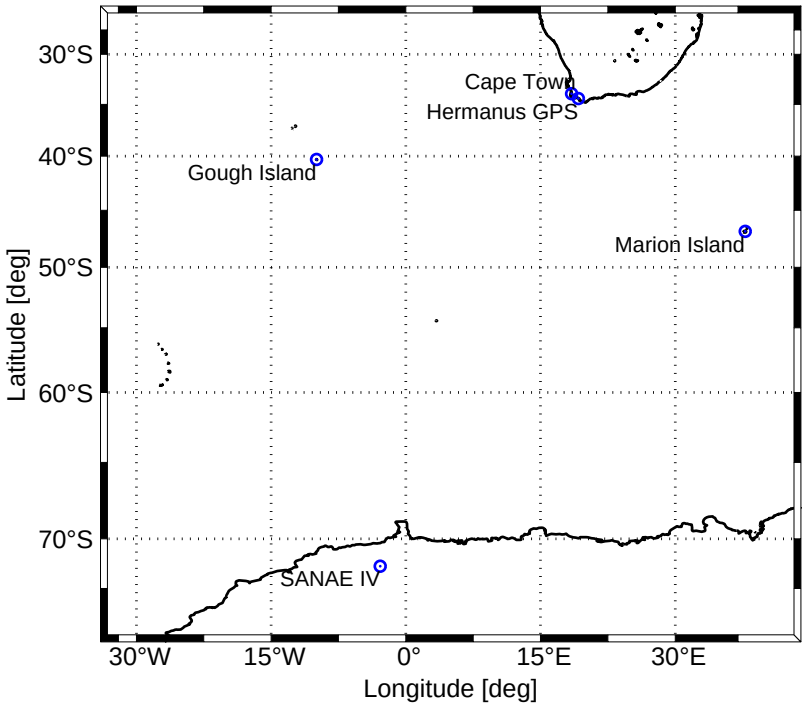

FIGURE 4.26: Static dual-frequency GPS receivers that can be used for the comparison (Trignet and SANAP GPS receivers).

4.4.1 Method

In order to make a valid comparison, GPS observables were collected from the CTWN and GOGH dual-frequency GPS receivers and preprocessed for inversion by the MIDAS algorithm for periods when the SA Agulhas was relatively close to each respective

land-based receiver. The observables from the SA Agulhas research vessel were filtered according to the quality specifications discussed in Section 4.1. The GPS static receiver observables were processed for a minimum number of observations (all observations were assumed to be valid) and total number of slant TEC values (epochs). No elevation angle cutoff filtering was performed on the static receiver observables. However, observations from the static receivers contain approximately the same number of STEC values as the AGHL data for the days analysed. The data quality criteria is specified in Section 4.2.3, with any unique values specified at each respective inversion. To obtain a suitable period for comparison, certain aspects had to be taken into account.

- **Time of day**
  The ionosphere typically has a higher electron density and a more variable electron density distribution during daytime because of the increased ionisation caused by rays from the Sun. A higher variation in electron density makes it easier to compare results, since the difference between peaks and troughs in electron density maps are larger. For this reason, daytime and a period of high electron density distribution variation are preferred.

- **Number of visible satellites**
  To obtain a valid comparison, the land-based receiver and the SA Agulhas receiver must have approximately the same satellite visibility.

- **Number of total slant TEC values**
  Although the number of visible satellites can be the same, the Cape Town receiver and the SA Agulhas receiver must also have approximately the same number of epochs to qualify for a valid comparison.

4.4.1.1 Performance evaluation

The purpose of this experiment was to compare electron density maps generated from mobile GPS receiver observables to electron density maps generated from static GPS receiver observables. Two criteria were taken into account to compare these two profiles:

- Plots of electron density distributions and vertical total electron content (Qualitative)

- Root mean square deviation (Quantitative)

Electron density distribution plots and total electron content plots were compared.

To provide a quantitative measure of the similarity of the electron density maps generated from the GPS observables from the mobile and static receivers, the root mean square difference (RMSD) for the two profiles were calculated. Calculation of the RMSD is shown in (4.3).

4.4.2 Results

4.4.2.1 Case study 1: Cape Town (CTWN)

When the SA Agulhas returned from its annual Marion Island relief voyage the ship was close to the Cape Town Harbour on 2010-05-19 (day of year 139). Considering the aspects important for selecting a suitable period (see Section 4.4.1), the period 16:00 - 17:00 UT on 2010-05-19 (day of year 139) was chosen. Fig. 4.27 shows the ship's position during this period. Table 4.11 provides statistics for the difference between slant TEC values of the satellites seen by both the AGHL and CTWN GPS receivers. The values agree with bias estimation variation values in the literature, as discussed in Section 4.2.1. Table 4.12 shows the settings used for data quality processing and MIDAS inversion. Data preprocessing was performed on the AGHL and CTWN data, as discussed in Section 4.1 and 4.2.1. Figs. 4.28 to 4.31 show the plots of electron density distributions and vertical total electron content for the CTWN and AGHL receivers respectively. The RMSD calculated for the AGHL and CTWN electron density maps was 0.0058×10^{12} $\frac{\mathrm{e}}{\mathrm{m}^3}$ (see Section 4.4.1.1).

TABLE 4.11: Statistics of the slant TEC differences: AGHL-CTWN comparison.

Mean	2.6 TECU
Maximum	3.7 TECU
Minimum	1.7 TECU

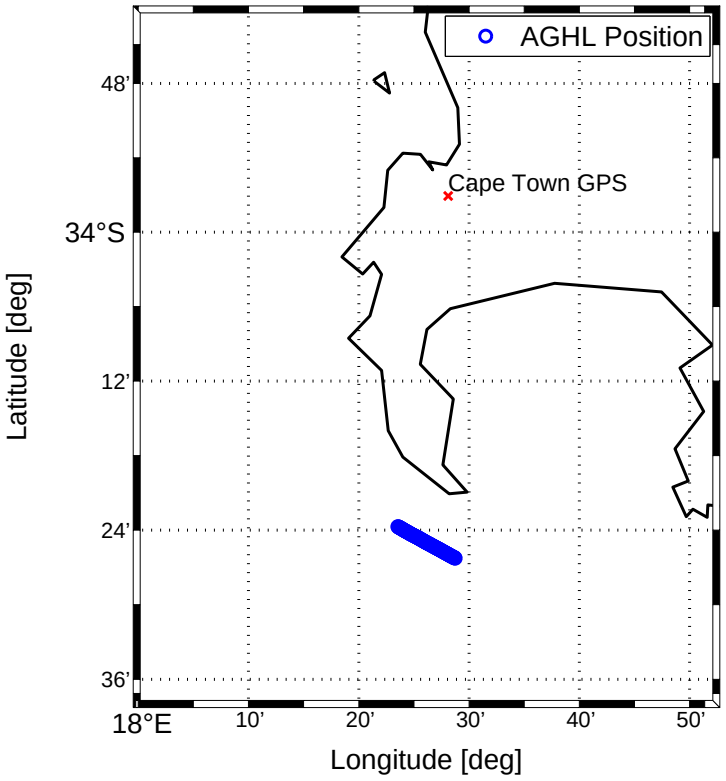

FIGURE 4.27: SA Agulhas position for the period 16:00 - 17:00 UT on 2010-05-19 (day of year 139).

TABLE 4.12: Settings for the AGHL-CTWN receiver comparison for the period 16:00 - 17:00 UT on 2010-05-19 (day of year 139).

Settings for AGHL-CTWN comparison	
Data and quality control settings	
CTWN	
No. of ray paths removed (elevation angle THR)	289
No. of satellites	7
No. of epochs used	506
AGHL	
No. of ray paths removed (elevation angle THR)	53
No. of satellites	7
No. of epochs used	701
MIDAS inversion settings	
Distance cutoff	Elev. angle
Distance cutoff parameter	$\frac{2}{3}$(GridMax) km
EOF peak height	**EOF scale height**
CTWN	
260 km (IRI2007)	80 km (IRI2007)
AGHL	
260 km (IRI2007)	60 km (IRI2007)

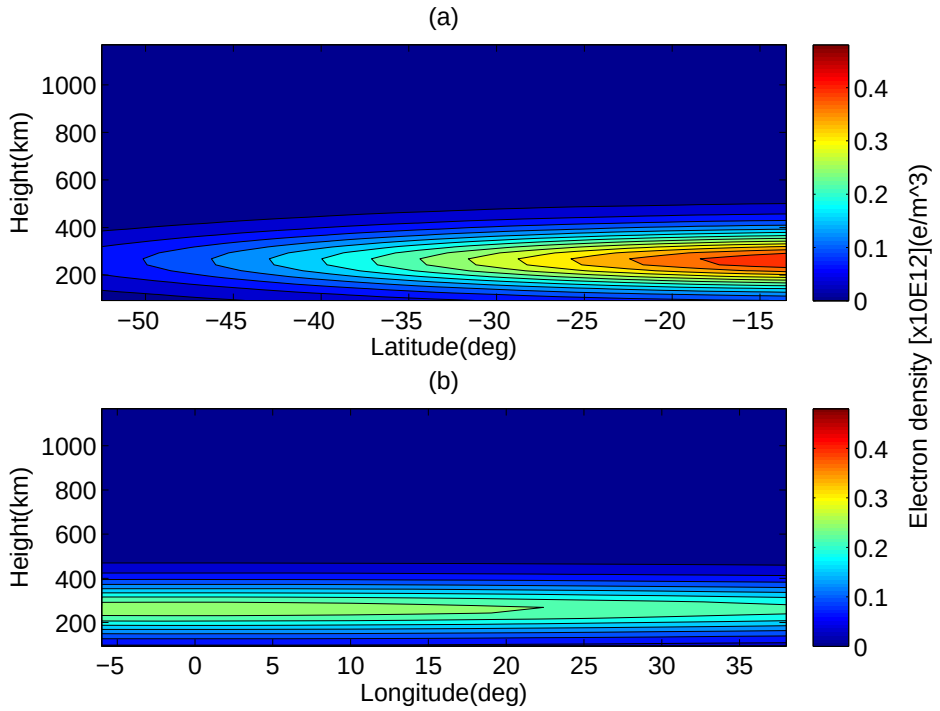

FIGURE 4.28: CTWN 2-D electron density distribution for the period 16:00 - 17:00 UT on 2010-05-19 (day of year 139): (a) North-South plane at 14° longitude. (b) East-West plane at −33.5° latitude.

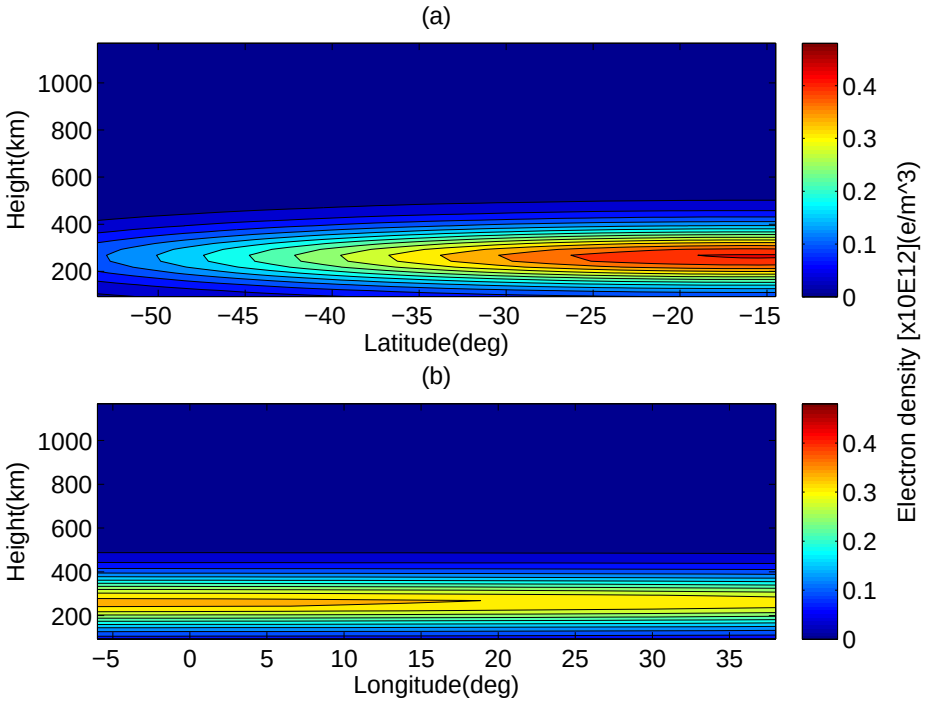

FIGURE 4.29: AGHL 2-D electron density distribution for the period 16:00 - 17:00 UT on 2010-05-19 (day of year 139): (a) North-South plane at 14° longitude. (b) East-West plane at −33.5° latitude.

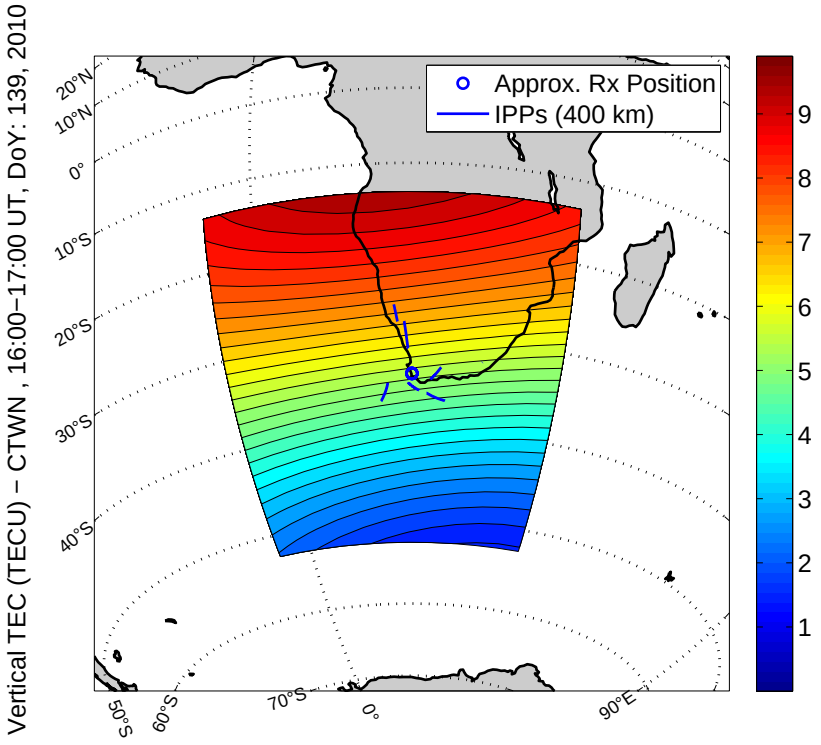

FIGURE 4.30: CTWN vertical TEC map for the period 16:00 - 17:00 UT on 2010-05-19 (day of year 139).

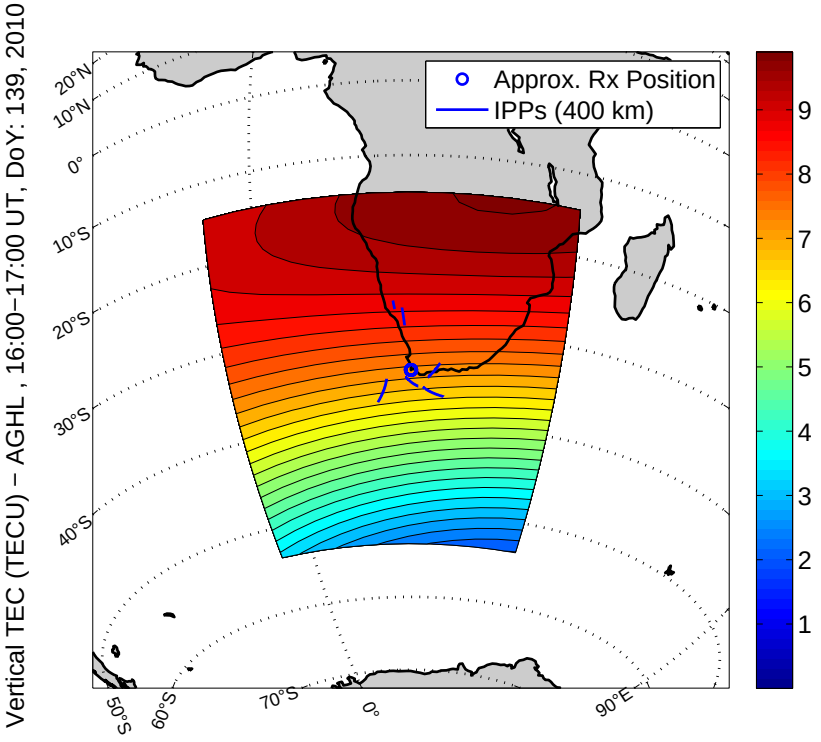

FIGURE 4.31: AGHL vertical TEC map for the period 16:00 - 17:00 UT on 2010-05-19 (day of year 139).

There is a good correlation between the electron density distributions of the CTWN and AGHL receivers in Fig. 4.28 and Fig. 4.29, although differences in the longitudinal gradient are clearly visible. The VTEC comparison in Figs. 4.30 and 4.31 also show a good correlation, although differences in gradient at lower latitudes are clearly visible. There may be several reasons for the difference in the electron density gradient - one being that the calculated TEC values are not definite and can differ by a constant bias offset caused by the MIDAS bias estimation process (Section 4.2.1). Another reason may be the slight difference in satellite visibility and number of STEC values available. The regions with the most visible difference are far away from the IPP's shown. At the time of inversion, the AGHL receiver was approximately 176 km from the CTWN receiver and this may also have caused the slight differences in electron density. The RMSD was 0.0058×10^{12} $\frac{\mathrm{e}}{\mathrm{m}^3}$, which is small compared to the maximum electron density value for the inversion of 0.4341×10^{12} $\frac{\mathrm{e}}{\mathrm{m}^3}$ - which is equal to 1.34 % of the maximum electron density. In Section 3.1.1 such small RMSD values were not considered indicative of the accuracy of the inversion. However, in this case, this value is not compared to other RMSD values and does give a useful indication of the magnitude of the difference. In conclusion, a good correlation exists between the electron density maps generated from the mobile AGHL GPS receiver observables and profiles generated from the CTWN static GPS receiver observables.

4.4.2.2 Case study 2: Gough Island (GOGH)

On 2009-09-16 (day of year 259) the SA Agulhas was close to Gough Island during its annual relief voyage. Considering the aspects important for selecting a suitable period (see Section 4.4.1) into account, the period 12:00 - 13:00 UT on 2009-09-16 (day of year 259) was chosen. Fig. 4.32 shows the ship's position during this period.

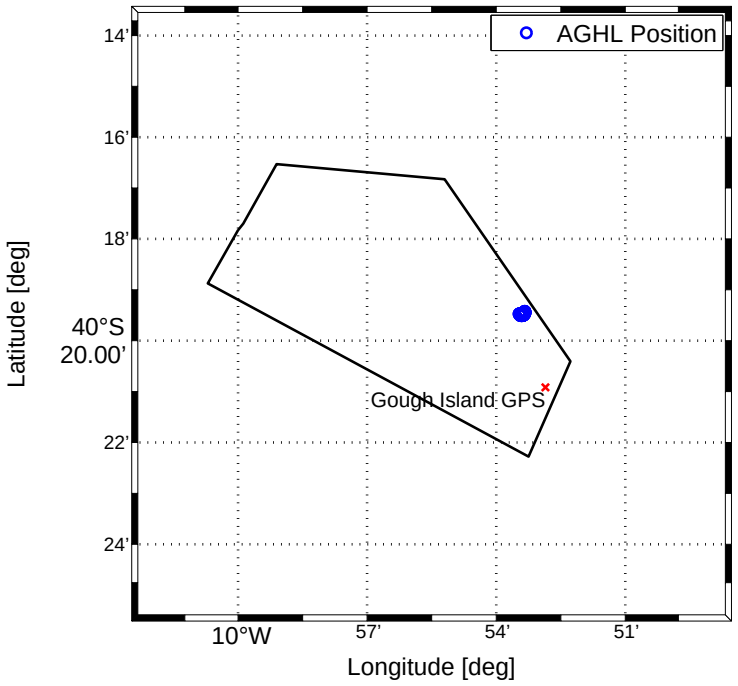

FIGURE 4.32: SA Agulhas position for the period 12:00 - 13:00 UT on 2009-09-16 (day of year 259). Due to the resolution of the map, it seems that the SA Agulhas was on the island. However, it was close to the shore of the island.

Table 4.13 shows the settings used for the data quality processing and MIDAS inversion. Data preprocessing was performed on the AGHL and GOGH data, as discussed in sections 4.1 and 4.2.1.

TABLE 4.13: Settings for the AGHL-GOGH receiver comparison for the period 12:00 - 13:00 UT on 2009-09-16 (day of year 259).

Settings for AGHL-GOGH comparison	
Data and quality control settings	
GOGH	
No. of ray paths removed (elevation angle THR)	81
No. of satellites	8
No. of epochs used	794
AGHL	
No. of ray paths removed (elevation angle THR)	0
No. of satellites	6
No. of epochs used	628
MIDAS inversion settings	
Distance cutoff	Elev. angle
Distance cutoff parameter	$\frac{2}{3}$(GridMax) km
EOF peak height	**EOF scale height**
GOGH	
230 km (IRI2007)	100 km (IRI2007)
AGHL	
230 km (IRI2007)	100 km (IRI2007)

Table 4.14 provides statistics for the difference between slant TEC values from satellites seen by both the AGHL and GOGH GPS receivers. The values shown agree with bias estimation variation values in the literature, as discussed in Section 4.2.1. However, the maximum bias difference is larger than the maximum difference in the comparison with the CTWN receiver and may cause larger differences in the electron density maps.

TABLE 4.14: Statistics of slant TEC differences: AGHL-GOGH comparison.

Mean	2.8 $TECU$
Maximum	5.3 $TECU$
Minimum	1.4 $TECU$

Figs. 4.33 to 4.36 show the plots of electron density distributions and vertical total electron content for the GOGH and AGHL receivers respectively. The RMSD calculated for the AGHL and GOGH electron density maps was 0.037×10^{12} $\frac{\text{e}}{\text{m}^3}$ (see Section 4.4.1.1).

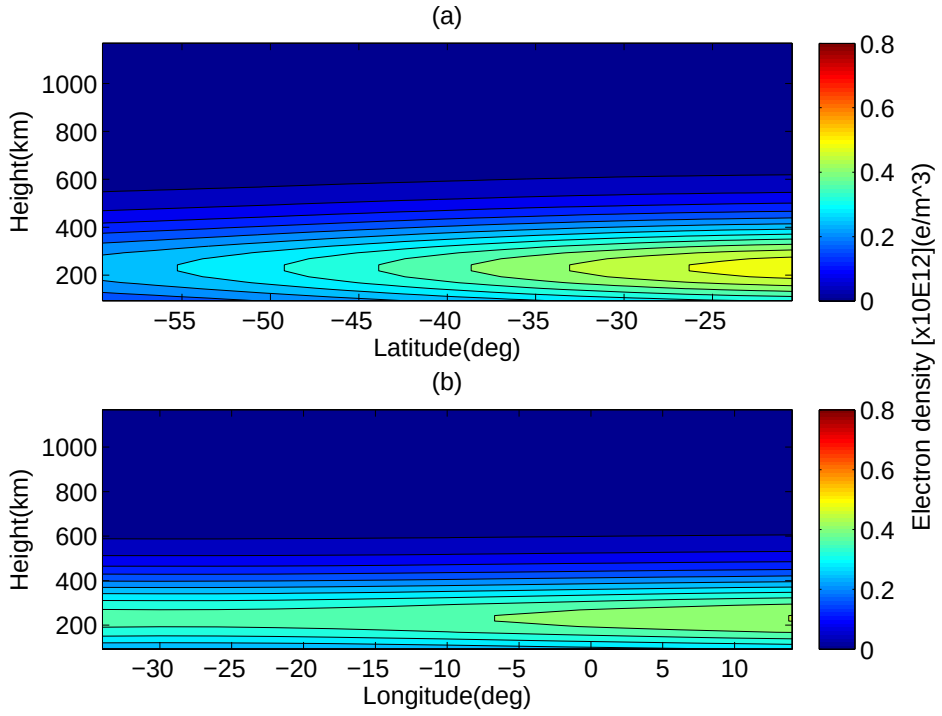

FIGURE 4.33: GOGH 2-D electron density distribution for the period 12:00 - 13:00 UT on 2009-09-16 (day of year 259): (a) North-South plane at −14° longitude. (b) East-West plane at −40.5° latitude.

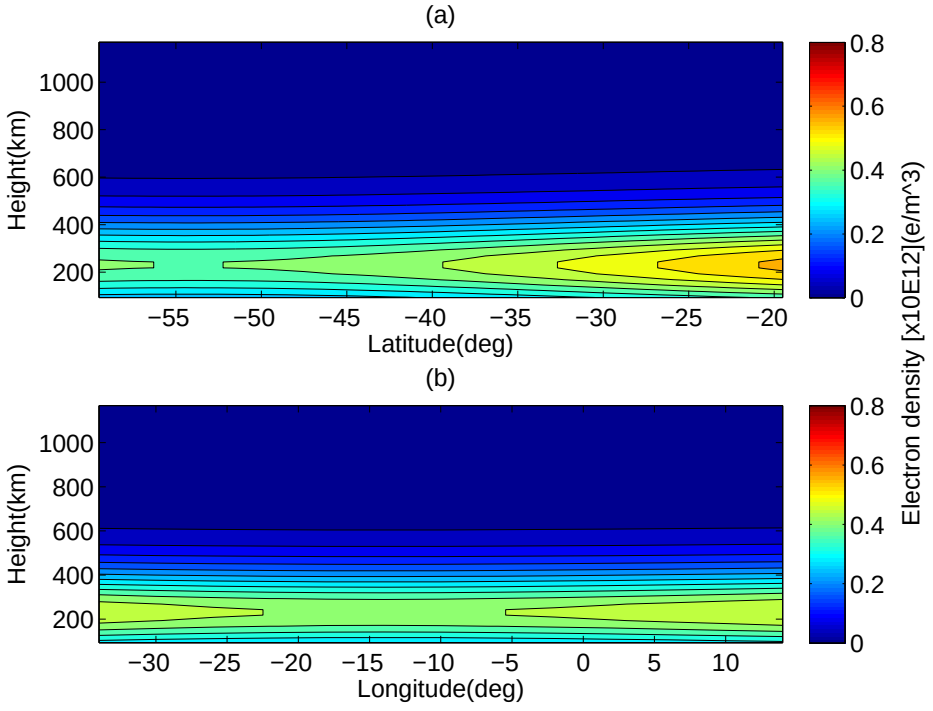

FIGURE 4.34: AGHL 2-D electron density distribution for the period 12:00 - 13:00 UT on 2009-09-16 (day of year 259): (a) North-South plane at −14° longitude. (b) East-West plane at −40.5° latitude.

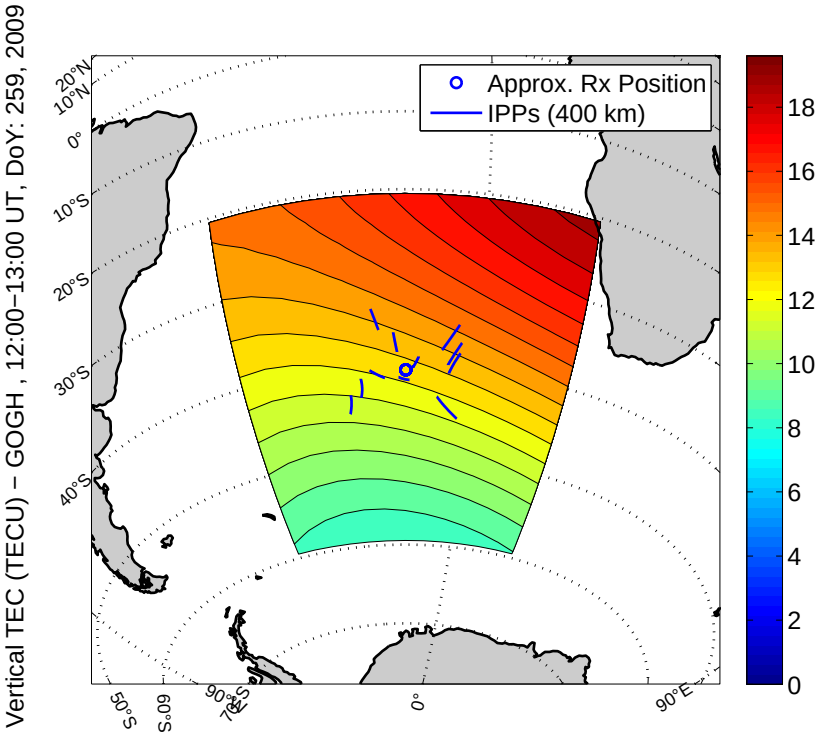

FIGURE 4.35: GOGH vertical TEC map for the period 12:00 - 13:00 UT on 2009-09-16 (day of year 259).

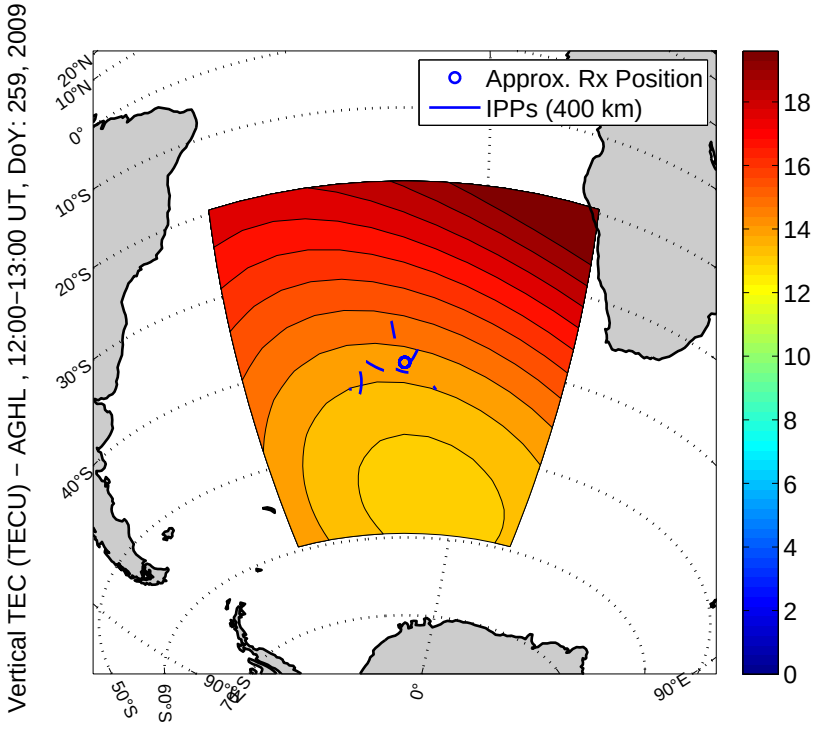

FIGURE 4.36: AGHL vertical TEC map for the period 12:00 - 13:00 UT on 2009-09-16 (day of year 259).

There is a good correlation between the electron distributions for the CTWN and GOGH receivers in Figs. 4.33 and 4.34. The VTEC comparisons shown in Figs. 4.35 and 4.36, however, shows large differences in gradient as the distance from the receivers increase. Fig. 4.35 and Fig. 4.36 clearly indicate that the GOGH receiver has more IPP's (and as a result, STEC values) for higher latitudes than the AGHL receiver. This is probably one of the main contributors to the differences in the vertical electron content maps. At lower latitudes, the IPP's seem similar and a better correlation is achieved. Additionally, bias estimation differences may cause differences in the distribution. The RMSD was 0.037×10^{12} $\frac{\text{e}}{\text{m}^3}$, which is small compared to the maximum electron density value in the inversion of 0.6427×10^{12} $\frac{\text{e}}{\text{m}^3}$ - which is equal to 5.76 % of the maximum electron density. This is considerably larger than the RMSD value of 0.0058×10^{12} $\frac{\text{e}}{\text{m}^3}$ calculated for the AGHL-CTWN comparison and shows the importance of using GPS observables with the same coverage. In conclusion, a correlation exists between the electron density maps generated from the mobile GPS receiver observables and those generated from the GOGH static GPS receiver observables. The decrease in correlation compared to the AGHL-CTWN analysis (Section 4.4.2.1) can be attributed to the larger bias differences between the VTEC values and to the differences in STEC observations available.

4.4.3 Conclusion

The two case studies presented here clearly show that there is a strong similarity between slant TEC and resulting electron density maps generated from the network of known and trusted static dual-frequency GPS receivers and similar receivers installed on a mobile platform. Quantitatively, the RMSD calculated for the AGHL-CTWN receiver comparison was 0.0058×10^{12} $\frac{\text{e}}{\text{m}^3}$, which is equal to 1.34 % of the maximum electron density. The RMSD calculated for the AGHL-GOGH receiver comparison was 0.037×10^{12} $\frac{\text{e}}{\text{m}^3}$, which is equal to 5.76 % of the maximum electron density. However, it cannot be argued that the electron density profiles are indeed correct. It can only be stated that the data is indeed *similar* to a known measurement technique currently employed.

Futhermore, GPS data from a mobile platform is significantly different from that of a static receiver. Some of these differences can be reduced to a certain degree by preprocessing. However, more research is needed to determine the cause of and a solution for

these differences, especially bias estimation differences.

In conclusion, a good correlation exists between the electron density maps generated from the mobile AGHL GPS receiver observables and those generated from the static GPS receiver observables.

4.5 HF PROPAGATION PATH PREDICTION

High frequency propagation path prediction is defined as the process which, based on the atmospheric conditions, predicts where a high frequency wave transmitted from an antenna will reach a point on the Earth's surface. Several methods are used to perform this prediction: VOACAP-based (Voice of America Coverage Analysis Program for HF Propagation Prediction and Ionospheric Communications Analysis) algorithms, MUF-based algorithms, and many more. A custom-made algorithm was used to perform high frequency propagation path predictions. The technique divides the ionosphere vertically into Multiple Quasi-Parabolic Segments (MQPS) and horizontally into sectors using the Segmented Method for Analytical Ray-Tracing (SMART). However, to predict the ray path, an electron density map of the ionosphere is needed. Currently, the International Reference Ionosphere is widely used as input for the HF propagation path algorithms. Ionospheric tomography, however, poses an alternative to the IRI model. Using a mobile GPS receiver, ionospheric tomography can provide electron density maps over the oceans where land-based methods such as ionosondes cannot be used. To investigate the viability of using electron density maps generated by ionospheric tomography based on a mobile dual-frequency GPS receiver's observations, a comparison was made of HF path predictions based on the IRI2007 model and HF path predictions based on the electron density maps generated by MIDAS from the SA Agulhas GPS observables. These predictions were compared to known HF signal paths obtained from the Norther California DX Foundation (NCDXF/IARU) HF Beacon Project.

4.5.1 Method

A comparison was made between HF path predictions based on the IRI2007 model and the electron density maps generated by MIDAS from the SA Agulhas GPS observables. To verify the maps, data from the network of NCDXF/IARU HF beacons were used. The network has 18 transmitter stations and approximately 40 monitoring stations. Each transmitter transmits a signal on five different frequencies according to a schedule. The frequencies used are 14.1 MHz, 18.110 MHz, 21.150 MHz, 24.930 MHz and 28.200 MHz. This signal is received by the monitoring stations and identified by a unique call sign. Each receiver can discern from which transmitter a signal originates and whether a signal has been received - this means that the ionospheric conditions

between these stations are favourable. Each beacon transmits a signal every three minutes. Fig. 4.37 shows the locations of all the transmitters around the globe and the black circle indicates the area of operation of the SA Agulhas research vessel.

FIGURE 4.37: Locations of the NCDXF/IARU HF beacons. The black circle indicated the operating region of the SA Agulhas research vessel. Taken from the NCDXF HF Beacon Project web site, with permission.

GPS observables were obtained from the SA Agulhas research vessel during 2009 and 2010 on several of its voyages to Marion Island, Gough Island and Antarctica. These observables were used for the inversion and the resulting electron density maps were used as input for the HF path prediction algorithm. To determine whether the electron density maps generated by the inversions are accurate enough for HF path prediction, the HF beacon receiver signal strength and the path prediction results must agree. Fig. 4.38 shows an example of the HF beacon receiver signal strength of the ZS1HMO station in Hermanus, South Africa. Transmitting and monitoring stations which can possibly be used for verification within the operating region of the SA Agulhas research vessel include:

- LU4AA - Beacon. Buenos Aires, Argentina. Location: 34.61666°S, 58.35°W
- ZS6DN - Beacon. Pretoria, South Africa. Location: 25.9050°S, 28.26440°E
- VK6RBP - Beacon. Rolystone, Australia. Location: 32.1°S, 116.05°E
- Antarctica - Monitoring. King George Island, Antarctica. Location: 62.0743°S, 58.4061°W

(a)

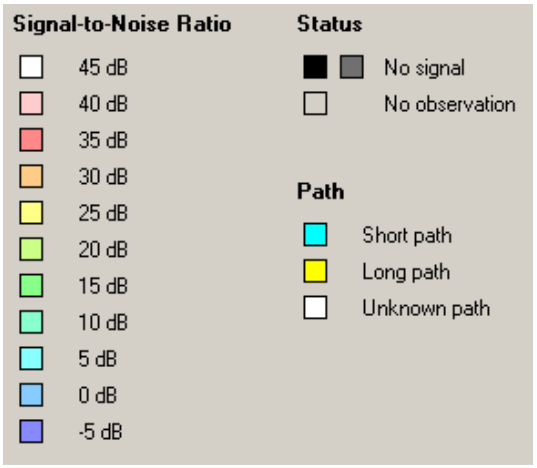

(b)

FIGURE 4.38: Results from the HF Beacon network: (a) ZS1HMO received signal strength, (b) Signal graph legend [27].

- ZS1HMO - Monitoring. Hermanus Magnetic Observatory, South Africa. Location: 19.22472°S, 34.42416°W

However, in choosing a suitable HF propagation path, the following aspects had to be taken into consideration.

- The accuracy of the MIDAS inversion decreases as the distance from the GPS receiver increases. Thus, the profile on which the HF propagation path is based must be as close to the mobile GPS receiver as possible.

- This study hopes to determine the viability of a *network* of mobile GPS receivers but currently only a single receiver's GPS observables are used, which limits the resolution and the geographical range of the inversion.

For instance, the propagation path between the LU4AA beacon and the ZS1HMO station was considered, but since only one mobile GPS receiver is currently available, the range of the inversion becomes large and the resulting electron density map may be inaccurate in the areas far from the receiver. Thus, the propagation path between the ZS6DN transmitting station and ZS1HMO monitoring station was used for the comparison. The SA Agulhas research vessel passes close by the ZS1HMO receiver on its voyages to and from Marion Island. For the IRI2007 comparison, 3-D electron density maps were generated using the IRI2007 model.

To perform the analysis, the raw GPS observables were preprocessed by means of the mobile GPS toolbox and used as input for the MIDAS inversion. The data quality criteria are specified in Section 4.2.3, with any unique values specified at each inversion. One EOF was generated based on the IRI2007 model (as explained in Section 4.2.2) at 12:00 UT on the day of interest. One variable worth noting is the distance from the receiver for which the inversion is being performed. For the purpose of HF propagation path prediction, a profile is needed that reaches both transmitter and receiver. The user-specified radius of the inversion was dtermined so that both the ZS1HMO receiver and the ZS6DN transmitter are covered. The electron density maps generated by MIDAS were in turn used as input for the HF path prediction algorithm. Since the locations of both the transmitter and receiver is known, the HF propagation algorithm effectively used only a 2-D slice (electron density distribution) from the electron density map to perform the prediction.

The HF path prediction algorithm has its own number of settings, including the elevation angle at which the transmitter transmits the signal. This variable is discussed briefly for the ZS6DN beacon.

ZS6DN elevation angle

One of the most important and influential factors in the HF ray prediction algorithm, is the elevation angle at which the transmitter transmits the HF signal. Theoretically speaking, if the ionosphere is in a favourable state for signal reflection, an HF signal

will always be traceable to a certain point on the ground if there are no constraints on the elevation angle (a change in the elevation angle will cause the landing point to shift). This will most likely lead to false results. To make provision for this problem, the radiation pattern of the transmitter (ZS6DN) has to be characterised to determine at which angle the signal will most likely reach the receiver. Although a weaker transmitter signal may reach the receiver, the probability that a signal transmitted at an elevation angle with the most power may reach the receiver, is much greater. The antenna installed at ZS6DN is a broadband vertical HF antenna. The generalised vertical radiation pattern for 14 MHz transmission is shown in Fig. 4.39.

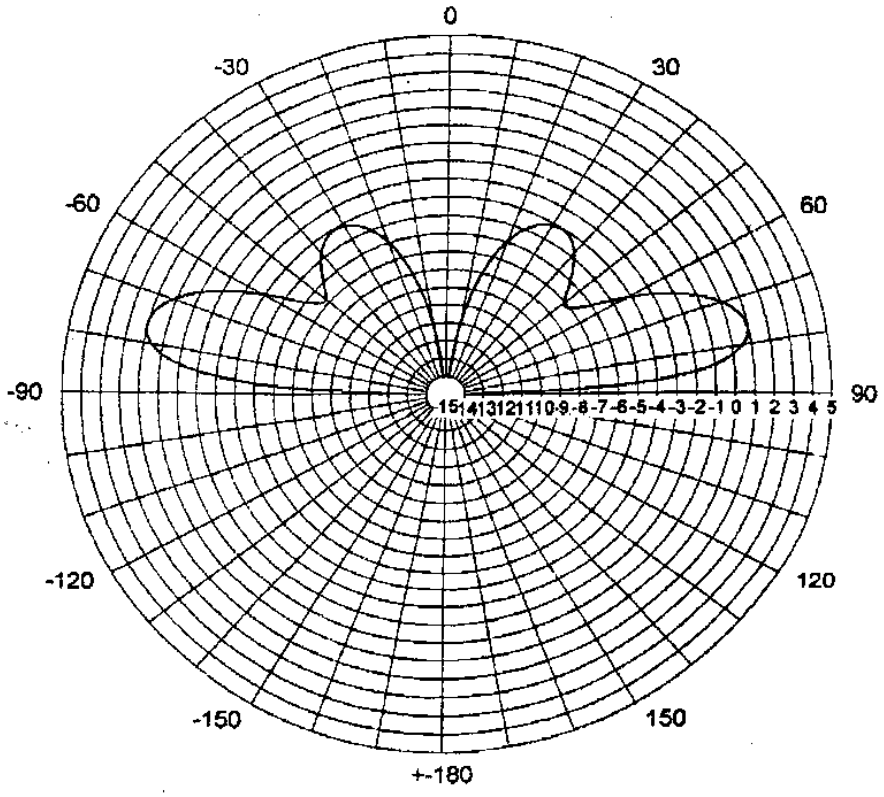

FIGURE 4.39: Generalised radiation pattern for a broadband HF vertical antenna transmitting at 14 MHz [28].

If the transmission angle of a transmitter transmitting at peak power is isolated, the elevation angle varies between 13° and 17° (Fig. 4.39). This is the elevation angle sweep range that was used in the analysis. An elevation angle sweep with an increment of one degree was performed.

Fig. 4.40 shows an example of an HF path prediction for 12:00 UT on 2010-04-08 (day of year 98).

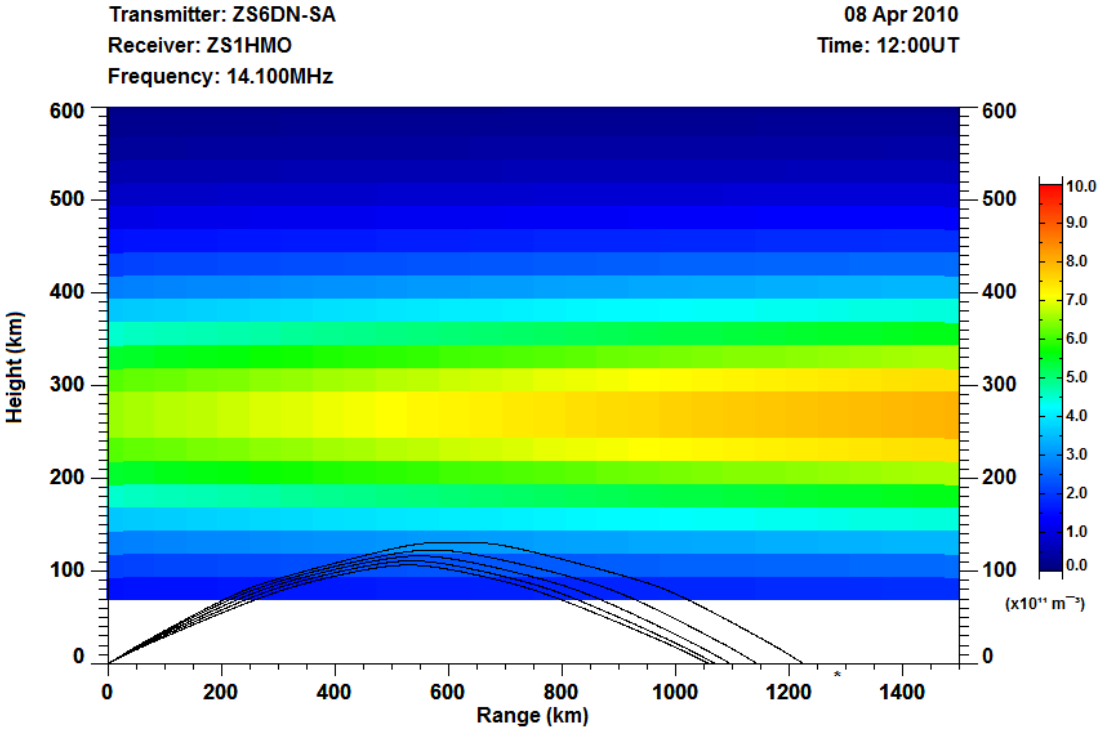

FIGURE 4.40: HF path prediction using the SA Agulhas mobile GPS receiver-generated electron density map for 12:00 UT on 2010-04-08 (day of year 98).

4.5.1.1 Performance analysis

To test the viability of using electron density maps generated from the mobile GPS receiver observables, periods that the receiver (ZS1HMO) received a signal from the transmitter (ZS6DN) must agree with HF ray path predictions. In other words, if a signal was received by the receiver, the HF ray path prediction algorithm should show that the ray path should most likely reach a point close to the receiver. However, when using HF ray path prediction as verification, many unknowns and assumptions of high-frequency propagation theory and the prediction algorithm are introduced into the analysis. To make provision these uncertainties, the signal was considered to have reached the receiver if it reached the ground within a radius of 150 km from the receiver location. This test was conducted for the electron density maps generated by both the IRI2007 model and the those generated by MIDAS from mobile GPS observables. These results were compared, and since the IRI is currently used for HF path prediction, this comparison should provide a fair measure of the viability of using electron density maps generated from the mobile GPS receiver observables. A correlation was made between the signal-to-noise ratio (SNR) at the receiver and whether the

predicted ray reached the ground within a radius of 150 km from the receiver location. This was to determine whether the ray path prediction is only accurate with high SNR values.

Since the power of the received signal is indicated on the receiver graph (Fig. 4.38) a correlation analysis was done of the distance between the point where the ray path prediction reaches ground level and the receiver, and the power SNR received by the monitoring station. Where the ray path predictions did not reach the ground, a value of 2 000 km was assigned for the purpose of the correlation analysis. The significance of assigning a value will become clear when results are discussed. Since the power levels are given in 15-minute intervals, the power SNR was averaged over four 15-minute intervals to obtain an estimate for an hour. Ideally, this correlation coefficient should be negative, because as the distance to the receiver decreases, the signal strength should increase.

In conclusion, five analyses were performed.

1. Receiver SNR (1 - larger than 0, 0 - zero) correlated with the predicted ray path reaching the ground within a radius of 150 km from the receiver (1 - Yes, 0 - No). [Qualitative]

2. Normalised receiver SNR correlated with the predicted ray path reaching the ground within a radius of 150 km from the receiver (1 - Yes, 0 - No). [Qualitative]

3. Percentage of correct ray path predictions agreeing with the receiver SNR (zero and non-zero SNR). [Quantitative]

4. Percentage of correct ray path predictions agreeing with periods that the receiver received a signal with a SNR larger than zero (only non-zero SNR). [Quantitative]

5. Correlation between the normalised received SNR and the normalised distance from the receiver where the predicted ray path reaches the ground. [Quantitative]

4.5.2 Results

4.5.2.1 Case study 1: ZS6DN-ZS1HMO for 2010-02-22 (day of year 53)

The following results were obtained for 2010-02-22 (day of year 53) when the SA Agulhas was on its inbound voyage from the SANAE base in Antarctica. The procedure is outlined in sections 4.2 and 4.5.1. Fig. 4.41 shows the ship's position for this day as well as the positions of the transmitter and receiver.

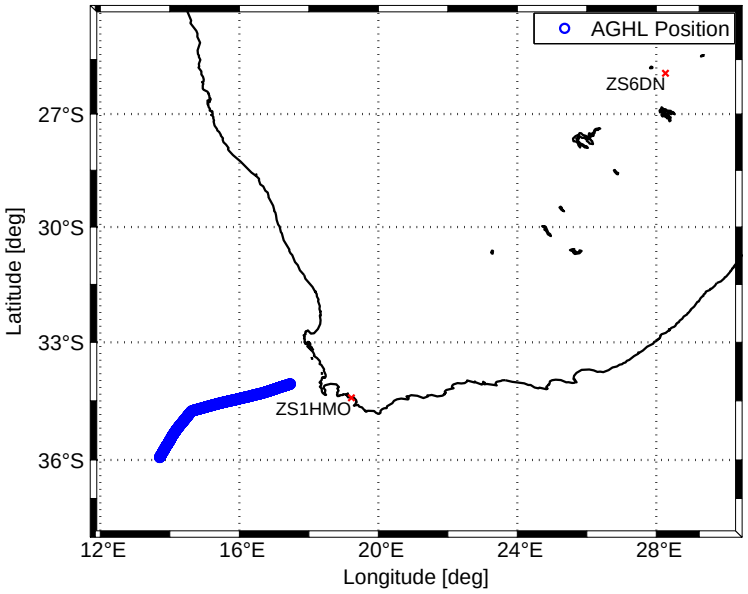

FIGURE 4.41: Position of the SA Agulhas research vessel on 2010-02-22 (day of year 53) and the positions of the ZS6DN transmitter and ZS1HMO receiver.

Table 4.15 presents the data quality criteria and MIDAS inversion settings used for the analysis.

TABLE 4.15: Data quality criteria and MIDAS inversion settings for the HF path prediction for 2010-02-22 (day of year 53).

Settings for 2010-02-22 (day of year 53).			
MIDAS inversion settings			
Distance cutoff	User	Distance cutoff parameter	2000 km
EOF peak height		**EOF scale height**	
295 km (IRI2007)		80 km (IRI2007)	

Table 4.16 lists results of the analysis for 2010-02-22 (day of year 53).

TABLE 4.16: Results of the ZS6DN-ZS1HMO HF propagation path prediction for 2010-02-22 (day of year 53). Hours that are not listed did not have adequate GPS observables available for the analysis.

Time (UT)	Distance from Rx (km)		Within 150 km		Av. P ($\frac{dB}{hour}$)
	AGHL	IRI2007	AGHL	IRI2007	
0	—	—	N	N	0
1	—	—	N	N	0
2	—	—	N	N	0
3	—	—	N	N	0
4	—	—	N	N	0
6	—	615	N	N	0
9	29	509	Y	N	27.5
10	60	553	Y	N	17.5
12	110	534	Y	N	27.5
16	115	533	Y	N	23.75
17	168	—	N	N	10
18	1875	—	N	N	3.75
19	583	—	N	N	0
22	—	—	N	N	23.75

Fig. 4.42 compares the HF path prediction algorithm results based on the IRI and AGHL electron density maps for performance analysis criteria one and two (Section 4.5.1.1). Table 4.17 lists the quantitative results obtained for performance analysis parameters three and four (Section 4.5.1.1).

TABLE 4.17: Quantitative results of the HF path prediction for 2010-02-22 (day of year 53).

Quantitative results for 2010-02-22 (day of year 53)		
	IRI2007	AGHL
Percentage of correct ray predictions (zero and non-zero)	50 %	83.3 %
Percentage of correct ray predictions (non-zero)	0 %	57.14 %

Due to the sparsity of the STEC data set, the relation between the normalised distance of the ray from the receiver (HF propagation algorithm) and the normalised receiver SNR was not investigated (performance analysis criterion five).

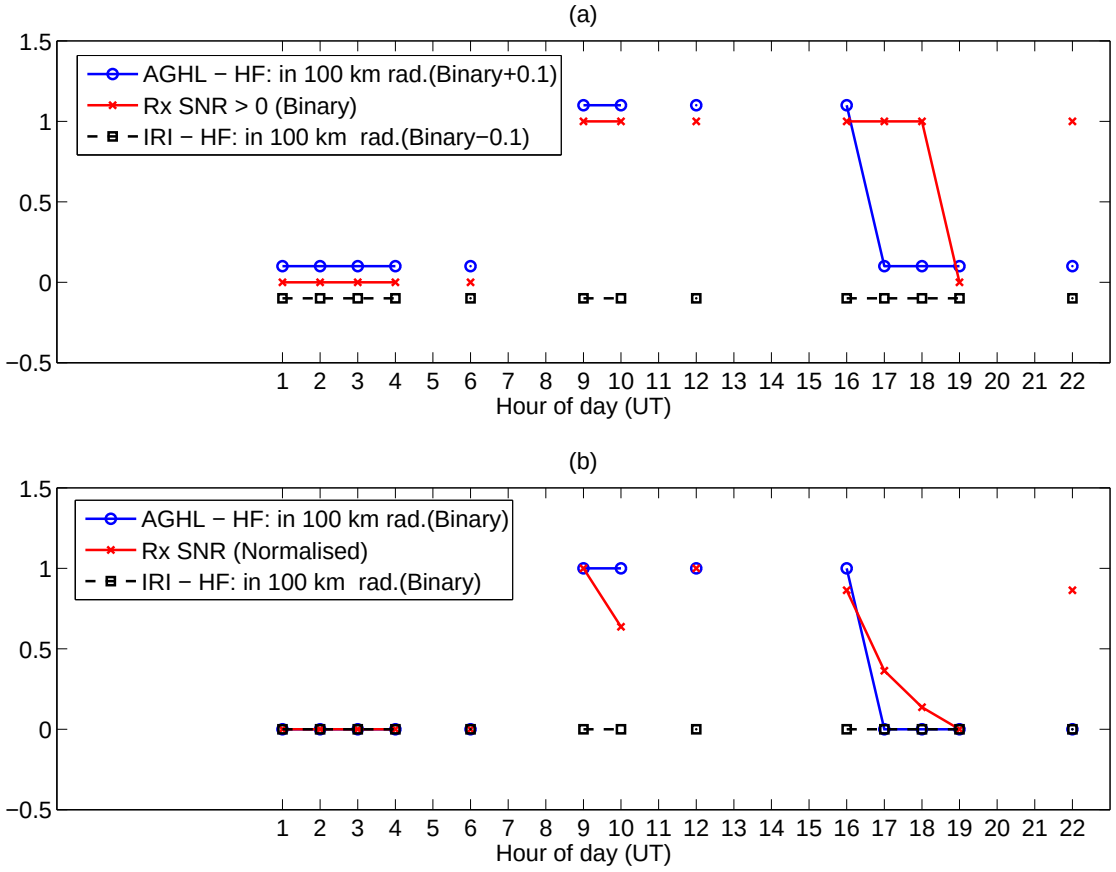

FIGURE 4.42: Comparison of HF path prediction results obtained with the IRI2007 model and with the tomographic inversion of the mobile GPS observables for 2010-02-22 (day of year 53): (a) Receiver SNR (1 - larger than 0, 0 - zero) correlated with the predicted ray path reaching the ground within a radius of 150 km from the receiver(1 - Yes, 0 - No). An offset was added to the binary values to make the results clearer. (b) Normalised receiver SNR correlated with the predicted ray path reaching the ground within a radius of 150 km from the receiver(1 - Yes, 0 - No).

Fig. 4.42(a) clearly shows that the electron density map generated from mobile GPS observables has a better correlation with the SNR at the ZS1HMO receiver than the map based on the IRI2007 model. Fig. 4.42(b) seems to suggest that the higher SNR values received by the ZS1HMO station agree with the HF path propagation results derived from the mobile GPS receiver observables. However, as expected from the results in 4.42(a), the IRI2007 model HF predictions show no relation to the SNR. Furthermore, the figures in Table 4.17 clearly demonstrate that the results obtained by using the mobile GPS observables are better than the results obtained by using the IRI2007 model.

4.5.2.2 Case study 2: ZS6DN-ZS1HMO - 2010-04-08 (day of year 98)

The following results were obtained for 2010-04-08 (day of year 98) when the SA Agulhas was on its return voyage from Marion Island. The procedure is outlined in sections 4.2 and 4.5.1. Fig. 4.43 shows the ship's position for this day as well as the positions of the transmitter and receiver.

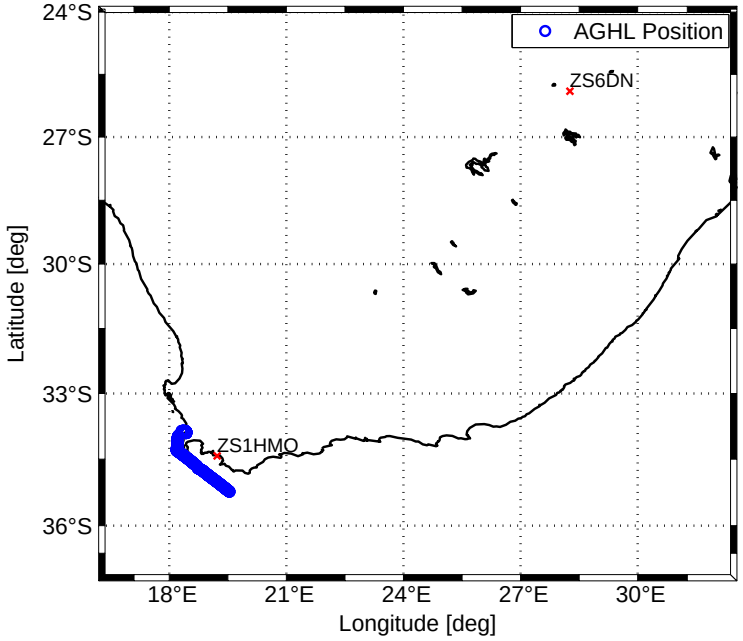

FIGURE 4.43: Position of the SA Agulhas research vessel on 2010-04-08 (day of year 98) and the positions of the ZS6DN transmitter and ZS1HMO receiver.

Table 4.18 presents the data quality criteria and MIDAS inversion settings used for the analysis.

TABLE 4.18: Data quality criteria and MIDAS inversion settings for the HF path prediction for 2010-04-08 (day of year 98).

Settings for 2010-04-08 (day of year 98)			
MIDAS inversion settings			
Distance cutoff	*User*	Distance cutoff parameter	2000 km
EOF peak height		**EOF scale height (km)**	
280 (IRI2007)		70 (IRI2007)	

Table 4.19 lists results of the analysis for 2010-04-08 (day of year 98).

TABLE 4.19: Results of the ZS6DN-ZS1HMO HF propagation path prediction on 2010-04-08 (day of year 98). Hours that are not listed did not have adequate GPS observables available to perform the analysis.

Time (UT)	Distance from Rx (km)		Within 150 km		Av. P ($\frac{dB}{hour}$)
	AGHL	IRI2007	AGHL	IRI2007	
11	25	328	Y	N	32.5
12	59	278	Y	N	30
13	186	221	N	N	32.5
14	39	188	Y	N	28.75
15	223	259	N	N	18.75
16	798	664	N	N	0
17	918	—	N	N	0
18	—	—	N	N	0
19	—	—	N	N	0
20	—	—	N	N	0
21	—	—	N	N	0
22	—	—	N	N	0
23	—	—	N	N	0
24	—	—	N	N	0

Fig. 4.44 compares the HF path prediction algorithm results based on the IRI2007 and AGHL electron density maps for performance analysis parameters one and two (Section 4.5.1). Fig. 4.45 shows the relation between the normalised distance of the ray from the receiver (HF propagation algorithm) and the normalised receiver SNR at the receiver. Table 4.20 lists the quantitative results for performance analysis parameters three and four (Section 4.5.1).

TABLE 4.20: Quantitative results of the HF path prediction for 2010-04-08 (day of year 98).

Quantitative results for 2010-04-08 (day of year 98)		
	IRI2007	**AGHL**
Percentage of correct ray predictions (zero and non-zero)	61.54 %	84.16 %
Percentage of correct ray predictions (non-zero)	0 %	60 %
Correlation (SNR and distance from Rx)	-0.89	-0.88

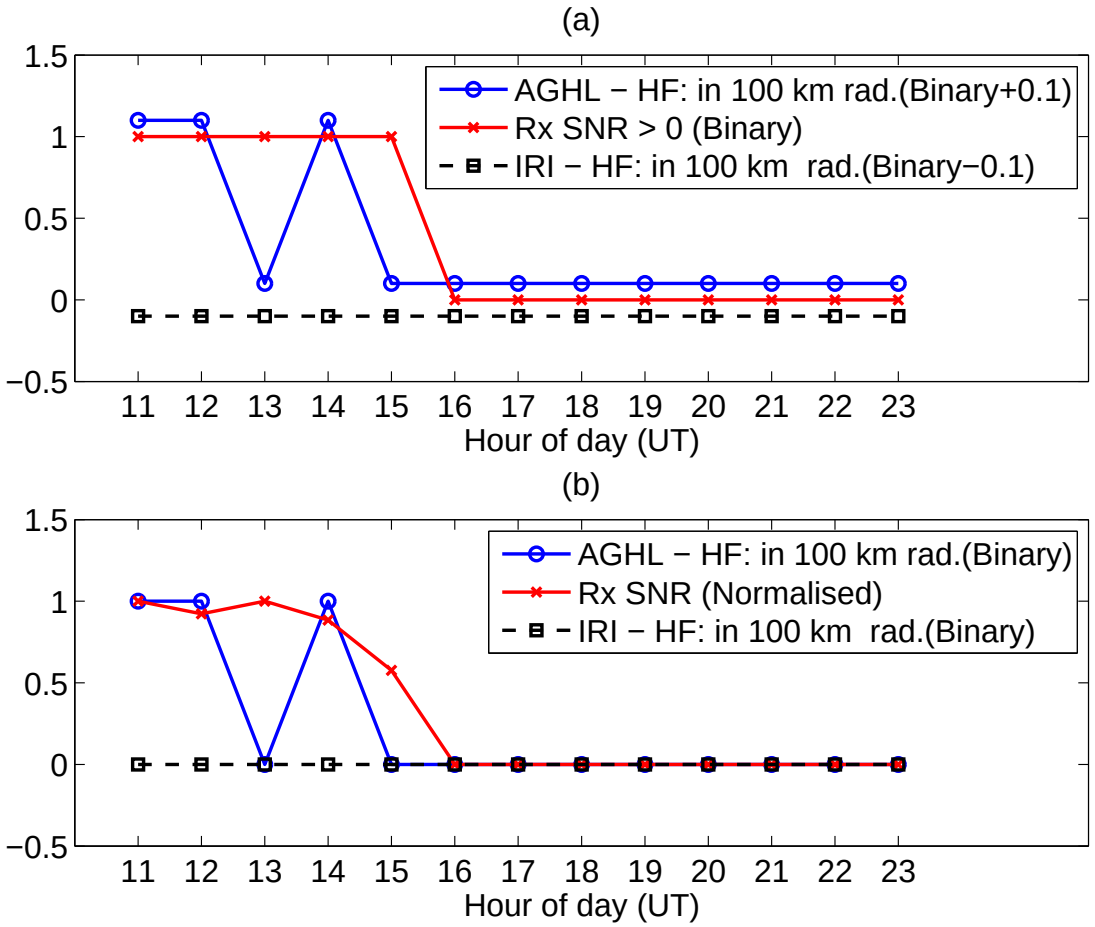

FIGURE 4.44: Comparison of HF path prediction results obtained with the IRI2007 model and with the tomographic inversion of the mobile GPS observables for 2010-04-08 (day of year 98): (a) Receiver SNR (1 - larger than 0, 0 - zero) correlated with the predicted ray path reaching the ground within a radius of 150 km from the receiver(1 - Yes, 0 - No). An offset was added to the binary values to make the results clearer. (b) Normalised receiver SNR correlated with the predicted ray path reaching the ground within a radius of 150 km from the receiver(1 - Yes, 0 - No).

Fig. 4.44(a) clearly shows that the electron density map generated from mobile GPS observables has a better correlation to the SNR at the ZS1HMO receiver than the map based on the IRI2007 model. Fig. 4.44(b) seems to suggest that the higher SNR values received by the ZS1HMO station agree with the HF path propagation results based on the mobile GPS receiver observables, but there is a mismatch at 13:00 UT. As expected from the results in Fig. 4.44(a), the IRI2007 model HF predictions shows no relation to the SNR. Fig. 4.45 shows a clear relation between the normalised SNR at the receiver and the normalised distance from the receiver to the closest predicted ray path. This confirms the accuracy of the electron density maps generated from the mobile GPS observables. Table 4.20 clearly shows that the results obtained by using

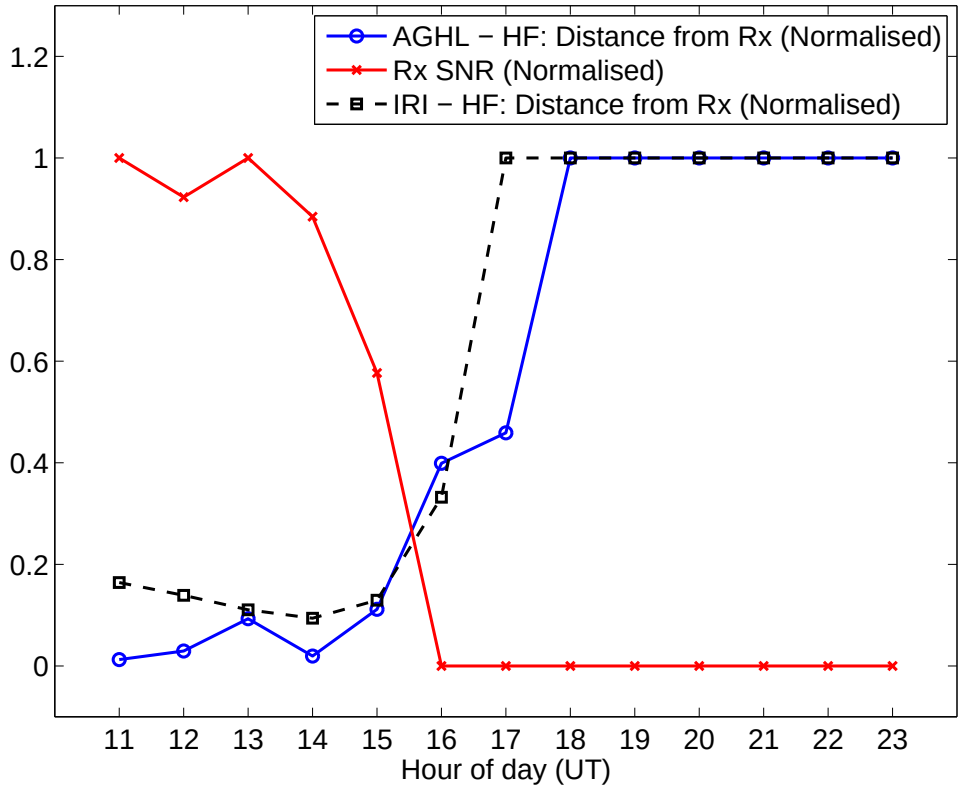

FIGURE 4.45: Comparison of HF path prediction results obtained with the IRI2007 model and with tomographic inversion of the mobile GPS data for 2010-04-08 (day of year 98).

the mobile GPS observables are better than the results obtained using the IRI2007 model - especially when an SNR larger than zero is received at the ZS1HMO station.

4.5.2.3 Case study 3: ZS6DN-ZS1HMO - 2010-05-19 (day of year 139)

The following results were obtained for 2010-05-19 (day of year 139) when the SA Agulhas was on its outbound voyage to Marion Island. The procedure is outlined in sections 4.2 and 4.5.1. Fig. 4.46 shows the ship's position for this day as well as the positions of the transmitter and receiver.

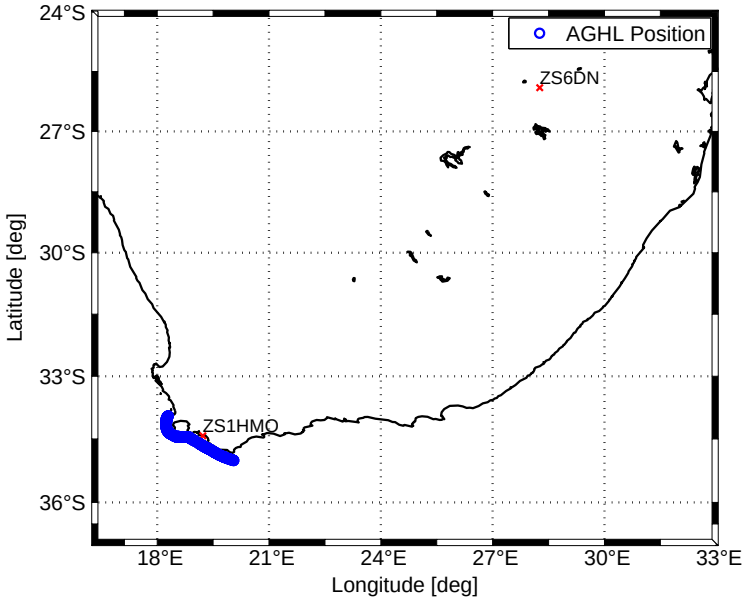

FIGURE 4.46: Position of the SA Agulhas research vessel on 2010-05-19 (day of year 139) and the positions of the ZS6DN transmitter and ZS1HMO receiver.

Table 4.21 presents the data quality criteria and MIDAS inversion settings used for the analysis.

TABLE 4.21: Data quality criteria and MIDAS inversion settings for the HF path prediction for 2010-05-19 (day of year 139).

Settings for 2010-05-19 (day of year 139)			
MIDAS inversion settings			
Distance cutoff	*User*	Distance cutoff parameter	2000 km
EOF peak height		**EOF scale height**	
270 km (IRI2007)		70 km (IRI2007)	

Table 4.22 shows results of the analysis for 2010-05-19 (day of year 139). Fig. 4.47 compares the HF path prediction algorithm results based on the IRI2007 and AGHL electron density maps for performance analysis parameters one and two (Section 4.5.1). Fig. 4.48 shows the relation between the normalised distance of the ray from the receiver (HF propagation algorithm) and the normalised receiver SNR. Table 4.23 lists the quantitative results obtained for performance analysis parameters three and four (Section 4.5.1).

TABLE 4.22: Results of the ZS6DN-ZS1HMO HF propagation path prediction on 2010-05-19 (day of year 139). Hours that are not listed did not have adequate GPS observables available to perform the analysis.

Time (UT)	Dist. from Rx (km)		Within 150 km		Av. P ($\frac{dB}{hour}$)
	AGHL	IRI2007	AGHL	IRI2007	
0	—	—	N	N	0
1	—	—	N	N	0
2	—	—	N	N	0
3	—	—	N	N	0
4	—	—	N	N	0
5	—	—	N	N	0
6	—	719	N	N	0
7	—	166	N	N	3.75
8	—	77	N	Y	16.25
9	1932	97	N	Y	23.75
10	403	148	N	Y	28.75
12	197	192	N	N	22.5
13	558	170	N	N	17.5
14	17	177	Y	N	26.25
15	425	364	N	N	28.75
16	1163	—	N	N	16.25
18	—	—	N	N	0
19	—	—	N	N	0
21	—	—	N	N	0
22	—	—	N	N	0

TABLE 4.23: Quantitative results of the HF path prediction on 2010-05-19 (day of year 139).

Quantitative results for 2010-05-19 (day of year 139)		
	IRI2007	**AGHL**
Percentage of correct ray predictions (zero and non-zero)	70 %	60 %
Percentage of correct ray predictions (non-zero)	33.33 %	11.11 %
Correlation (SNR and distance from Rx)	-0.78	-0.83

Contrary to the previous two analyses, Fig. 4.47(a) shows that the electron density map based on the IRI2007 model has a better correlation SNR at the ZS1HMO receiver than the map based on the mobile GPS observables. Fig. 4.47(b) does not indicate any significant relation between the receiver SNR and whether the ray path falls within 150 km of the receiver. Fig. 4.48 shows the relation between the normalised receiver SNR and the distance from the receiver to the closest predicted ray path for both the IRI2007 and the mobile GPS based electron density maps, and a stronger correlation is seen between the results based on the mobile GPS observables than those based on

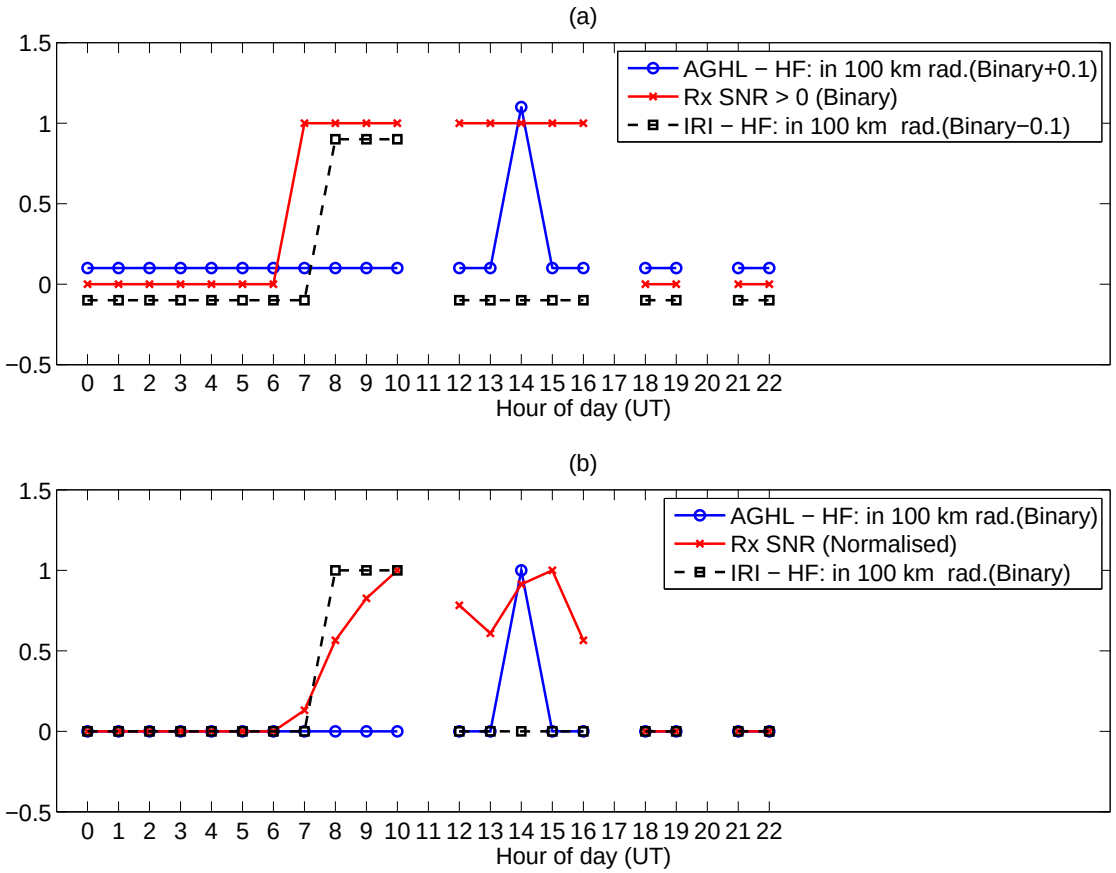

FIGURE 4.47: Comparison of HF path prediction results obtained with the IRI2007 model and with the tomographic inversion of the mobile GPS observables for 2010-05-19 (day of year 139): (a) Receiver SNR (1 - larger than 0, 0 - zero) compared with the predicted ray path reaching the ground within a radius of 150 km from the receiver(1 - Yes, 0 - No). An offset was added to the binary values to make the results clearer. (b) Normalised receiver SNR compared with the predicted ray path predictions reaching the ground within a radius of 150 km from the receiver(1 - Yes, 0 - No).

the IRI2007 model. These results are also confirmed by the correlation between the SNR and the distance from the receiver shown in Table 4.23. The results in Table 4.23 show better performance of the results based on the IRI2007 model than those based on the mobile GPS observables.

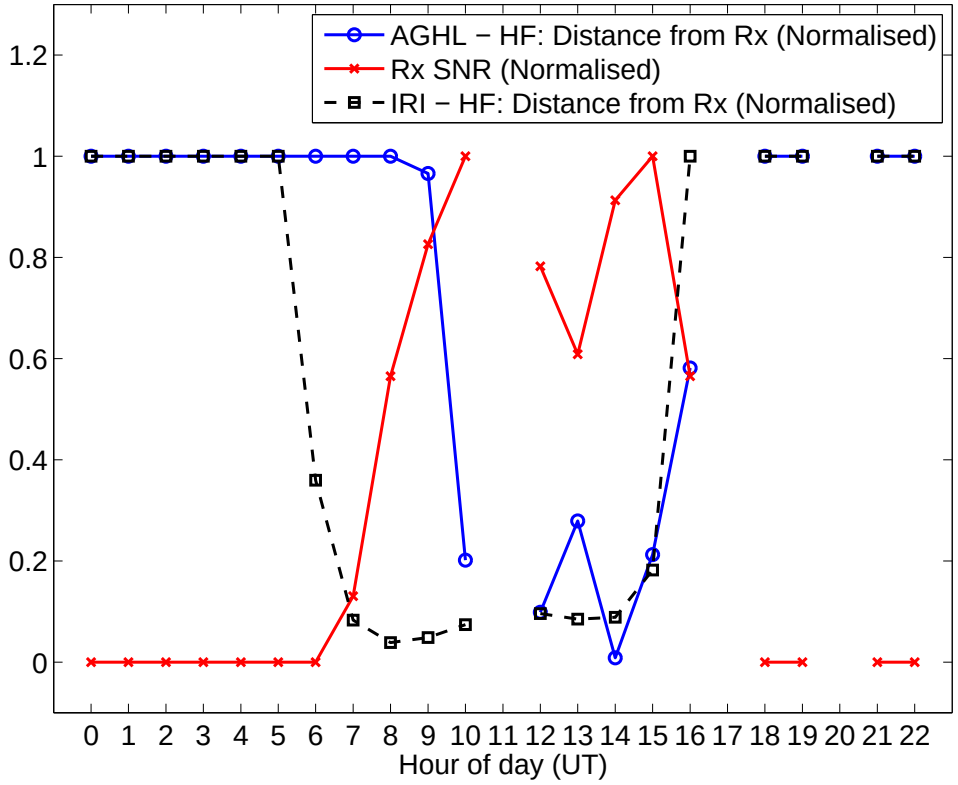

FIGURE 4.48: Comparison of HF path prediction results obtained with the IRI2007 model and with the tomographic inversion of the mobile GPS observables for 2010-05-19 (day of year 139).

4.5.3 Conclusion

Table 4.24 shows a summary of the mean values for the three case studies performed for the HF propagation path prediction analysis. It is clear that if all three case studies

TABLE 4.24: Summary of quantitative results for the HF path prediction analysis.

Summary of quantitative results		
	IRI2007	**AGHL**
Mean percentage of correct ray predictions (zero and non-zero)	60.51 %	75.82 %
Mean percentage of correct ray predictions (non-zero)	11.11 %	42.75 %
Mean correlation (SNR and distance from Rx) (2 cases)	-0.83	-0.88

presented are considered, the results are more accurate for electron density maps based on the mobile GPS observables as opposed to electron density maps generated with the IRI2007 model. For case study 3 the results based on the IRI2007 model outperformed the results based on the mobile GPS observables. However, the good results obtained in terms of the various performance evaluation criteria with electron density maps based

on the mobile GPS observables in case studies 1 and 2, overshadows the results of case study 3 where the IRI2007-based electron density map produced better results. The results show that electron density maps generated from mobile GPS observables for HF path prediction are likely to be better than those generated from the IRI2007 model. This confirms the relative accuracy of the MIDAS inversion. However, the IRI model is not well-defined for the southern hemisphere due to a paucity of ionosonde data in this region. The mobile GPS receiver-based electron density maps, on the other hand, make use of indirect observations via GPS signals and the results should thus be better than those based on the IRI2007 model. In conclusion, the results confirm the viability of using electron density maps generated from mobile dual-frequency GPS receiver observables.

CHAPTER 5

CONCLUSION AND FUTURE WORK

CONCLUSION

In this dissertation the viability of using a mobile GPS receiver for ionospheric tomography was investigated. To verify the accuracy of the algorithm for tomographic inversion using mobile GPS observables, it was applied to a model ionosphere using simulated ray paths. The performance of various inversion parameters was investigated. Observations by a mobile GPS receiver were verified by ionosondes, static GPS receivers and HF propagation path prediction.

It was demonstrated both theoretically and practically that a mobile GPS receiver can be used successfully for ionospheric tomography. The experimental verification proved that a mobile GPS dual-frequency receiver can provide useful and fairly accurate electron density maps. If implemented correctly, the GPS receiver on the SA Agulhas research vessel together with the software developed for this dissertation will be the first of its kind that will be able to characterise the bottomside ionosphere over the Earth's oceans continuously. This provides a basis for future work on the use of mobile GPS receivers on vessels traversing the ocean for better characterisation of the ionosphere.

The primary objective of this research was to investigate the viability of using a mobile

GPS receiver for ionospheric tomography. The viability of this endeavour was confirmed by the results of the research. A secondary objective was to develop a system for processing observations from a mobile dual-frequency GPS receiver. The various electron density maps generated is evidence of the realisation of this objective.

In conclusion, the author demonstrated that the mobile dual-frequency GPS system under investigation can provide useful ionospheric electron density profiles by means of tomographic inversion, as demonstrated in Chapters 3 and 4.

FUTURE WORK

This study focussed on the viability of using a mobile GPS receiver for ionospheric tomography. The viability of using a mobile GPS receiver for ionospheric tomography was confirmed by the useful results presented in this dissertation. However, there are several aspects of ionospheric tomography that still need to be addressed before this method will equal the accuracy of current absolute measurement of instruments such as ionosondes. The following technical challenges, which were beyond the scope of this investigation, still have to be addressed.

- Current bias estimation methods are not reliable enough to obtain absolute electron density observations. The absolute electron density level plays an important role in applications such as HF propagation path prediction. It needs to be estimated accurately and independent of external data, since nearby absolute measurements are not always available for calibration.
- The inversion algorithm is very sensitive to the EOFs used in the MIDAS package and some research is needed to determine a method whereby the data is not dominated by the basis functions.
- Large-scale processing and storage of data from a network of mobile dual-frequency GPS receivers needs to be investigated to promote the viability of such a network.

Nevertheless, the research presented in this dissertation is a major step forward in the advancement of the characterisation of the ionosphere. The work presented here has the potential to develop into a global research project and will be of great value to space scientists and physicists and in engineering and military applications.

REFERENCES

[1] J. Goodman and J. Aarons, "Ionospheric effects on modern electronic systems," *Proceedings of the IEEE*, vol. 78, no. 3, pp. 512–528, Mar. 1990.

[2] N. Maslin, *HF Communications: a Systems Approach*. New York: Plenum Press, 1987.

[3] G. Xu, *GPS: Theory, Algorithms and Applications*, 2nd ed. Berlin: Springer, 2007.

[4] P. Cilliers, C. N. Mitchell, and B. D. Opperman, "Characterization of the ionosphere over the South Atlantic Ocean by means of ionospheric tomography using dual frequency GPS signals received on board a research ship," in *Proceedings of NATO Information Systems Technology (IST) Panel Specialists Meeting/Symposium on Characterising the Ionosphere*, University of Alaska, Fairbanks, Alaska, Jun. 2006, pp. 28:5–18.

[5] G. Hulot *et al.*, "Small-scale structure of the geodynamo inferred from Oersted and Magsat satellite data," *Nature*, vol. 416, pp. 620–623, 2002.

[6] B. Hofmann-Wellenhof *et al.*, *GPS Theory and Practice*, 5th ed. New York: Springer, 2001.

[7] C. Kee and B. Parkinson, "Wide Area Differential GPS (WADGPS): future navigation system," *IEEE Transactions on Aerospace and Electronic Systems*, vol. 32, no. 2, pp. 795–808, Apr. 1996.

[8] I. L. Harris *et al.*, "Ionospheric specification algorithms for precise GPS-based aircraft navigation," *Radio Science*, vol. 36, no. 2, pp. 287–298, Mar. 2001.

[9] K. Davies, *Ionospheric Radio*. London: Peter Peregrinus, 1990.

[10] C. N. Mitchell and P. S. J. Spencer, "A three-dimensional time-dependent algorithm for ionospheric imaging using GPS," *Annals of Geophysics*, vol. 46, no. 4, pp. 687–696, Aug. 2003.

[11] M. J. Angling *et al.*, "Development of an HF selection tool based on the electron density assimilative model near-real-time ionosphere," *Radio Science*, vol. 44, p. 11, Jul. 2009.

[12] J. M. Goodman, *HF Communications: Science and Technology.* New York: Van Nostrand Reinhold, 1992.

[13] E. D. Kaplan *et al.*, *Understanding GPS: Principles and Applications.* Boston: Artech House, 1996.

[14] R. W. Meggs, "Mapping of ionospheric total electron content using global navigation satellite systems," Ph.D. dissertation, University of Bath, Bath, UK, 2005.

[15] D. Coco *et al.*, "Variability of GPS satellite differential group delay biases," *IEEE Transactions on Aerospace and Electronic Systems*, vol. 27, no. 6, pp. 931–938, Nov. 1991.

[16] J. Austen, S. Franke, and C. Liu, "Ionospheric imaging using computerized tomography," *Radio Science*, vol. 23, no. 3, pp. 299–307, Jan. 1988.

[17] T. Raymund *et al.*, "Application of computerized tomography to the investigation of ionospheric structures," *Radio Science*, vol. 25, pp. 771–790, Sept. - Oct. 1990.

[18] K. Yeh and T. Raymund, "Limitations of ionospheric imaging by tomography," *Radio Science*, vol. 26, no. 6, pp. 1361–1380, 1991.

[19] E. J. Fremouw *et al.*, "Application of stochastic inverse theory to ionospheric tomography," *Radio Science*, vol. 27, no. 5, pp. 721–732, Sept. 1992.

[20] K. Rawer, "Synthesis of ionospheric electron density profiles with Epstein functions," *Advances in Space Research*, vol. 8, no. 4, pp. 191–199, 1988.

[21] D. Bilitza, "35 Years of International Reference Ionosphere - Karl Rawer's legacy," *Advances in Radio Science*, vol. 2, pp. 283–287, 2004.

[22] ——, "The International Reference Ionosphere Climatological Standard for the Ionosphere," in *Characterising the Ionosphere, Proceedings RTO-MP-IST-056*, no. 32, Neuilly-sur-Seine, France, 2006, pp. 1–12.

[23] C. Mitchell. Multi-Instrument Data Analysis System: example outputs of MIDAS. University of Bath. [Online]. Available: http://people.bath.ac.uk/eescnm/midas.htm

[24] R. M. Dear, "Wide area forecasting of total electron content over Europe," Ph.D. dissertation, University of Bath, Bath, UK, 2006.

[25] P. Prikryl *et al.*, "GPS TEC, scintillation and cycle slips observed at high latitudes during solar minimum," *Annales Geophysicae*, vol. 28, no. 6, pp. 1307–1316, 2010.

[26] B. Opperman, P. Cilliers, and S. Koch, *Ionospheric Measurement Campaign on board the SA Agulhas over transacts of the South Atlantic Ocean in support of HMO Antarctic SHARE Radar Experiment - User Manual*, Hermanus Magnetic Observatory and CDSM, Dec. 2007.

[27] Hermanus Magnetic Observatory. ISES Regional Warning Centre for Africa. [Online]. Available: http://spaceweather.hmo.ac.za/index.php?action=propagation&site=HER

[28] Mobat Communications, *HF Broadband Vertical Antenna FAA 5522 Specification Sheet*.

ADDENDUM A

LEGAL DOCUMENTATION

A.1 Permission to use figures and data

A.1.1 NASA - Fig. 2.2

Excerpt from NASA website regarding the use of media resources

---

Still Images, Audio Recordings, Video, and Related Computer Files

NASA still images; audio files; video; and computer files used in the rendition of 3-dimensional models, such as texture maps and polygon data in any format, generally are not copyrighted. You may use NASA imagery, video, audio, and data files used for the rendition of 3-dimensional models for educational or informational purposes, including photo collections, textbooks, public exhibits, computer graphical simulations and Internet Web pages. This general permission extends to personal Web pages.

This general permission does not extend to use of the NASA insignia logo (the blue "meatball" insignia), the retired NASA logotype (the red "worm" logo) and the NASA seal. These images may not be used by persons who are not NASA employees or on products (including Web pages) that are not NASA-sponsored.

NASA should be acknowledged as the source of the material except in cases of advertising. See NASA Advertising Guidelines.

A.1.2 Dr. Richard Dear - Fig. 2.2, 4.16

Excerpt from email correspondence

Dear Dr. Dear
I am a student currently enrolled at the University of Pretoria in South Africa for my Master's degree in electronic engineering. I am currently working on a project under the guidance of Dr. Pierre Cilliers from the Hermanus Magnetic Observatory. The project entails the use of MIDAS to perform GPS ionospheric tomography using data from a GPS receiver installed on a research vessel. In my dissertation, there is some of your figures from you thesis which I would like to use - specifically in the literature study. I would like to obtain your permission to use these figures, if possible. As soon as my dissertation is finalized, I will send the numbers of the specific figures I used to you.
I thank you in advance and I look forward to hearing from you.
Kind regards
SJ van der Merwe
University of Pretoria

==========

Yes that is fine, although note 1.1 is not mine.
May be able to dig out the jpeg versions if you want of figures, although the pdf looks good quality. Not 100% though, so worst case you can lift from the pdf.

What are you researching with MIDAS? Good to here that is still being used. Hope it is going well.

Best regards

Richard

A.1.3 RTO Paper - Fig. 2.3, 4.1

Excerpt from email correspondence

Good morning,

As the authors of papers presented at RTO Events continue to hold the copyright of their papers, you must ask permission from your study leader. If your study leader had co-authors on his/her paper you should - as a courtesy - also ask their permission.

...

==========

Alles in orde met my
Ben Opperman PhD
Space Physics Researcher
Hermanus Magnetic Observatory

==========

Ben & Cathryn
The e-mail below refers. I would like to grant permission for my student SJ van der Merwe to use material from our attached paper in his MEng dissertation and in a paper that may be based on his research.
Would you kindly add your permission if it is in order?
Regards

Pierre

Dr Pierre J Cilliers, PrEng
Research Physicist
Hermanus Magnetic Observatory (HMO)
P.O. Box 32, Hermanus, South Africa
www.hmo.ac.za

A.1.4 Dr. Bob Meggs - Fig. 2.5

Excerpt from email correspondence

Hello,

...

In principle, I am very happy to give permission for you to use figures from my PhD thesis. I would appreciate an acknowledgement in your dissertation, please. Note that some figures in my thesis are ones that I did not generate myself, so if you wish to use those you should seek permission from source. Generally, I have put an acknowledgement in the figure caption if this is the case, but if you are not sure please email me and I will be able to tell you. You are probably aware that Dr Cilliers has an electronic copy of my thesis.

...

==========

Dear Dr. Meggs
I am a student currently enrolled at the University of Pretoria in South Africa for my Master's degree in electronic engineering. I am currently working on a project under the guidance of Dr. Pierre Cilliers from the

Hermanus Magnetic Observatory. The project entails the use of MIDAS to perform GPS ionospheric tomography using data from a GPS receiver installed on a research vessel. In my dissertation, there is some of your figures from you thesis which I would like to use - specifically in the literature study. I would like to obtain your permission to use these figures, if possible. As soon as my dissertation is finalized, I will send the numbers of the specific figures I used to you.

I thank you in advance and I look forward to hearing from you.

Kind regards
SJ van der Merwe
University of Pretoria

A.1.5 Hermanus Magnetic Observatory - Fig. 2.11

Excerpt from email correspondence

SJ
You are welcome to use any Hermanus ionograms that you need for your thesis. All that we require is acknowledgement that the ionograms came from us.
If you use more than one then just a general acknowledgement such as
"All ionograms reproduced in this these were provided by the Hermanus Magnetic Observatory (HMO) and are used with their permission"
Or
If you use only one then in the figure caption you can just add "Ionogram provided by the Herm Ma Ob..
Hope this helps
Regards
Lee-Anne

--

A.1.6 NGI (Trignet) - Fig. 4.25

Excerpt from email correspondence

Hello Pierre

I am in San Francisco at AGU at present but have the opportunity to respond. My suggestion is that instead of a "References" citation, an acknowledgment to the data source could be made. This could be used for all data sources not created by the author. Not sure if this would be acceptable. Whichever route is selected please make sure that correct name for the office is used ie Chief Directorate: National Geospatial Information (NGI) (of the Department of Rural Development and Land Reform although the latter could be left off).

Regards

Richard

R T Wonnacott
Director : Survey Services
Chief Directorate : Surveys and Mapping
Private Bag X10
Mowbray
7705
SOUTH AFRICA

==========

Dear Richard
The e-mail below from my MSc student pertains. Is there a preferred way for citation of the use of data from Trignet in any publication?

Can you give him permission for the use of Trignet data in his dissertation?
Does he need to send you the details of the specific data he used, or could you provide him with a general statement of permission?

...

Regards
Pierre

Dr Pierre J Cilliers, PrEng
Research Physicist
Hermanus Magnetic Observatory (HMO)
P.O. Box 32, Hermanus, South Africa
www.hmo.ac.za

A.1.7 Lowell Digital Ionogram Data Base

Excerpt from the Lowell Digital Ionogram Data Base web site

The data acquired from the digisonde network for storage in the University of Massachusetts Lowell DIDBase may be used freely for educational and non-commercial academic research purposes by registered users only. Redistribution of the data is subject to the same conditions of use.

A.1.8 SA Agulhas operating Manual - Figs. 4.15 and 4.14

Excerpt from email correspondence

SJ
Hiermee verleen ek graag toestemming vir die gebruik van enige materiaal uit die GPS Manual waarvan ek 'n mede-outeur is.

Pierre

Dr Pierre J Cilliers, PrEng
Research Physicist
Hermanus Magnetic Observatory (HMO)
P.O. Box 32, Hermanus, South Africa
www.hmo.ac.za

==========

Middag dr.
Ek gebruik een of 2 foto's asook die sisteem vloeidiagram vanuit die GPS manual op die Agulhas. By wie moet ek toestemming kry vir die gebruik hiervoor?
Groete
SJ

A.1.9 NCDXF HF Beacon Project - Fig. 4.37

Excerpt from email correspondence

Dear SJ van der Merwe,

you have our permission to use the maps and any other content on the IBP web site that is of use to you.

We would appreciate receiving a copy of your thesis when you have it completed.

Regards,
Peter Jennings
IARU International Beacon Coordinator and IBP Webmaster

LIST OF TABLES

LIST OF FIGURES